Spring 5-11-2024

Deformation Mapping and Modeling of the Aleutian Volcanoes with InSAR and Numerical Models

Jiahui Wang
jiahuiwang@smu.edu

DEFORMATION MAPPING AND MODELING

OF THE ALEUTIAN VOLCANOES WITH INSAR AND NUMERICAL MODELS

Approved by:

_____

Prof. Zhong Lu
Professor of Geophysics

_____

Prof. Brian Stump
Professor of Geophysics

_____

Dr. Jinwoo Kim
Research Scientist of Geophysics

_____

Prof. Patricia Gregg
Associate Professor of Geology
(UIUC)

_____

Dr. Heresh Fattahi
Radar Engineer (JPL)

DEFORMATION MAPPING AND MODELING OF THE ALEUTIAN VOLCANOES WITH INSAR AND NUMERICAL MODELS

A Dissertation Presented to the Graduate Faculty of the

Dedman College

Southern Methodist University

in

Partial Fulfillment of the Requirements

for the degree of

Doctor of Philosophy

with a

Major in Geophysics

by

Jiahui Wang

B.S., Geophysics, University of Science and Technology of China

May 11, 2024

ACKNOWLEDGMENTS

This work could not have been accomplished without the wisdom of my wonderful advisor, Prof. Zhong Lu. I really appreciate his invaluable guidance, support, mentorship, and patience throughout my doctoral studies. His expertise and encouragement have been instrumental in shaping this dissertation. Thanks to Dr. Jinwoo Kim for his enormous help on SAR and InSAR processing and data preparation. I want to thank Prof. Patricia Gregg for the invaluable guidance on numerical modeling for volcanoes and constructive suggestions and discussions on the manuscripts. I am grateful to Prof. Brian Stump and Dr. Heresh Fattahi for the insightful discussions and unwavering support.

Thanks to all the faculty and staff at the department of Earth Science at SMU. Stephanie Schwob is always nice and helped a lot with the tedious paperwork. I benefited a lot from the valuable discussions with the SMU Radar Lab and UIUC Gregg Lab members. Thanks for all the help from my wonderful friends.

My heartfelt thanks go to my family and my girlfriend Yinglu Tang, for their love, encouragement, and support.

This study was funded by NASA Earth Surface & Interior Program (80NSSC19K0357), NASA NISAR Science Team (80NSSC19K1491; 80NSSC22K1888), and the Shuler-Foscue Endowment at the Southern Methodist University. ALOS-2 PALSAR-2 datasets are copyrighted and provided by Japan Aerospace Exploration Agency's via the 2nd and 3rd Research

Announcement on the Earth Observations (PI No. ER2A2N061; PI No. ER3A2N132). This work was supported through the “enabling cloud based InSAR science” ACCESS 2019 award. Part of this work was carried out at the Jet Propulsion Laboratory, California Institute of Technology, under a contract with NASA.

Wang, Jiahui B.S., Geophysics, University of Science and Technology of China

Deformation Mapping and Modeling
of the Aleutian Volcanoes with InSAR and Numerical Models

Advisor: Professor Zhong Lu

Doctor of Philosophy conferred May 11, 2024
Dissertation completed Apr 10, 2024

Surface deformation mapping is an essential component for comprehensive monitoring of volcanic activities, serving as a vital tool for discerning crucial insights into magma dynamics, storage, and migration for accurate hazard forecasting, assessment, and mitigation. However, monitoring of the volcanic deformation across the Aleutian volcanic arc is usually limited by the lack of terrestrial sensors deployed due to their remote locations and hostile environmental conditions, necessitating alternative methodologies for data acquisition and analysis.

My PhD study aims at precisely mapping the crustal deformation for the Aleutian volcanoes and tracking the evolution of the magmatic system with Interferometric Synthetic Aperture Radar (InSAR) and numerical deformation modeling. Advanced timeseries InSAR algorithms are applied to three cases: Okmok, Makushin, and western and central Aleutian. Deformation history since the 2008 eruption at Okmok mapped with PSInSAR unveils several successive inflation episodes with time-dependent rates. Finite Element Models (FEM) updated with Ensemble Kalman Filter (EnKF) find the timeseries deformation can be well explained by a spherical source with temporally steady location about 3.5 km beneath the central caldera, with cumulative volume change about 0.08 km^3 from 2008 to 2021.

Deformation mapped from SAR data collected across platforms have detected multiple inflation/deflation cycles characterized by temporally varying rates at Makushin volcano from 2004 to 2021. Inverse models of the crustal deformation suggest a Mogi source located to the northeast of the caldera at a depth ~6 km Beneath Sea Level (BSL). A shallow secondary deformation located to the southeast of the volcano, with rates about half that of the main deformation is also identified. A volatile intrusion/degassing dominated plumbing system is preferred by the inflation/deflation cycles with distinct magnitudes and lifetimes.

A new timeseries InSAR framework is developed based on the geocoded unwrapped interferograms produced from Jet Propulsion Laboratory (JPL) Advanced Rapid Imaging and Analysis (ARIA) system. Deformation histories for volcanoes in the western and central Aleutian are retrieved with this framework with Sentinel-1 imageries from 2015 to 2021. Various deformation patterns associated with different volcanic processes have been detected and used to track the evolution of volcanic systems. New deformation patterns are observed from Tanaga, Great Sitkin and Yunaska volcano. Overall higher magmatism, which may be attributed to spatial variation in tectonic environments, is identified in the central Aleutian.

To investigate the discrepancy between magmatic sources derived from geodetic deformation and the ones inferred from seismic tomography at Okmok, several numerical magma reservoir models are constructed and analyzed. The single reservoir model with magmatic chamber characterized by low P and S wave velocity (V_p and V_s, respectively) and moderate P to S wave velocity ratio (V_p/V_s) produce crustal deformation that fits the geodetic observations better than the distributed reservoir model with magma chambers represented by high V_p and V_p/V_s and low V_s, which likely reconcile the geodetic deformation and seismic tomography observations and

highlights the necessity of joint interpretation of geophysical observations over regions with complicated volcanic environments.

TABLE OF CONTENTS

LIST OF FIGURES

LIST OF TABLES

To my family

CHAPTER 1
INTRODUCTION

Crustal deformation is widely seen at active volcanic systems worldwide, usually found associated with a wide variety of volcanic activities, e.g., volume/pressure accumulation and extraction produced by the migration of magmas and hydrothermal fluids within the magma plumbing systems (Lu and Dzurisin, 2010; Wang et al., 2021), thermoelastic compaction of the lava flow and pyroclastic deposits emplaced during previous eruptions (Wang and Aoki, 2019; Chaussard, 2016), pressure loss due to degassing and crystallization from the plumbing systems and thermal contraction of the magma reservoirs (Shreve et al., 2019; Trasatti et al., 2019; Lu and Dzurisin).

Precise mapping of surface deformation provides critical constraints for the identification and modeling of the complex volcanic processes in the magmatic plumbing system. Essential source parameters, i.e., source location, shape, and pressure change within the magma reservoir can be determined from geophysical modeling for the surface displacements, providing valuable insights into the complex volcanic processes for volcano study, eruption forecasting and hazard mitigation (Dzurisin, 2006). For instance, surface deformation measured from tiltmeters detected the conduit opening and magma intrusion to shallow depth a few days before the large 1991 eruption at Mount Pinatubo, Philippines (Ewert et al., 1991); inverse models of crustal displacements derived from InSAR is used to determine the source parameters and mechanical

conditions for the onset of the 2018 eruption of Sierra Negra Volcano, Galápagos, Ecuador (Gregg et al., 2022).

The focus of this dissertation is to retrieve the deformation history of the Aleutian volcanoes and track the temporal evolution of their plumbing system with deformation modeling.

1.1 Background of the Aleutian Volcanoes

The Aleutian volcanic arc is produced by the subduction of the Pacific Plate beneath the North American Plate (Figure 1; Miller et al., 1998; Spence, 1977). Stretching more than 2000 km from east Russia to Alaska, the immense size of this convergent boundary created more than 40 historically active volcanoes characterized by diverse tectonic settings and volcanic environments and is one of the most volcanically and seismically active area in the world (Lu and Dzurisin, 2014).

Although most of Aleutian volcanoes are located in remote areas, the unanticipated eruptions and the associated hazardous ashes have enormous and immediate threat to aviation, marine transportation, and local communities. Due to the remote and isolated locations of these volcanoes, manually installing and continuously maintaining local seismic and infrasound sensors, geodetic networks, and web cameras is a challenging task for volcano researchers and monitoring authorities. Continuous Global Navigation Satellite Systems (GNSS; blue triangles in Figure 1), also referred to as Global Positioning System (GPS) are only installed at a small portion of the Aleutian volcanoes, e.g., Okmok, Makushin and Akutan. A few of the active volcanoes are monitored with other terrestrial sensors, e.g., Atka and Tanaga volcano are deployed with permanent seismometers (red triangles in Figure 1). A large number of the volcanoes with eruption records since 1700s are not monitored with any ground-based

instruments, e.g., Kasatochi and Bogoslof, where eruptions with Volcanic Eruption Index (VEI) exceeds 3 have been produced in 2008 and 2016, respectively.

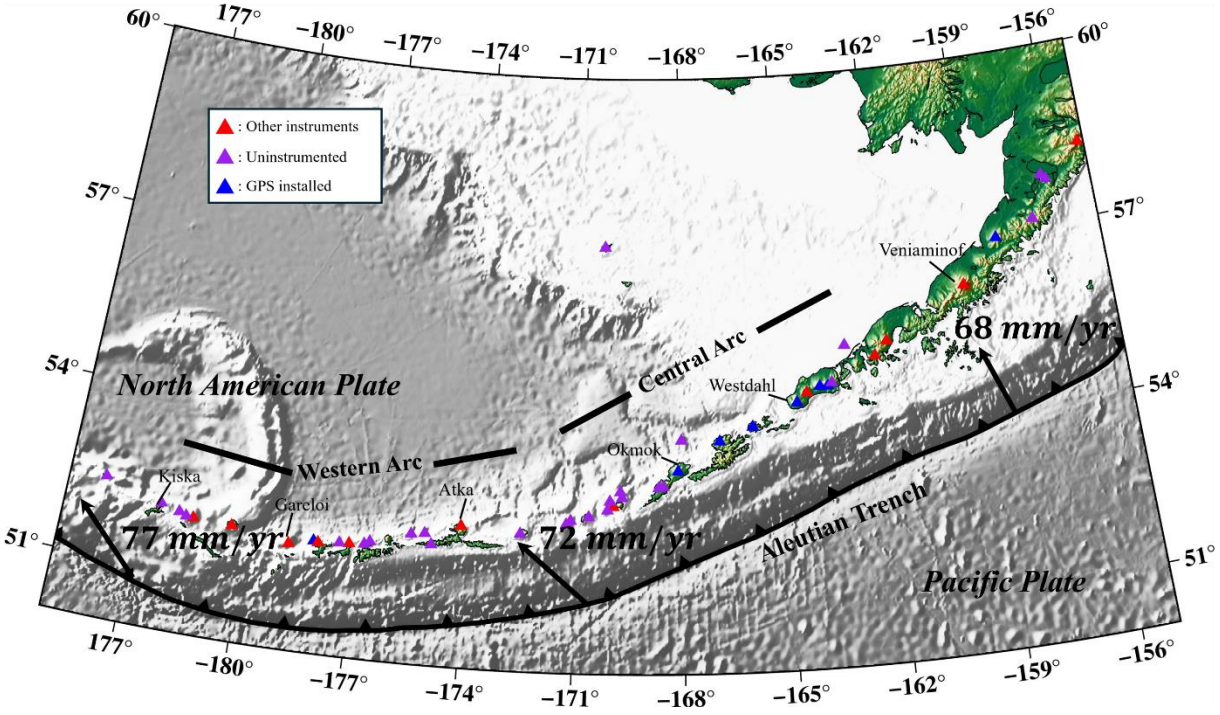

Figure 1.1 Map of part of the Aleutian volcanic arc. Historically active volcanoes are labeled with colored triangles. The Aleutian Trench is labeled as a solid black line with black triangles. The black arrows indicate the local slip velocity direction of the Pacific Plate relative to the North American Plate with the convergence rates labelled.

The very limited ground-based stations pose great challenges for real time monitoring, hazard predictions, and mitigations for the Aleutian volcanoes. Recent developments in remote sensing technologies have greatly increased the availability and volume of volcanic deformation data. These measurements from satellites provide comprehensive temporal and spatial coverage over remote and hazardous areas such as the Aleutian Island arc (Lu and Dzurisin, 2014; Dean

and Dehn, 2016). Of all these revolutionary techniques, Interferometric Synthetic Aperture Radar (InSAR) has been proven to be a very effective tool to accurately map the surface changes associated with volcanic activities in regions with good coherence and has been applied for deformation mapping at volcanoes worldwide (Lu and Dzurisin, 2014; Pritchard and Simons, 2004). In this dissertation, the deformation histories of the Aleutian volcanoes are mapped with several different InSAR algorithms.

1.2 InSAR Principal

Like the interferometry of optical lights, InSAR is the interferometry of the radar signals. The Synthetic Aperture Radar (SAR) records the amplitude and phase of the echoes from ground targets to the sensor, where the amplitude is determined mainly by the reflectivity of the ground surface and the phase is determined by the travel time from the target to sensor. InSAR measures surface changes by measuring the travel time difference of the radar signal between different passes:

$$\Delta R = -\frac{\lambda}{4\pi} \cdot (\phi_2 - \phi_1)$$

where ΔR is the line of sight (LOS) range change, λ is the wavelength of the radar signal, ϕ is the two-way travel time from the sensor to the ground targets.

Application of the conventional InSAR algorithms to the Aleutian volcanoes is very limited due to the coherence loss issue as a result of dense snow and ice coverage even during the summertime (Lu and Dzurisin, 2014). To solve this issue, taking advantage of the available multi-temporal SAR acquisition, timeseries InSAR processing, i.e., Small Baseline Subset (SBAS) and Persistent Scatterer (PS) InSAR algorithms, are used to extract targets that preserve better coherence during the observation period and reconstruct the deformation history.

SBAS algorithm utilize the interferometric pairs with small temporal and spatial baselines, which maintain higher coherence, to build an effective network of interferograms and inverse the deformation timeseries (Berardino et al., 2002). The general SBAS algorithm can be written as:

$$\boldsymbol{A}\phi = \delta\phi$$

Where $\boldsymbol{A}$ is an incidence-like matrix that dependent on the SBAS network, ϕ is the phase history and $\delta\phi$ is the unwrapped interferometric phase of the network. When all the acquisitions belong to a single subset, the phase history can be inverted with least-square methods. When two or more subsets are created, singular value decomposition (SVD) are usually used to solve the ϕ.

PS are defined as ground scatterers that are persistent over time. PSInSAR model the interferometric phase as:

$$\Delta\Phi = \Delta\Phi_{def} + \Delta\Phi_{atm} + \Delta\Phi_{orb} + \Delta\Phi_{topo} + \Delta\Phi_{noise}$$

where $\Delta\Phi_{\mathrm{def}}$, $\Delta\Phi_{atm}$, and $\Delta\Phi_{orb}$ are the spatially correlated phase difference due to deformation, atmospheric delay, and orbit error, respectively. $\Delta\Phi_{topo}$ and $\Delta\Phi_{noise}$ are the spatially uncorrelated phase term produced by DEM error and decorrelation noise. PS identification is done in three main steps: 1) the wrapped interferograms are filtered with combined low-pass and adaptive filters, with a weight initialized with the amplitude dispersion D_A for each PS candidate:

$$D_A = \frac{\sigma_A}{\bar{A}}$$

where σ_A is the standard deviation of the SAR amplitudes and $\bar{A}$ is the mean amplitudes. Afterwards, the spatially uncorrelated terms are separated by subtracting the filtered interferograms from the original interferograms. 2) The spatially uncorrelated terms are used to estimate the noise component for each PS candidate by extract the DEM error terms, which are

estimated by maximizing the temporal coherence γ

$$\gamma = \frac{\left|\sum_{i=1}^{n} e^{j\left(\phi_{SUC,i} - \phi'_{topo,i}\right)}\right|}{n}$$

where n is the total number of interferograms, $\phi_{SUC,i}$ is the spatially uncorrelated phase term of the i_{th} interferogram estimated from step 2, $\phi'_{topo,i}$ is the estimated topography error phase term for the i_{th} interferogram. An iteratively estimation of γ is conducted by updating the weight in step 1 with $(1 - P_{rand})^2$ for each PS candidates, where P_{rand} is the possibility of been normally distributed noise, calculated by comparison of the γ distribution of PS candidates and the simulated normally distributed noise. 3) cluster the calculated γ for each PS candidate based on the associated D_A, and compute the γ threshold by comparing the γ distribution of PS candidates with that of normally distributed noise for each D_A bin. Scatterers with γ higher than the calculated thresholds are identified as PS points. Phase unwrapping and corrections is applied to the PS points to retrieve the deformation time series after PS selection.

1.3 Deformation modeling

Both analytic and numerical models are used to infer the source parameters responsible for the derived surface deformation at the Aleutian volcanoes. Time-dependent source inversions are applied to the deformation timeseries with Ensemble Kalman Filter (EnKF). EnKF is a Monte Carlo implementation of the traditional Kalman Filter. The EnKF formulation is constructed by replacing the calculation of Jacobian of the transformation model from system parameters to observations with model ensembles. Combining model predictions from previous time step with observations, the evolutions of the system parameters are tracked using a Markov Chain of Monte Carlo method (Evensen, 2003):

$$\boldsymbol{A}^a = \boldsymbol{A} + \boldsymbol{P}_e\boldsymbol{H}^T(\boldsymbol{H}\boldsymbol{P}_e\boldsymbol{H}^T + \boldsymbol{R}_e)^{-1}(\boldsymbol{D} - \boldsymbol{H}\boldsymbol{A})$$

where $\boldsymbol{A}$ is the forecast ensemble matrix of the system parameter to be estimated and predicted observations, A^a is the updated $\boldsymbol{A}$. $\boldsymbol{P}_e$ is the covariance matrix of $\boldsymbol{A}$, $\boldsymbol{H}$ is the mapping matrix that linking the forecast ensemble $\boldsymbol{A}$ to the observations, $\boldsymbol{R}_e$ is the covariance matrix of the observations and $\boldsymbol{D}$ is the matrix of measurements. An iterative update strategy is applied to the individual time step to get a more accurate estimation of the source parameters as in Zhan and Gregg (2017).

For the transient deformation signals, e.g., earthquakes, Bayesian inversion algorithms are used to derive the deformation sources. The Bayesian inversion algorithms approach the optimal model parameters by maximizing the posterior probability distribution functions (PDF) :

$$p(\boldsymbol{d}|\boldsymbol{m}) = (2\pi)^{-N/2}|\boldsymbol{\Sigma_d}|^{-1/2} \times exp\left(-\frac{1}{2}(\boldsymbol{d}-\boldsymbol{Gm})^T\boldsymbol{\Sigma_d^{-1}}(\mathbf{d}-\boldsymbol{Gm})\right)$$

where $\boldsymbol{d}$ is the data vector, $\boldsymbol{m}$ is the model parameters (i.e., the location and the source strength), N is the number of data points, and $\boldsymbol{G}$ is the nonlinear model function that converts the model inputs to observations. $\boldsymbol{\Sigma_d}$ is the variance-covariance matrix of the data vector, and the variance-covariance matrix of the InSAR measurements is derived using the semivariogram (Bagnardi and Hooper, 2018).

1.4 Chapter summaries

In the second chapter, to investigate the discrepancy between the post-eruptive deformation derived from InSAR and GNSS (Qu et al., 2015) from 2008 to 2014, and update the deformation since 2015, I map the deformation history of the Okmok volcano from 2008 to 2021 with PSInSAR algorithm. The derived deformation time series from PSInSAR is consistent with the continuous GNSS records at all available sites and is then modeled with Finite Element Models (FEM) updated with EnKF to track the temporal evolution of the magma plumbing system at

Okmok volcano. Based on the temporal and spatial behavior of the source responsible for the surface deformation, the magma supply dynamics and eruption mechanisms are discussed. This work has been published in *Journal of Geophysical Research: Solid Earth* (https://doi.org/10.1029/2023GL106323).

Chapter 3 presents another work using PSInSAR, to derive the deformation history with multiple SAR datasets and track the evolution of the magmatic system at Makushin volcano from 2004 to 2021. The new deformation patterns that were not detected in previous surveys have been identified and discussed. The mechanisms of the successive inflation/deflation at time-dependent rates are also discussed. Large scale surface erosion along the valleys is detected in the L-band ALOS2 interferograms. This work has been published in *Journal of Volcanology and Geothermal Research* (https://doi.org/10.1016/j.jvolgeores.2023.107991).

In Chapter 4, I build a new timeseries InSAR processing framework for large-scale deformation mapping over the tectonically active region based on the Geocoded Unwrapped (GUNW) products provided by JPL's ARIA processing system and produced the deformation history of the historically active volcanoes in the western and central Aleutian. The derived deformation time series are modeled to track the temporal evolution of the sources at several volcanoes. The newly discovered deformation patterns at several volcanoes and the temporal/spatial distributions of the along-arc volcanism are discussed. This work has been published in *Geophysical Research Letters* (https://doi.org/10.1029/2023GL106323).

In Chapter 5, To interpret the discrepancy between multi-disciplinary observations, e.g., deformation derived from geodetic measurements and seismic wave velocity produced from seismic tomography, I build multi-physical models incorporating the coupled thermal and mechanical processes to model the complicated magmatic plumbing system for Okmok

volcanoes. A series of sensitivity tests have been conducted to determine the effects of multiple factors that may disturb the predicted surface deformation. Several reservoir models are built based on the tomography and are tested with surface deformation. Principles for reconciling the geodetic deformation and seismic tomography for volcanic system modeling is discussed.

1.5 Reference

Bagnardi, M. and A. Hooper (2018), Inversion of surface deformation data for rapid estimates of source parameters and uncertainties: A Bayesian approach, Geochem. Geophys. Geosyst., 19(7), 2194-2211.

Berardino, P., G. Fornaro, R. Lanari, and E. Sansosti (2002), A new algorithm for surface deformation monitoring based on small baseline differential SAR interferograms, IEEE Trans. Geosci. Remote Sens., 40(11), 2375-2383.

Chaussard, E. (2016a), Subsidence in the Parícutin lava field: Causes and implications for interpretation of deformation fields at volcanoes, J. Volcanol. Geotherm. Res., 320, 1-11.

Chaussard, E. (2016b), Subsidence in the Parícutin lava field: Causes and implications for interpretation of deformation fields at volcanoes, J. Volcanol. Geotherm. Res., 320, 1-11.

Dzurisin, D. (2006), Volcano Deformation: New Geodetic Monitoring Techniques, Springer Science & Business Media.

Ewert, J. W., A. B. Lockhart, S. Marcial, and G. Ambubuyog (1996), Ground deformation prior to the 1991 eruptions of Mount Pinatubo, Fire and Mud; Eruptions and Lahars of Mount Pinatubo, Philippines.Philippine Institute of Volcanology and Seismology, 329-338.

Lu, Z., D. Dzurisin, J. Biggs, C. Wicks Jr, and S. McNutt (2010), Ground surface deformation patterns, magma supply, and magma storage at Okmok volcano, Alaska, from InSAR analysis: 1. Intereruption deformation, 1997–2008, Journal of Geophysical Research: Solid Earth, 115(B5).

Gregg, P. M., Y. Zhan, F. Amelung, D. Geist, P. Mothes, S. Koric, and Z. Yunjun (2022), Forecasting mechanical failure and the 26 June 2018 eruption of Sierra Negra volcano, Galápagos, Ecuador, Science advances, 8(22), eabm4261.s

Miller, T. P., R. G. McGimsey, D. H. Richter, J. R. Riehle, C. J. Nye, M. E. Yount, and J. A. Dumoulin (1998), Catalog of the Historically Active Volcanoes of Alaska, United States Department of the Interior, United States Geological Survey.

Pritchard, M. E. and M. Simons (2004), An InSAR‐based survey of volcanic deformation in the central Andes, Geochem. Geophys. Geosyst., 5(2).

Shreve, T., R. Grandin, M. Boichu, E. Garaebiti, Y. Moussallam, V. Ballu, F. Delgado, F. Leclerc, M. Vallée, and N. Henriot (2019), From prodigious volcanic degassing to caldera subsidence and quiescence at Ambrym (Vanuatu): the influence of regional tectonics, Scientific Reports, 9(1), 18868.

Spence, W. (1977), The Aleutian arc: Tectonic blocks, episodic subduction, strain diffusion, and magma generation, Journal of Geophysical Research, 82(2), 213-230.

Trasatti, E., V. Acocella, M. A. Di Vito, C. Del Gaudio, G. Weber, I. Aquino, S. Caliro, G. Chiodini, S. de Vita, and C. Ricco (2019), Magma degassing as a source of long‐term seismicity at volcanoes: the Ischia Island (Italy) case, Geophys. Res. Lett., 46(24), 14421-14429.

Wang, J., Z. Lu, and P. M. Gregg (2021), Inflation of Okmok volcano during 2008–2020 from PS analyses and source inversion with finite element models, Journal of Geophysical Research: Solid Earth, 126(10), e2021JB022420.

Wang, X. and Y. Aoki (2019), Posteruptive thermoelastic deflation of intruded magma in Usu volcano, Japan, 1992–2017, Journal of Geophysical Research: Solid Earth, 124(1), 335-357.

Zhan, Y. and P. M. Gregg (2017), Data assimilation strategies for volcano geodesy, J. Volcanol. Geotherm. Res., 344, 13-25, doi: 10.1016/j.jvolgeores.2017.02.015.

CHAPTER 2
INFLATION OF OKMOK VOLCANO DURING 2008–2020 FROM PS ANALYSES AND SOURCE INVERSION WITH FINITE ELEMENT MODELS

2.1 Abstract

Okmok volcano, located on northeastern Umnak Island along the eastern end of the Aleutian Island arc, is one of the most active volcanoes in Alaska, producing multiple eruptions in the past century. The most recent eruption, which occurred during July–August of 2008, was the most explosive since the early nineteenth century. In the years following the 2008 eruption, Global Navigation Satellite System (GNSS) and Interferometric Synthetic Aperture Radar (InSAR) observations indicate that Okmok has inflated at a variable rate of 40–195 mm/yr. In this study, we investigate the post-eruptive deformation of Okmok (2008–2020) using InSAR and GNSS. L-band ALOS-2, C-band Sentinel-1/Envisat and X-band TerraSAR-X data are analyzed with Persistent Scatterer (PS) InSAR method. The deformation time series calculated from InSAR and GNSS are assimilated into finite element models using the Ensemble Kalman Filter to track the evolution of the magma system through time. The results indicate that the InSAR derived deformation history can be well explained by a spatially stable magmatic source located in the central caldera, at about 3 km beneath the sea level, which is also believed to be the same source that produced the 1997 and 2008 eruptions. Magma accumulation in the reservoir is about 0.08 km3 from 2008 to 2020, which is about 160% and about 60% of the total reservoir volume changes during the 1997 and the 2008 eruptions, respectively.

2.2 Introduction

Okmok, located in the northeast of the Umnak Island, Alaska, is one of the most activate volcanoes in the Aleutian Island Arc. Two major catastrophic pyroclastic eruptions with max Volcanic Explosivity Index (VEI) exceeded 4, i.e., Okmok Caldera Forming Eruption (CFE) I and Okmok CFE II dated about 12000 years and 2050 ^{14}C years ago, respectively, shaped the major topographic morphology of Okmok (Larsen et al., 2007; Byers, 1959). In addition to the current caldera rim, evidence from six arctic ice cores shows the Okmok CFE II may also be responsible for one of the coldest decades of recent millennia in the Northern Hemisphere (McConnell et al., 2020). Since 1900, multiple effusive eruptions have been documented at Okmok producing a new prominent cone, Cone A. From 1943 to 1997, all Okmok's eruptions originated from Cone A (Figure 2.1; Lu and Dzurisin, 2014). The most recent eruption in 2008, spanned from July 12 to mid-August, was the most explosive eruption since at least the late nineteenth century, and produced a minimum of 0.17 km^3 of dense rock-equivalent ejecta (Larsen et al., 2015). As opposed to previous eruptions, the 2008 eruption emanated from the northwest flank of an existing cinder cone (Cone D), about 5 km northeast of Cone A. Due to the strong magma interaction with ground and surface water, the 2008 eruption was highly phreatomagmatic (Larsen et al., 2013; 2015). The ejected ash and tephra deposit during the 2008 eruption covered the entire caldera and part of the northeast flank of the caldera and formed a new tuff cone near Cone D (named "Ahmanilix"; Larsen et al., 2015).

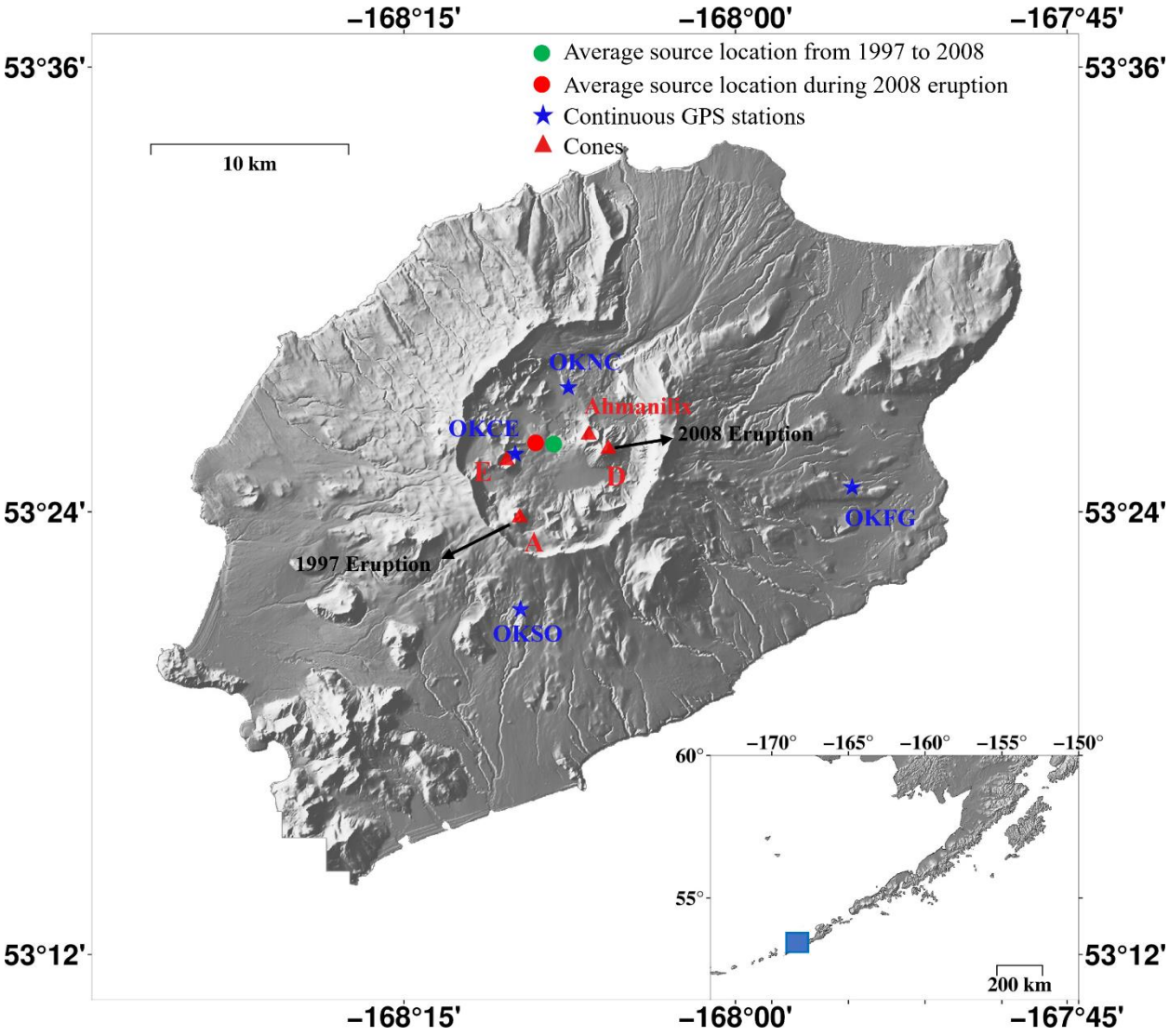

Figure 2.1 Location and topography of Okmok volcano. GNSS stations are labeled as blue stars. Red triangles represent the cones. Red circle represents the average location of the source producing the co-eruptive deflation during the 2008 eruption. Green circle indicates the average location of the source responsible for the inflations from 1997 to 2008.

Due to the remote location and small population of Umnak Island, most of Okmok's historical eruptions are poorly documented. Thanks to the advance in spaceborne geodetic techniques, the 1997 and 2008 eruptions were well observed and documented. The magma

source and eruption mechanisms have been previously studied using ground deformation measurements from InSAR and GNSS data. Before the 1997 eruption, inflation with a decreasing rate was observed from 1992 to 1995 and stalled sometime during 1995–1996, during which stage slight local subsidence occurred instead (Lu et al., 2000; Mann et al., 2002). The pre-eruption inflation was interpreted as the result of accumulation of magma, the local deflation may have been related to withdrawal or movement of the magma or hydrothermal depressurization (Mann et al., 2002). Since the first post-eruption observation in 1997, persistent inflation at a varying rate was confirmed by both InSAR and GNSS. Episodic pulses of more rapid inflation signals were observed during 1997–1998 and 2001–2003. The deformation rate decreased, and the caldera subsided 3–5 cm during 2004–2005, and then elevated a similar amount during 2005–2006. Preceding the 2008 eruption, uplift of ~150 mm/yr was recorded during 2007–2008 (Fournier et al., 2009; Lu et al., 2010). Based on the deformation signal from 1992 to 2008 derived from multiple InSAR datasets, Lu et al. (2005, 2010) inferred a tension sphere (Mogi) source embedded ~3 km below sea level (BSL). Fournier et al. (2009) derived a stable Mogi source at ~2.5 km BSL with both campaign and continuous GNSS data spanning from 2000 to 2007. Biggs et al. (2010) found a Mogi source at a depth of ~3.4 km using a combined data set consisted of GNSS data spanning from 2000 to 2007 and InSAR data from 1992 to 2007. Lu et al. (2010) found a Mogi source with a depth evolving from ~2 km BSL in the beginning of the eruption to ~3 km BSL post-eruptive period using co-eruptive deformation derived from InSAR data. Freymueller and Kaufman (2010) interpreted the magma source as a Mogi sphere lying ~1.9 km BSL and captured the reinflation almost three weeks right after the vigorous ash emissions.

Subsequent to the 2008 eruption, Qu et al. (2015) analyzed post-eruptive InSAR data from four satellite tracks and found a time varying inflating rate of 48–130 mm / yr from 2008 to 2014 and found the best fit source accounting for this uplift signal is a Mogi source ~3.9 km BSL. However, using the same results, Xue et al. (2020) found a best fit model consisting of a Mogi source at ~3.2 km lying beneath a shallow sill at about 0.9 km, they then updated the magma accumulation status of Okmok using campaign and continuous GNSS data with the source derived using the InSAR results from Qu et al. (2015). In this study, we focus on the post-eruptive deformation from 2008 right after the eruption to 2020.

In this study, we use PSInSAR techniques to produce deformation time series for Okmok volcano, using data from 4 different sensors and six independent imaging geometries to track the evolution of the Okmok magma system since its 2008 eruption. The deformation time series captures the temporal evolution of the surface deformation at Okmok volcano. The Ensemble Kalman Filter (EnKF) is used to track the source parameters over time as the system evolves. EnKF is a time-dependent inversion filter based upon the traditional Kalman Filter (KF). The KF is a data assimilation algorithm that evaluates a linearly evolving system problem. It uses a series of measurements observed over time containing statistical noise and other inaccuracies to produce estimates of unknown model parameters (Kalman, 1960). The EnKF uses an ensemble of forward models to link system parameters to observations. The ensemble approach enables EnKF to overcome the limitations of the traditional KF and Extended Kalman Filter (EKF), such as high computation load and poor performance when dealing with highly nonlinear systems (Evensen, 2003, 2009). Here we adopt the framework developed by Gregg and Pettijohn (2016) and Zhan and Gregg (2017) to assimilate the deformation time series computed from InSAR into

linear elastic finite element models (FEM) of the magma source to investigate the evolving state of the Okmok magma system.

2.3 Methods and Datasets

2.3.1 Time-Series InSAR Algorithms

Conventional InSAR deals with only a few interferometric pairs. In this scenario, the measurement accuracy can be significantly compromised by artifacts and noise such as Atmospheric Phase Screen (APS) due to the atmospheric phase delay, orbital error introduced by inaccurate satellite orbit determination, unwrapping errors due to large phase jump or decorrelation, topography error due to inaccurate DEM, and geometric errors associated with the change in look angle between the sensor and the ground targets (Hooper et al., 2007). The PSInSAR technique provides a way of approaching such problems. PSInSAR algorithms aim at extracting scattering mechanisms from ground targets that persist over the observation period to maintain good interferometric coherence. Since the emergence of PS concepts in the last two decades, there are two main approaches for PSInSAR implementation. One approach uses the amplitude dispersion as a proxy for the stability of the scattering mechanism; points with small amplitude dispersions are selected and used for subsequent PSInSAR processing (Ferretti et al., 2001). The other one assumes the noises are spatially uncorrelated and identifies PS by noise level thresholding (Hooper, 2008; Hooper et al., 2004). In this research, we use the later one, which is also referred to as the Stanford Method for Persistent Scatterers (StaMPS). The standard procedure of PS incorporating SBAS, hereafter called PSSBAS, is used to process the SLC image stack. For detailed description of the algorithm, readers should refer to Chapter 1 and Hooper (2008) and Hooper et al. (2007).

2.3.2 SAR Datasets and Processing

SAR datasets used in this study begin in September 2008, one month after the last ash emissions recorded on August 20, 2008. The C-band Envisat P222 track spans from 2008 to 2010 with 7 scenes in total. The TerraSAR-X P116 track spans from 2011 to 2014 with 8 scenes in total. The temporal gap is about 11 months between the Envisat and TerraSAR-X and about 9 months between the Sentinenl-1 and TerraSAR-X. The C-band Sentinel-1 P95 track spans from 2015 to 2020 with 44 scenes, and P168 track from 2016 to 2020 with 40 scenes. The L-band ALOS-2 P92 track spans from 2015 to 2019 with 8 scenes, and P93 track from 2015 to 2019 with 9 scenes. All the SAR images are acquired in summer from June to October. Winter scenes are discarded due to the decorrelation effects introduced by the thick snow and ice coverage. To remove the topographic contribution from the interferometric phase, we use the high-resolution ArcticDEM generated with optical stereo imagery (Porter et al., 2018). Precise DORIS orbits are used for the Envisat data for baseline calculation. Interferometric pairs with relatively small perpendicular baseline and temporal separation are selected to reduce the spatial and temporal decorrelation. Additionally, to reduce the influence of APS to the 3D phase unwrapping, a minimum temporal separation of 60 days is used when smoothing the phase spatial gradient in time for computation of the cost function for the network-flow phase unwrapping. The perpendicular baselines threshold given to each track is a compromise between a relatively denser network for retrieving single referenced deformation history and relatively smaller perpendicular baseline to maintain interferometric coherence. The reference region for phase unwrapping is selected in either the southeast area near the GNSS station OKFG, or the northeast of the island if OKFG is not covered in the SAR images. The volcanic deformation over these regions is negligible.

The SBAS networks constructed are shown provided in Figure 2.2. The derived deformation time series are then validated with the GNSS data provided by the Nevada Geodetic Laboratory (Blewitt et al., 2018) from 3 sites: OKCE, OKNC, and OKSO (Figure 2.1). The temporal coverage of GNSS data is shown as in Figure 2.2g.

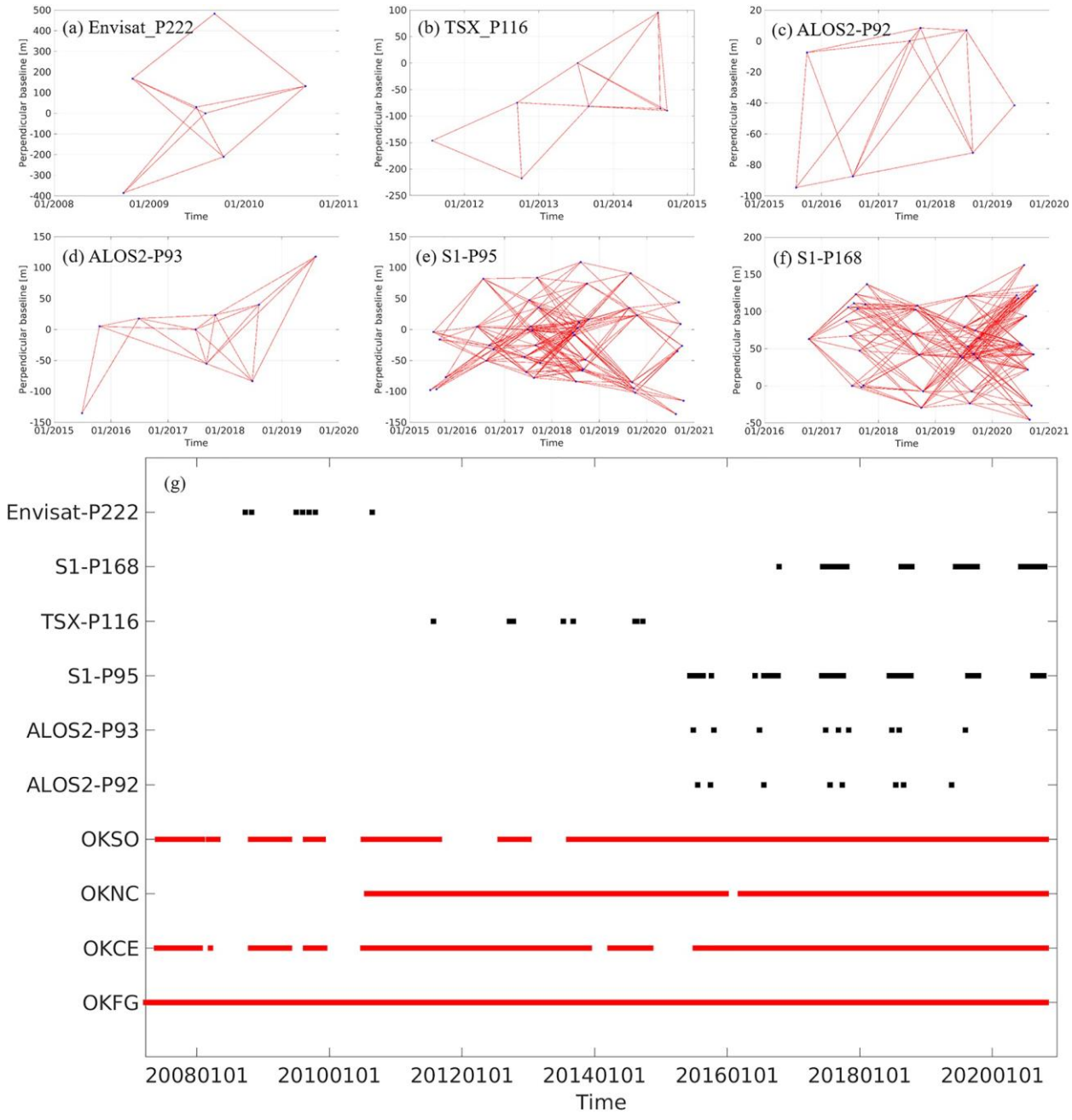

Figure 2.2. Temporal-spatial baseline distribution of the SBAS network for the six InSAR datasets and temporal coverage of GNSS data used: Interferograms with perpendicular baseline less than (a) 400 m for C-band Envisat P222 track; (b) 200 m for X-band TerraSAR-X P116 track; (c) 100 m for L-band ALOS-2 P92 track; (d) 200 m for L-band ALOS-2 P93 track; (e) 150 m for C-band Sentinel-1 P95 track; (f) 100 m for Sentinel-1 P168 track. (g) Temporal coverage of SAR and Continuous GNSS data used in this study.

2.3.3 Time-Dependent Source Inversion

The deformation time series calculated with PSInSAR are then used for the inversion of the Okmok magma source with an ensemble of FEMs updated by the EnKF. We use a three-dimensional, linear elastic FEM to model stress and strain with COMSOL Multiphysics 5.5®. The source is modeled as an incompressible pressure sphere with a radius of R and an overpressure ΔP, embedded at a depth of Z below the surface. The host rocks are modeled as a block of homogeneous linear elastic materials with a dimension of $60\ km \times 60\ km \times 20\ km$, a Young's modulus of $7.5 \times 10^{10}\ Pa$ and a Possion's ratio of 0.25. Initial isostatic stress is applied in response to the constant gravity ($g = 9.8\ m^2/s$).

$$\sigma_1 = \sigma_2 = \sigma_3 = \rho g z$$

Where $\boldsymbol{\sigma_i}$ are the initial principle stress, $\rho = 2700\ kg/m^3$ is the density of the crust, $\boldsymbol{z}$ is the depth. The side and bottom boundaries are characterized by roller condition and the upper surface is free to deform. We use a mesh-controlled domain with finer mesh grids near the magma reservoir location for higher accuracy.

For the EnKF setup, an iterative parameter updating strategy is employed as described in Zhan and Gregg (2017). 100 ensembles are used and a maximum of 10 iteration steps to balance between parameter precision and computational costs. Previous studies suggest better inversion results could be achieved when displacements from both InSAR and GNSS measurements are jointly assimilated into the sequential source inversion (Zhan and Gregg, 2017; Albright et al., 2019). However, for our case, the three GNSS records do not provide enough constraints to the source parameters, i.e., three-dimensional location, magma reservoir radius and overpressure inside the magma chamber. Assimilation of GNSS data leads to divergence instead of providing important time evolution updates during the temporal gap of InSAR data collections. Moreover,

since the InSAR data from different tracks take different references, and only the TerraSAR-X are acquired from a descending orbit, it is not feasible to assimilate InSAR observations from different tracks. In such a scenario, we conduct the time dependent source inversion independently for each InSAR tracks and then link them with the GNSS data to provide the full-time range of the magma system evolution of Okmok after the 2008 eruption. The GNSS data were downsampled to 30-day average bins. The source locations for the GNSS inversion are fixed based on our InSAR results. Only the source strength, i.e., radius of the pressure sphere and over pressure inside the chamber are variables that updated at each EnKF updating step. The cumulative post-eruptive volume changes at each InSAR reference date are also estimated from the GNSS records. The cumulative volume changes associated with the InSAR observations are then derived by adding the incremental volume change from each track to the cumulative volume change at the reference date. To reduce the influence of APS and other noise on the source modeling, we only use InSAR results inside the caldera, which we will discuss in detail later.

2.4 Deformation history and source evolution

2.4.1 Deformation history since 2008

The deformation history since the 2008 eruption is generated with the PSInSAR algorithms, with Spatially Correlated Look Angle (SCLA) error corrected using a least squares sense. APS correction in StaMPS is accomplished by a high-pass filter in time and low-pass filter in space (Hooper et al., 2004). For this application, SCLA correction alone is enough for accurate deformation mapping inside the caldera (Figure 2.4). Results with APS correction tend to bias deformation signals both inside and outside the caldera compared to the records of GNSS, which we use as ground truth to validate the InSAR measurements. One possible reason may be that the inflation rates are time varying, the low-pass filter during APS correction tends to flatten the

higher frequency signals and introduce bias. Therefore, APS corrections are not applied in the InSAR results. After the SCLA correction, the cumulative deformations are derived from the SBAS network using a least squares approach. The deformation mapped from different datasets are shown as in Figure 2.3. The corresponding cumulative deformation derived from each SAR data set is shown in Table 1. The inflation is persistent throughout the whole observation period from 2008 to 2020 for all the six InSAR tracks. The region of the most deforming area is located near the center of the caldera, with little variation during the entire time span.

Scene ID	Envisat P222	TerraSAR-X 116	ALOS-2 P92	ALOS-2 P93	Sentinel-1 P95	Sentinel-1 P168
Start time	20080924	20110727	20150722	20150629	20150609	20161012
End time	20100825	20140924	20190522	20190805	20201010	20201015
Cumulative deformation (mm)	300	180	280	310	350	320

Table 2.1. Cumulative deformation for each InSAR dataset. Dates are in the format of YYYYMMDD.

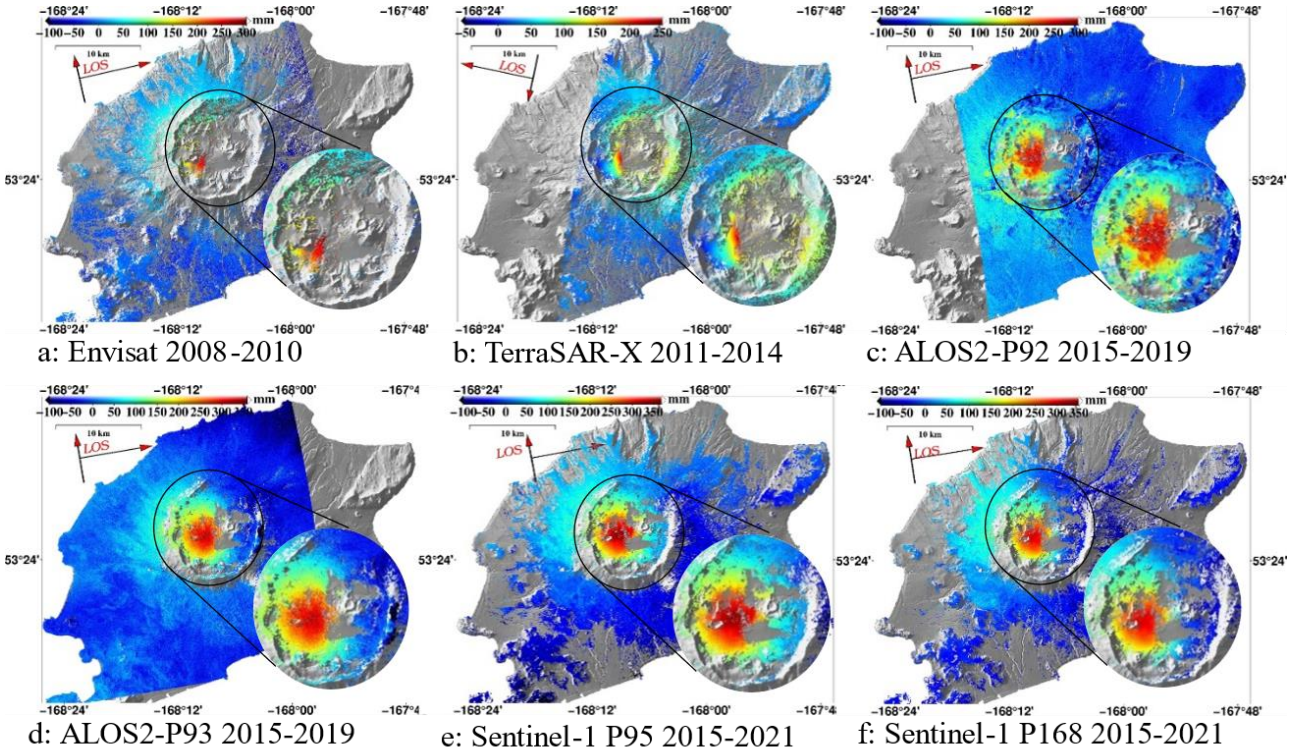

Figure 2.3. Cumulative deformation maps from different InSAR tracks. The signal in red corresponds to uplift. (a) Envisat P222 track, (b) TerraSAR-X P116 track, (c) ALOS-2 P92 track, (d) ALOS-2 P93 track, (e) Sentinel-1 P95, and (f) Sentinel-1P168. All the deformation measurements are in the Line-Of-Sight (LOS) directions. Deformations inside the caldera are enlarged in the inset to improve visibility.

The cumulative deformation maps are then compared with the GNSS records for validation of measurement accuracy at three GNSS stations, that is, OKCE, OKNC, and OKSO (Figure 2.4). The GNSS measurements are corrected for non-volcanic deformation, mainly tectonic signals due to the interaction between the Pacific plate and the North American plate, by subtracting the measurements from a GNSS station far away from the deforming center at a distance of about 15 km, that is, OKFG (Figure 2.1). The three-dimensional GNSS measurements are then projected to the LOS direction of the corresponding SAR imaging

geometry. PS within 100 m of the GNSS sites are selected and their averages are computed for the comparison. The promising agreement between the InSAR derived deformation time series and the GNSS solution suggests our InSAR measurements are reliable, with most of the standard deviations of the difference between the InSAR results and GNSS records less than 1cm.

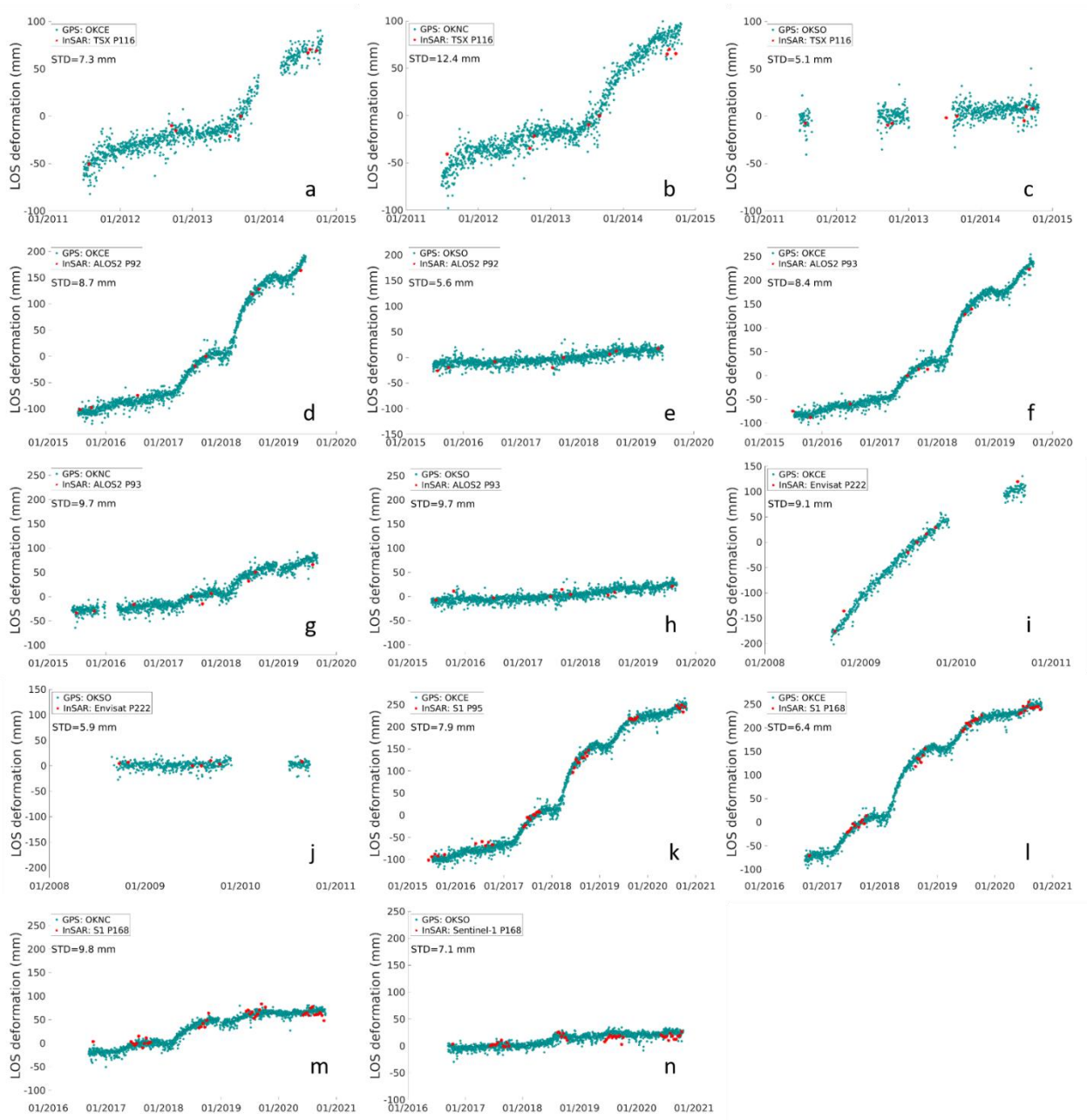

Figure 2.4. Comparison of deformation time series from InSAR with the GNSS observations in the LOS direction: (a) (b) (c): deformation from TerraSAR-X P116 track and GNSS at station OKCE, OKNC and OKSO, respectively; (d) (e): deformation from ALOS-2 P92 and GNSS site OKCE and OKSO, respectively; (f) (g) (h): deformation from ALOS-2 P93 and GNSS site OKCE, OKNC and OKSO, respectively; (i) (j): deformation from Envisat P222 and GNSS site OKCE and OKSO, respectively; (k): deformation from Sentinel-1 P95 and GNSS site OKCE; (l) (m) (n): deformation from Sentinel-1 P168 and GNSS site OKCE, OKNC and OKSO, respectively. All the GNSS observations are referenced to OKFG and are shifted to the same reference data of the InSAR observations, respectively. The InSAR measurements agree well with the GNSS records with most of the standard deviation of their difference less than 1 *cm*.

2.4.2 Evolution of the magma system

We use a single incompressible pressure sphere to capture the temporal evolution of the deformation obtained above. The InSAR results are resampled to $50m \times 50m$ grids to reduce noise and data volume for the EnKF processing. The measurement uncertainty of InSAR is determined as the standard deviation of the phase of PS fallen into the same grid, plus the uncertainties introduced by APS, which is computed using semi-variograms over areas where volcanic deformation is negligible (Murray et al., 2019). One great advantage of EnKF is not only the evolution of parameters that are tracked with the time-dependent filter, the uncertainty of the system parameters can also be estimated to the first order for each assimilation (Evensen, 2009). In our case, the uncertainty is high for the first a few steps and then the estimation converges rapidly over time. Due to the nature of non-uniqueness in the inversion, we use a single volume change, which combines both the source radius and the overpressure of the magma chamber, to represent the source strength.

Our results show a stationary source embedded ~3.5 km beneath the mean elevation of the caldera floor, which is equivalent to a source about 3 km BSL (Figure 2.5), can account for most of the observed InSAR signals and agree well with previous studies of the pre-2008 eruption magma system (Albright et al., 2019; Biggs et al., 2010; Fournier et al., 2009; Lu et al., 2005, 2010). The easting and northing of the source position are relatively unstable during 2008–2014 compared to those in the period from 2015 to 2020, which was also identified in Qu et al. (2015). As previous studies have confirmed that the position of the shallow magma source is stable without significant temporal variations, we believe that this fluctuation during 2008–2014 is a result of sparse spatial coverage of InSAR data inside the caldera, which adversely impacts the performance of EnKF leading to the need for a model spin-up period (Zhan & Gregg, 2017).

Sparse PS density inside the caldera is caused primarily by the decorrelation associated with mobile tephra deposited during the 2008 eruption. Since after the 2008 eruption, magma storage in the source has been increasing at a time-varying rate with a maximum rate of about $0.006\ km^3/yr$ during 2017–2018 and a minimum rate of about $0.003\ km^3/yr$ during 2015–2016 and 2019 to 2020. The fluctuating magma accumulation rate is similar to that during the previous inter-eruption cycle during 1997 and 2008 (Lu & Dzurisin, 2014; Lu et al., 2010).

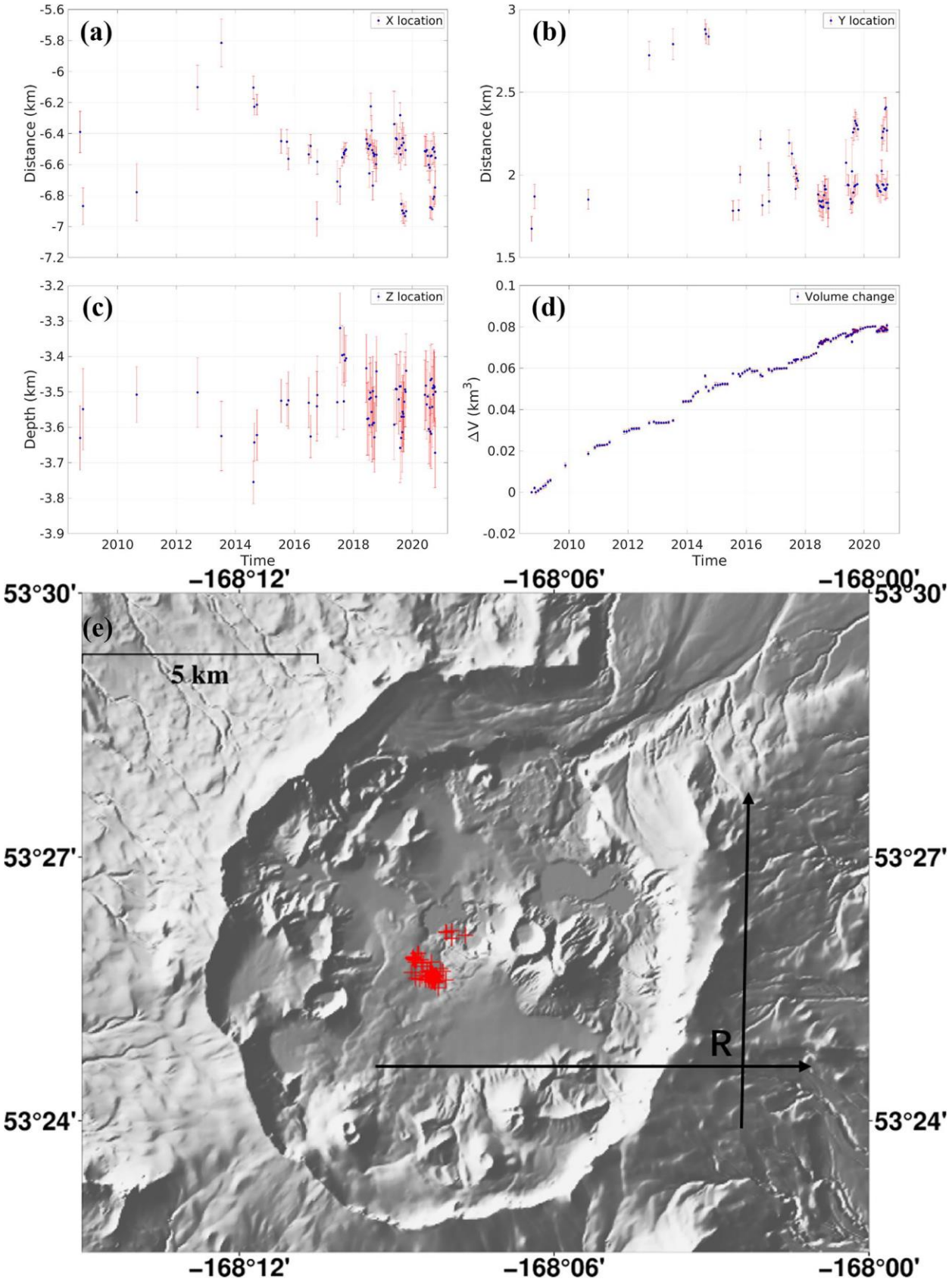
(a)
X location
Distance (km)
(b)
Y location
Distance (km)
(c)
Z location
Depth (km)
Time
(d)
Volume change
ΔV (km3)
Time
(e)
5 km
R
−168°12'
−168°06'
−168°00'
53°30'
53°27'
53°24'

Figure 2.5. Time dependent source models from 2008 to 2020 based on the InSAR data with error bars showing 1σ uncertainties. (a) Temporal evolution of easting coordinate of the magmatic deformation source with respect to an arbitrary reference R (figure 2.5e) and its uncertainty. (b) Northing coordinate of the best-fit source as a function of time and its uncertainty. (c) Best-fit depth of the deformation source and its uncertainty as a function of time. (d) Evolution of source strength (cumulative volume change) and its uncertainty with time. (e) Lateral spreading of the inverted source position, where R is the reference point for the easting and northing coordinates.

2.5 Discussion

2.5.1 InSAR processing error analysis

In this study, we use only the InSAR observations inside the caldera for the source inversion despite the fact that significant volcanic deformation can be easily identified at a distance of several kilometers away from the inflation center. This data selection strategy, which produced a rather persistent and precise estimation of the magma system (Figure 2.5a, 2.5b, 2.5c, 2.5e), is an optimization for the derived time-series InSAR results. The methodology we use for the multi-interferogram algorithm, PS-SBAS, is a three-dimensional algorithm which takes advantage of both the spatial and temporal information during the processing (e.g., the CLAP filtering conducted spatially on pixels in each data layer), and the linear regression of the look angle error done on pixels in time. In addition, manipulation of the three-dimensional information can improve the PS-SBAS performance significantly especially in presence of noise. For example, the 3D phase unwrapping algorithm in StaMPS uses a temporal and spatial smoothing to the spatial gradients of the nodes to derive the cost function for the statistic-cost network-flow phase unwrapping, which performs well especially when some SLC scenes are saturated with random noise. Nevertheless, in the presence of strong APS effects, the temporal smoothing may bias the

estimation, and thus results in a systematically deviated unwrapped phase, which is the case for the PS-SBAS processing for Okmok.

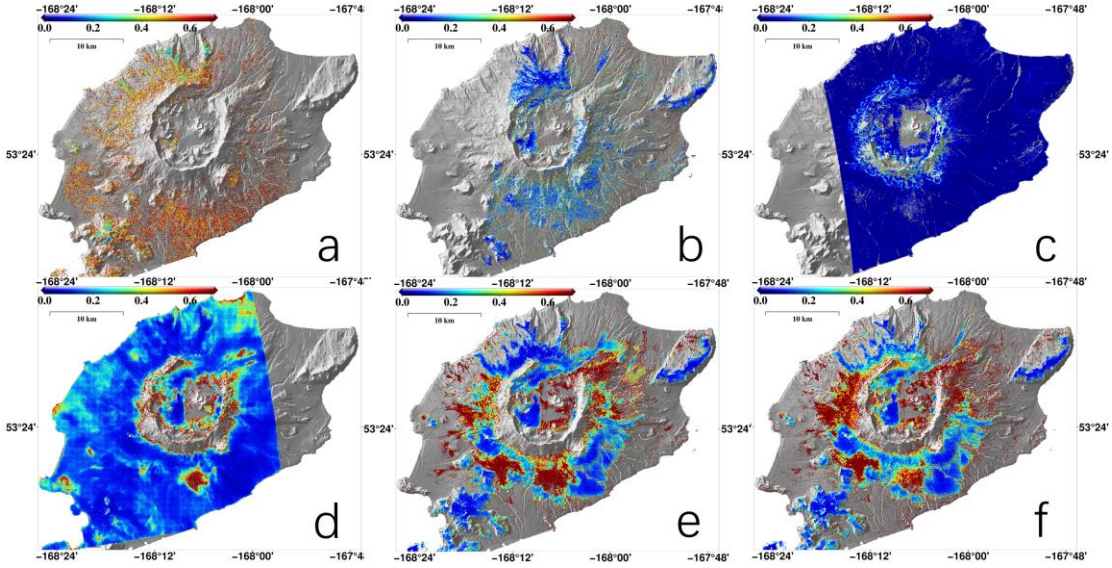

Figure 2.6. Unwrapping noise for the PS-SBAS processing: (a). Envisat P222, (b) TerraSAR-X P116, (c) ALOS-2 P92, (d) ALOS-2 P93, (d) Sentinel-1 P95, (e) Sentinel-1 P168.

Following the algorithms used in StaMPS, we employ the minimum standard deviation of the arc noise of each node as a representation of the noise for the computation nodes (Figure 2.6). The noise level around the inflation center inside the caldera is significantly lower than that outside the caldera for all the datasets except for the C-band Envisat, which is caused predominantly by the larger decorrelation effects associated with larger spatial baselines. Although the noise level is low for a considerable portion of areas away from the deformation center, the error can be cumulative in space and time using the network-approach phase unwrapping algorithm. Considering the noise level over the caldera rim is significantly high and our measurements near the locus are reliable (Figure 2.4), the measurement uncertainty in areas

away from the center caldera can be large. After the 3D phase unwrapping, the cumulative deformation is derived from the SBAS network in a least-square scenario. We use a simple estimator ρ to evaluate the SBAS processing noise:

$$\rho = \sum_{i=1}^{N} \left(\left| \frac{\phi_{sb}^{i} - \phi_{sb\_sim}^{i}}{\phi_{sb\_sim}^{i}} \right| \cdot \frac{|\phi_{sb\_sim}^{i}|}{\sum_{i=1}^{N} |\phi_{sb\_sim}^{i}|} \right)$$

where ϕ_{sb}^{i} is the i_{th} out of N unwrapped interferogram in the SBAS network, $\phi_{sb\_sim}^{i}$ is the i_{th} unwrapped interferogram calculated from the inverted single-referenced cumulative deformation map. ρ estimates the deviations of the unwrapped phase for each PS. Compared with the one derived from linear regression, ρ can be considered as a biased estimation of the signal to noise ratio (SNR) since $\phi_{sb\_sim}^{i}$ is just a biased estimate to the real cumulative displacements. A large ρ indicates a larger uncertainty in the unwrapped phase. Figure 2.7 illustrates the calculated ρ for each dataset. It is obvious that the noise level outside the caldera is significantly higher than that near the deformation locus for all the six InSAR tracks. The low ρ values in most area of the caldera suggest precise observations during the whole observation period. On the other hand, the good agreement between the InSAR data and GNSS records, especially the one located close to the deformation center, i.e., OKCE, suggests that our InSAR results have captured the temporal evolution of the deformation quite well and the derived displacements near the locus are reliable (figure 2.4). Outside the caldera, the volcanic deformation extends to a distance of several kilometers from the source to the volcano flank. The high ρ values in these areas indicate a rather wide distribution of points during the SBAS linear regression. Such results are still useful for the source inversion if the overall effects of the individual deviation are negligible. However, since the APS effects are spatially correlated in each interferograms and is not temporally independent as discussed before, the APS artifacts in a single scene are not normally distributed

and can be a catastrophe for determining the source parameters. For this reason, we have discarded signals outside the caldera to get a more persistent and accurate estimation of the deformation source.

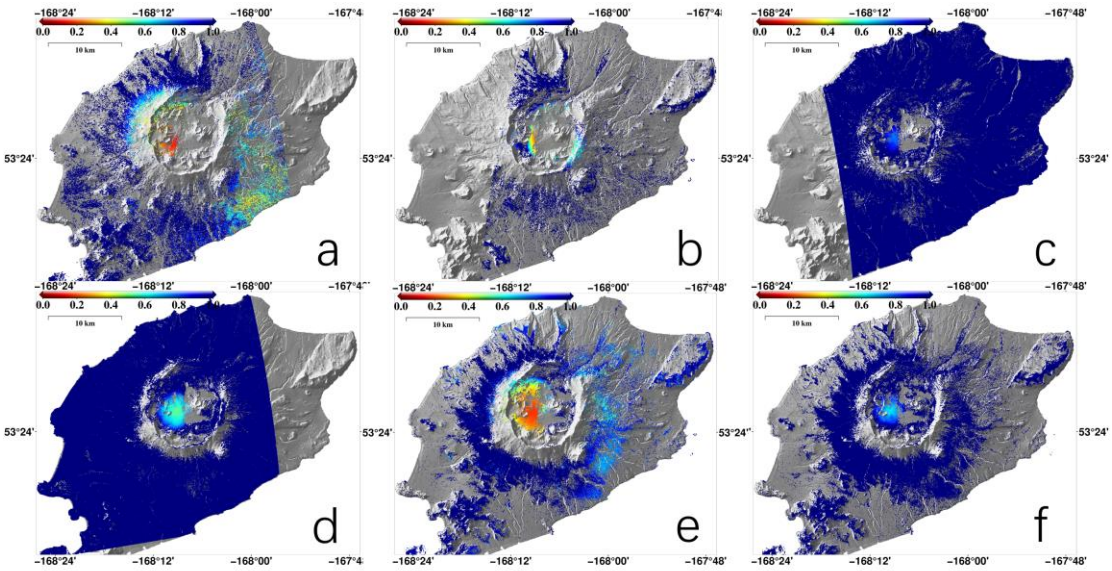

Figure 2.7. SBAS inversion noise ρ for the PS-SBAS processing: (a). Envisat P222, (b) TerraSAR-X P116, (c) ALOS-2 P92, (d) ALOS-2 P93, (d) Sentinel-1 P95, (e) Sentinel-1 P168.

Use of only deformation inside the caldera is verified for the Sentinel-1 P168 dataset. Source modeling is applied to both the full scene and the signal inside the caldera. The source parameters derived with signal inside the caldera are mostly consistent with the ones derived from the full scenes with only small deviations, indicating that the deformation inside the 10-km-wide caldera alone is enough to constrain the magma system. The inverted magma source models agree well with the previous studies before the 2008 eruption, especially with the previously InSAR derived models (e.g., Lu et al. 2005, 2010). Our results indicate the source accounting for the post-eruptive deformation of Okmok since the 2008 eruption is still the same

source which is responsible for the 1997 and 2008 eruptions and during the inter-eruption interval. The APS and decorrelation have always been a problem for modeling the magma source of Okmok over the Aleutian arc (Gong et al., 2015), our work in this paper may also provide some insights to the source modeling with time series InSAR data over areas with dense APS artifacts and decorrelation.

2.5.1 The stationary magma reservoir of Okmok

Using spaceborne SAR images acquired from six different imaging geometries at three frequency bands during 2008–2020 we have investigated the post-eruptive deformation of Okmok after the 2008 eruption. The produced deformation history shows that the Okmok started rapid reinflation with a persistent deformation rate of about 150 mm/yr within the first two years after the 2008 eruption, then slowed down to about 50 mm/yr during 2011–2013 and accelerated to about 90 mm/yr again during 2013–2014. The volcanic deformation rate was relatively steady from mid-2015 to about mid 2016 with a rate of about 50 mm/yr. From 2017 to mid-2019, the inflation rate increased again, with an average rate reaching about 100 mm/yr. Since mid-2019, the inflation rate decreased again to about 40 mm/yr. The episodic pulse of inflation at different rate resembles those of the pre- and inter-eruption deformation patterns of the 2008 and 1997 events of Okmok, which inflate periodically at time-varying rates with exponential patterns and were interpreted as responses to the magma accumulation in the shallow reservoir about 3 km BSL (Biggs et al., 2010; Lu et al., 2005, 2010). One major difference of the post-eruptive deformation after 2008 is that there is no period of quiescence as that during 1993–1996 and 2004–2007, which was interpreted as a critical state of pressurization for the reservoir where the surrounding hosting rocks are strong enough to temporarily retard the magma supply from depth (Lu et al., 2010). This persistent inflation pattern at a time-varying rate suggests a persistent

pressure gradient between the deep magma source and the shallow reservoir and a critical capacity of the magma reservoir beyond which the reservoir wall can no longer deform to accommodate the magma pressure has not yet reached since the 2008 eruption.

The episodic pulses of inflation at different rates are especially evident in the vertical components of the GNSS records. About five pulses of rapid inflation that slow down exponentially can be identified from the vertical GNSS records. The time varying inflation rates of a single pulse that decay exponentially in a single pulse can be possibly explained by a model where the shallow reservoir is fed by the magma flow from a deep source to compensate the pressure gradient (e.g., Lu et al., 2003, 2010). The episodic pulses may indicate that the pressure balance between the shallow reservoir and the deep source was broken at the end of the previous pulse. Several volcanic processes can produce this kind of pressure gradient behavior. First, injection of hot magma into the relatively colder reservoir is accompanied with crystallization, during which the hot melts cool down and contract. The decrease in volume will result in increased pressure gradient between the shallow magma reservoir and deep magma source. However, the time scale of crystallization is generally much larger than the period of episodic inflation (Caricchi et al., 2014), thus it cannot be solely responsible for the observed inflation pattern at Okmok. Degassing of excess volatiles from the cooling and crystallization of water-saturated magma may also contribute to the pressure decrease in the magma reservoir. Gas bubbles exsolve from the volatile-rich magma during crystallization, and the crystals tend to trap the gas bubbles. When the host rocks become permeable, gas can be expelled from the reservoir, which will result in pressure decrease in the reservoir. Another alternative explanation is that the pressure in the deep magma source might not be constant over time. The pressure in the deep source may increase episodically, which builds up episodic pressure gradient between the

reservoir and the magma source and produces an episodic inflation pattern at Okmok. Similar episodic inflations have also been observed at other volcanoes, some of these cases were interpreted using a temporal blockage in the magma migration pathway (Cervelli & Miklius, 2003). A transient interruption of magma supply may be caused by a short-lived blockage, which is believed to be produced by the convective overturns of the degassed crystallized magma in the reservoir. The denser magmas move downward and tend to impede the magma flow from the pathway to the shallow reservoir. Upon removal, another episode of inflation begins. Whether these processes can occur in the magma system is still unknown, further investigations are still needed to test these hypotheses.

As mentioned above, spatially correlated APS effects are prone to saturate the InSAR results outside the caldera and compromise the source inversion significantly, especially when the APS can reach a magnitude comparable to the deformation signal. In our case, the signals outside the caldera with dense APS are masked out, and the deformation time series are modeled with numerical FEMs and a best fit magma source is found located at about 3.5 km beneath the caldera floor, which agrees well with the previous studies (Biggs et al., 2010; Lu et al., 2005, 2010), suggesting the same magma source accounting for the progressive pre- and inter-eruptive deformation of the 1997 and 2008 eruption. Qu et al. (2015) mapped the post-eruptive deformation during 2008–2014 and found a Mogi source embedded about 4 km beneath the caldera center, which is about 1 km deeper than previous studies conducted with InSAR. Using the same datasets, Xue et al. (2020) identified significant deviations between the GNSS and InSAR results inside the caldera near the locus and interpreted them as localized deformation possibly related to self-compaction and erosion of new tephra by the 2008 erosion and viscoelastic relaxation and thermo-elastic cooling from older lava flows. After masking the

signals inside the caldera where the InSAR and GNSS are not compatible and combined with GNSS records, a Mogi source located about 3.2 km together with a shallow sill was used to account for the post-eruptive deformation. However, we have recomputed the deformation history during 2008–2014 with the same datasets (i.e., the C-band Envisat P222 and X-band TerraSAR-X P116 track) using the PSInSAR processing procedure deployed in this study and found good agreements between the InSAR and GNSS. Also, results from C-band Sentinel-1 and L-band ALOS-2 show little deviation to the GNSS records since 2015, indicating that our mapped deformation inside the caldera is accurate for the source inversion. The source depth accounting for the inflation immediately after the 2008 eruption in our study is very close to that before 2008, which is consistent with the progressive deepening in the deflation source during the 2008 eruption in previous inter-eruption observations by Lu and Dzurisin (2010) and Freymueller and Kaufman (2010), indicating magma accumulation inside the shallow reservoir resumed rapidly after the eruption. The inferred locations of the magma reservoir from InSAR coincide with the low seismic velocity zone inferred from seismic radial anisotropy and resistivity survey (Miller et al., 2020).

2.5.3 Erosion of the 2008 Tephra Deposits

Although the erosion of the unconsolidated tephra deposits cannot be mapped directly, our InSAR results can still provide some insights into it. Since the 2008 eruption, the dense volcanic sediments inside the caldera have become a pervasive and insurmountable problem for deformation mapping with InSAR. Rapid surface changes associated with erosion of the deposits would degrade the interferometric coherence. For the identification of PS using SAR datasets with small perpendicular baselines, the spatial coverage of PS represents basically the area without significant temporal changes. Our InSAR observations cover only a small portion inside

the caldera and no coherent measurements can be obtained near Cone D (Figure 2.3), which produced the 2008 phreatomagmatic eruption and is deposited with tephra to a thickness of 25–50 m (Larsen et al., 2015). The PS coverage of the C-band Envisat P222 right after the 2008 eruption is less than that of the X-band TerraSAR-X which started about two years after the eruption. Considering that the decorrelation associated with surface erosion is stronger for the X-band sensor (e.g., Hanssen, 2001; Wei & Sandwell, 2010), our results indicate that the erosion and consolidation of the tephra materials evolved rapidly in the first two years after the eruption. Also, the spatial extent of PS in the C-band Sentinel-1 or L-band ALOS-2 covers most of the caldera area except for the region near cone D and water bodies in the east caldera, suggests that large scale of sediment erosion that reshaped the surface rapidly after the 2008 eruption has ceased in these areas since 2015.

2.5.4 Magma Supply Dynamics

The InSAR deformation history can be well modeled by a simple spherical pressure source which is relatively stationary through time and is consistent with the calculated pressure source prior to the 2008 eruption. Lu and Dzurisin (2010) suggests a shallow contracting sill at a depth ~0.5 km during the 2008 eruption and they interpreted this as the extraction of ground water which was responsible for the phreatic nature of the 2008 eruption. Freymueller and Kaufman (2010) also detected changes in the magma source immediately before and during the 2008 eruption; they suggest that these variations are related to preexisting magma storage at shallower depths prior to 1997, with a more chemically evolved magma that accounts for the slightly higher SiO2 content and 2–3 times larger eruption volume. We cannot evaluate the possibility of the existence of such a shallower structure with only the coherent InSAR observations from 2008 to 2014 due to the lack of spatial coverage near the center of the caldera, where the shallow sill

was thought to reside (Lu & Dzurisin, 2010; Xue et al., 2020). However, starting from 2015, the availability of Sentinel-1 and ALOS- 2 data enables a larger spatial coverage than the Envisat and TerraSAR-X. We have detected no localized deformation that is indicative of shallower sources for this time range. Hence, the shallower sill structure discussed in Freymueller and Kaufman (2010) and Lu and Dzurisin (2010) was likely a transient process associated with the 2008 eruption.

The 2008 eruption was significantly different from its predecessors. We compared the post-eruptive magma accumulation with that during the inter-eruptive period from 1997 to 2008 (Figure 2.8). The rapid magma replenishment occurred immediately after the 1997 and the 2008 eruptions and both show episodic patterns with time-varying rates decaying exponentially. We notice that the magma intrusion rate after the 2008 eruption is almost three times of that after the 1997 eruption. Consider a conceptual model widely used for Okmok and other shield volcanoes in the Aleutian where the shallow reservoir is fed by the magma flow from a deep source to compensate the pressure gradient (e.g., Lu et al., 2003, 2010). The much larger post-eruption magma replenishment rate indicates a reduction in the resistance inside the magma transport pathway from the deep source to the shallow reservoir after the 2008 eruption, or that the pressure difference between the shallow reservoir and the deep source after the 2008 eruption is much higher than after the 1997 eruption. Whether and how the extrusion of magma in the shallow reservoir during the 2008 eruption can affect the deep magma migration pathway remains uncertain. We are inclined to suggest that the increase in the pressure difference following the 2008 eruption is the result of a pressure decrease in the shallow reservoir assuming the pressure in the deep magma source remains constant. Hence, the much higher inflation rate after the 2008 eruption may be the result of a larger pressure deficit in the shallow reservoir as

the eruption volume from the 2008 eruption was much greater than that of the 1997 eruption. The cumulative volume change after the 2008 eruption also indicates a much higher magma accumulation rate; ~0.08 km3 of magma has been intruded into the shallow reservoir from 2008 until 2020, which is about twice the rate observed from 1997 to 2008. Along with the post-eruptive surface deformation, which can be well determined by the spherical source, we speculate that the increase in the eruptive volume associated with the 2008 eruption relative to the prior historical eruptions from Cone A is likely resulted from over-extrusion of magma in the shallow reservoir during the 2008 eruption. The over-extrusion during the eruption thus causes a possible greater reduction in magma pressure compared to the 1997 eruption, which subsequently leads to a higher magma replenishment rate and large inflation rate.

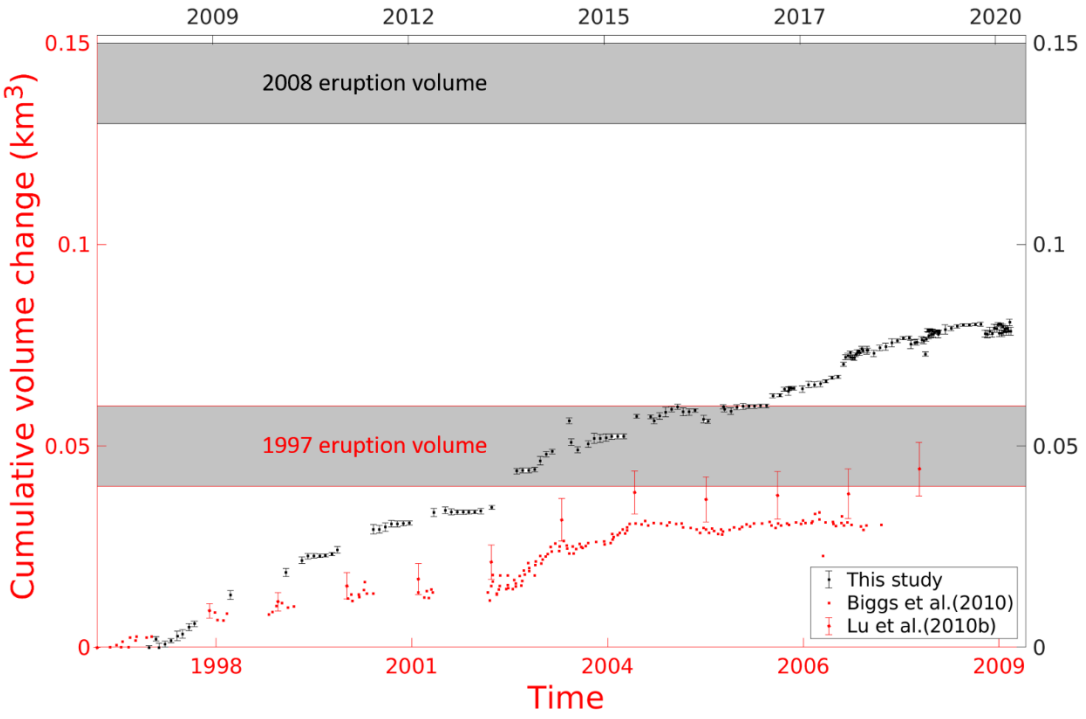

Figure 2.8. Comparison of the cumulative volume change since 2008 with that during 1997–2008. The 1997 eruption volume is from Lu et al. (2005), the 2008 eruption volume is the co-eruptive volume change from Lu and Dzurisin (2014). The data in this study are plotted with respect to the axes on the top and the right; the volume changes from 1997 to 2008 from Biggs et

al. (2010) and Lu and Dzurisin (2010) are plotted with respect to the axes on the bottom and the left.

The over-extrusion may be a result of a change in the mechanism of the magma ascent from the reservoir to the surface as discussed in Larsen et al. (2015), where the magma migration pathway changed from a single, narrow shallow conduit that connecting the reservoir with Cone A to a dike-fed system tapping a larger portion of the eruptible magma from storage. This is consistent with the inter- and co-eruptive seismicity distribution associated with the 2008 eruption (Ohlendorf et al., 2014). We infer that the two earthquake swarms located beneath Cone A and Cone D recorded during the period from early 2003 to July 6, 2008, and from 6 to 13 2008, respectively, are indicative of brittle failure associated with the magmatic fluid migration. The distinctly different event locations are evidence of different magma ascent pathways accounting for the 1997 and the 2008 eruptions. An alternative explanation involves the phreatomagmatic nature of the 2008 eruption. Lu et al. (2010) identified minor deflations during the inter-eruptive period from 2004 to 2005, which was associated with the outgassing of volatiles. Signals of localized deflation during the 2008 eruption were also identified and attributed as the withdrawal of ground water (Lu & Dzurisin, 2010). The exsolution of magmatic volatiles may fracture the host rocks of the spherical magma source and shallower ground water reservoir, making it possible for explosive interaction between the magma and the ground water, which further fracture the magma migration pathway and finally produced the explosive eruption and the significantly large eruption volume. A schematic illustrating the two hypotheses above is shown in Figure 2.9.

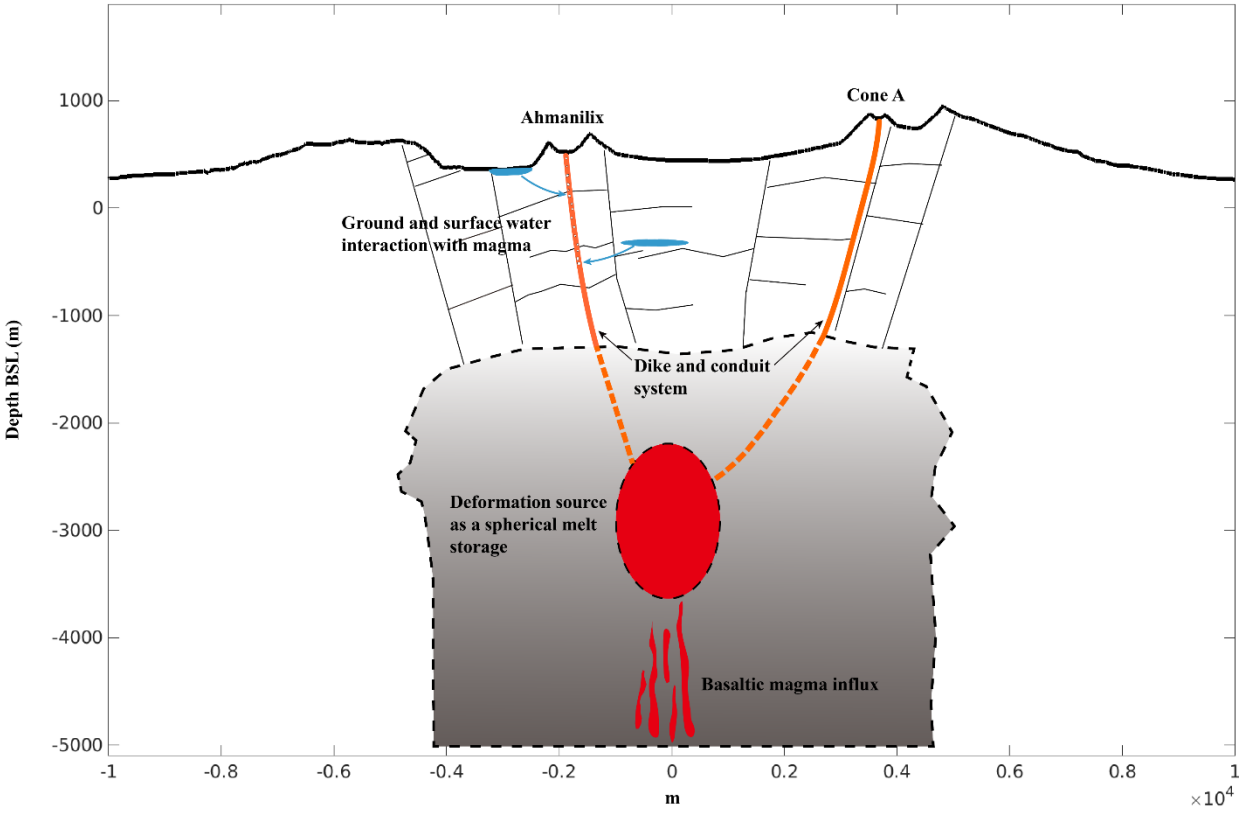

Figure 2.9. Schematic cross section through Okmok along Cone A and Ahmanilix illustrating the mechanism for the proposed over extrusion. The 2008 eruption was possibly fed by dike systems well evolved during the caldera collapse. Interaction between the magma ascent and ground and surface water may have also contributed to the large eruption volume.

The cumulative volume change inside the shallow reservoir until 2020 is about 60% of the total reservoir volume change during the 2008 eruption ($\sim 0.08\ km^3$). The 2008 eruption occurred when the volume of magma withdrawn during the 1997 eruption was almost replenished (Figure 2.8), which may imply that the triggering condition of an eruption is when the reservoir capacity is reached. In addition, declining inflation rates that last for a few years prior to the eruption and a period of oscillations including deflation and inflation may also serve as an indication that an eruption draws near (Fournier et al., 2009; Lu et al., 2010). Since 2019,

the inflation rate at Okmok decreased to about 40 mm/yr, which is the lowest since the 2008 eruption and is close to that during the pre-eruptive inflation during 1993–1995. Therefore, continuous monitoring ground deformation at Okmok volcano is critically important in the future. Even if surface deflation such as that observed during 2004–2005 were detected at Okmok, without knowledge of the magma pressure in the shallow reservoir and the deep source, it is difficult to determine whether the decreasing inflation rate is an indication of an imminent critical pressure state or just another tail of the exponential decaying magma replenishment cycle as those during 2011–2013 and 2015 to 2016. Limited by the over-simplified nature of the models we use, further understanding of the volcanic system can be achieved only when the realistic physical processes critical for the volcanic life cycles are considered, for example, compressibility of the magma, melt viscosity, degassing and crystallization, which require assimilation of multi-disciplinary data such as tomography of the sub-caldera structure from seismology and magma evolution from geochemical research.

2.6 Conclusion

In this paper, we have mapped the inflation of Okmok volcano after the 2008 eruption with the PS-SBAS method. Multi-temporal SAR datasets from C-band Envisat and Sentinel-1, X-band TerraSAR-X and L-band ALOS-2 over long-period observations allow us to produce deformation time-series with high accuracy within the caldera, despite the dense APS artifacts contamination. The generated deformation history indicates Okmok has been inflating at a time-varying rate ranging from about 30-150 mm/yr since after the 2008 eruption, which agrees well with the GNSS records. We then track the magma system evolution with EnKF using a spherical incompressible pressure source. The results suggest that the volcanic deformation can be explained well by a source located about 3 km BSL at the center of the caldera with little

variations in lateral positions, which we believe, is the same source that produced the 1997 and 2008 eruptions and the surface deformation associated with them. The cumulative volume change accounting for the inflation is about $0.08\ km^3$ from 2008 to 2020, which is about 160% and about 60% of the total reservoir volume changes during the 1997 and the 2008 eruptions, respectively.

The dense SAR data acquisitions from spaceborne SAR sensors such as Sentinel-1 provides critical constraints for the mapping of volcanic deformation, and EnKF is a promising tool to assimilate the time-series deformation for the determination of source location and the tracking of temporal evolution of the source strength. The combination of InSAR and EnKF provides an exquisite approach to update the source evolution of volcanoes for hazards forecasting and prevention. However, although elegant source modeling can be produced with current workflow and datasets, limitations still remain. For example, the poor data coverage in certain areas due to decorrelation in long-term observations may compromise the performance of EnKF as that in our study during 2008 to 2014, no coherence for winter acquisitions of C-band SAR can make it difficult to track the deformation continuously, saturation of dense APS artifacts may degrade the data coverage significantly in order to get robust inversions. Hopefully, this situation can be solved provided high interferometric-quality SAR data, e.g., the future NISAR mission, and new algorithms that are capable of dealing with decorrelation and APS contaminations.

2.7 Acknowledgments, Samples, and Data

This research is funded by NASA Earth Surface & Interior Program (80NSSC19K0357), NASA NISAR Science Team (80NSSC19K1491), and the Shuler-Foscue Endowment at the Southern Methodist University. ALOS-2 PALSAR-2 datasets are copyrighted and provided by

Japan Aerospace Exploration Agency's via the 2nd Research Announcement on the Earth Observations (PI No. ER2A2N061).

2.8 References

Albright, J. A., Gregg, P. M., Lu, Z., & Freymueller, J. T. (2019). Hindcasting magma reservoir stability preceding the 2008 eruption of Okmok, Alaska. *Geophysical Research Letters*, *46*, 8801 – 8808. https://doi.org/10.1029/2019GL083395

Biggs, J., Lu, Z., Fournier, T., & Freymueller, J. T. (2010). Magma flux at Okmok volcano, Alaska, from a joint inversion of continuous GPS, campaign GPS, and interferometric synthetic aperture radar. Journal of Geophysical Research, 115, B12401. https://doi.org/10.1029/2010JB007577

Blewitt, G., Hammond, W. C., & Kreemer, C. (2018). Harnessing the GPS data explosion for interdisciplinary science. Eos, 99. https://doi.org/10.1029/2018EO104623

Byers, F. M. (1959). Geology of Umnak and Bogoslof Islands, Aleutian Islands, Alaska (pp. 267 – 369). U.S. Geological Survey Bulletin B; U.S.Government Printing Office.

Caricchi, L., Biggs, J., Annen, C., & Ebmeier, S. (2014). The influence of cooling, crystallization and re-melting on the interpretation of geodetic signals in volcanic systems. Earth and Planetary Science Letters, 288, 166 – 174. https://doi.org/10.1016/j.epsl.2013.12.002

Cervelli, P., & Miklius, A. (2003). The shallow magmatic system of Kilauea volcano. In C. Heliker et al. (Eds.), The Pu‘u ‘O‘o-Kupaianaha eruption of Kilauea volcano, Hawai‘i: The first 20 years. (pp. 149 – 164), Prof. Pap. 1676, U.S. Geol. Surv, Reston, Virginia.

Evensen, G. (2003). The ensemble Kalman filter: Theoretical formulation and practical implementation. Ocean Dynamics, 53, 343 – 367. https://doi.org/10.1007/s10236-003-0036-9

Evensen, G. (2009). Data assimilation: The ensemble Kalman filter (2nd ed.). Springer. https://doi.org/10.1007/978-3-642-03711-5

Ferretti, A., Prati, C., & Rocca, F. (2001). Permanent scatterers in SAR interferometry. IEEE Transactions on Geoscience and Remote Sensing, 39(1), 8 – 20. https://doi.org/10.1109/36.898661

Fournier, T., Freymueller, J., & Cervelli, P. (2009). Tracking magma volume recovery at Okmok volcano using GPS and an unscented Kalman filter. Journal of Geophysical Research, 114, B02405. https://doi.org/10.1029/2008JB005837

Freymueller, J. T., & Kaufman, A. M. (2010). Changes in the magma system during the 2008 eruption of Okmok volcano, Alaska, based on GPS measurements. Journal of Geophysical Research, 115, B12415. https://doi.org/10.1029/2010JB007716

Gong, G., Meyer, F., Lee, C. W., Lu, Z., & Freymueller, J. (2015). Measurement and interpretation of subtle deformation signals at Unimak Island from 2003 to 2010 using Weather Model-Assisted Time Series InSAR. Journal of Geophysical Research: Solid Earth, 120, 1175 – 1194. https://doi.org/10.1002/2014JB011384

Gregg, P. M., & Pettijohn, J. C. (2016). A multi-data stream assimilation framework for the assessment of volcanic unrest. Journal of Volcanology and Geothermal Research, 309, 63 – 77. https://doi.org/10.1016/j.jvolgeores.2015.11.008

Hanssen, R. F. (2001). Radar interferometry: Data interpretation and analysis. Kluwer Acad.

Hooper, A. (2008). A multi-temporal InSAR method incorporating both persistent scatterer and small baseline approaches. Geophysical Research Letters, 35, L16302. https://doi.org/10.1029/2008GL034654

Hooper, A., Segall, P., & Zebker, H. (2007). Persistent scatterer interferometric synthetic aperture radar for crustal deformation analysis, with application to Volcan Alcedo, Galapagos. Journal of Geophysical Research, 112, B07407. https://doi.org/10.1029/2006JB004763

Hooper, A., Zebker, H., Segall, P., & Kampes, B. (2004). A new method for measuring deformation on volcanoes and other natural terrains using InSAR persistent scatterers. Geophysical Research Letters, 31, L23611. https://doi.org/10.1029/2004GL021737

Hooper, A., & Zebker, H. A. (2007). Phase unwrapping in three dimensions with application to InSAR time series. Journal of the Optical Society of America. A, 24, 2737. https://doi.org/10.1364/JOSAA.24.002737

Kalman, R. E. (1960). A new approach to linear filtering and prediction problems. Journal of Fluids Engineering, 82, 35–45. https://doi.org/10.1115/1.3662552

Larsen, J. F., Neal, C., Schaefer, J., Beget, J., & Nye, C. (2007). Late Pleistocene and Holocene caldera-forming eruptions of Okmok Caldera, Aleutian Islands, Alaska. In J. Eichelberger, E. Gordeev, P. Izbekov, M. Kasahara, & J. Lees (Eds.), Volcanism and subduction: The Kamchatka region (pp. 343–364). https://doi.org/10.1029/172GM24

Larsen, J. F., Neal, C. A., Schaefer, J. R., Kaufman, A. M., & Lu, Z. (2015). The 2008 phreatomagmatic eruption of Okmok Volcano, Aleutian Islands, Alaska: Chronology, deposits, and landform changes. Alaska Division of Geological & Geophysical Surveys Report of Investigation 2015-2, 53 p. https://doi.org/10.14509/29405

Larsen, J. F., Śliwiński, M., Nye, C., Cameron, C., & Schaefer, J. R. (2013). The 2008 eruption of Okmok Volcano, Alaska: Petrological and geochemical constraints on the subsurface magma plumbing system. Journal of Volcanology and Geothermal Research, 264, 85–106. https://doi.org/10.1016/j.jvolgeores.2013.07.003

Lu, Z., & Dzurisin, D. (2010). Ground surface deformation patterns, magma supply, and magma storage at Okmok volcano, Alaska, from InSAR analysis: 2. Coeruptive deflation, July–August 2008. Journal of Geophysical Research, 115, B00B02. https://doi.org/10.1029/2009JB006970

Lu, Z., & Dzurisin, D. (2014). In InSAR Imaging of Aleutian Volcanoes: Monitoring a Volcanic Arc from Space. Springer Praxis Books, Geophysical Sciences. Springer. https://doi.org/10.1007/978-3-642-00348-6

Lu, Z., Dzurisin, D., Biggs, J., Wicks, C., & McNutt, S. (2010). Ground surface deformation patterns, magma supply, and magma storage at Okmok volcano, Alaska, from InSAR analysis: 1. Intereruption deformation, 1997–2008. Journal of Geophysical Research, 115, B00B03. https://doi.org/10.1029/2009JB006969

Lu, Z., Mann, D., Freymueller, J. T., & Meyer, D. J. (2000). Synthetic aperture radar interferometry of Okmok volcano, Alaska: Radar observations. Journal of Geophysical Research, 105(B5), 10791–10806. https://doi.org/10.1029/2000JB900034

Lu, Z., Masterlark, T., & Dzurisin, D. (2005). Interferometric synthetic aperture radar study of Okmok volcano, Alaska, 1992–2003: Magma supply dynamics and post-emplacement lava flow deformation. Journal of Geophysical Research, 110(B2), 0148–0227. https://doi.org/10.1029/2004JB003148

Lu, Z., Masterlark, T., Dzurisin, D., Rykhus, R., & Wicks, C. (2003). Magma supply dynamics at Westdahl volcano, Alaska, modeled from satellite radar interferometry. Journal of Geophysical Research, 108(B7), 2354. https://doi.org/10.1029/2002JB002311

Mann, D., Freymueller, J., & Lu, Z. (2002). Deformation associated with the 1997 eruption of Okmok volcano, Alaska. Journal of Geophysical Research, 107(B4), ETG 7-1–ETG 7-12. https://doi.org/10.1029/2001JB000163

McConnell, J. R., Sigl, M., Plunkett, G., Burke, A., Kim, W. M., Raible, C. C., et al. (2020). Extreme climate after massive eruption of Alaska's Okmok volcano in 43 BCE and effects on the late Roman Republic and Ptolemaic Kingdom. Proceedings of the National Academy of Sciences of the United States of America, 117(27), 15443–15449. https://doi.org/10.1073/pnas.2002722117

Miller, D., Bennington, N., Haney, M., Bedrosian, P., Key, K., Thurber, C., et al. (2020). Linking magma storage and ascent to eruption volume and composition at an arc caldera. Geophysical Research Letters, 47, e2020GL088122. https://doi.org/10.1029/2020GL088122

Murray, K., Bekaert, D., & Lohman, R. (2019). Tropospheric corrections for InSAR: Statistical assessments and applications to the Central United States and Mexico. Remote Sensing of Environment, 232, 111326. https://doi.org/10.1016/j.rse.2019.111326

Ohlendorf, S. J., Thurber, C. H., Pesicek, J. D., & Prejean, S. G. (2014). Seismicity and seismic structure at Okmok Volcano, Alaska. Journal of Volcanology and Geothermal Research, 278-279, 103–119. https://doi.org/10.1016/j.jvolgeores.2014.04.002

Porter, C., Morin, P., Howat, I., Noh, M. J., Bates, B., Peterman, K., et al. (2018). ArcticDEM. Harvard Dataverse, v1. https://doi.org/10.7910/DVN/OHHUKH

Qu, F., Lu, Z., Poland, M., Freymueller, J., Zhang, Q., & Jung, H.-S. (2015). Post-eruptive inflation of Okmok volcano, Alaska, from InSAR, 2008–2014. Remote Sensing, 7(12), 15839–16794. https://doi.org/10.3390/rs71215839

Wei, M., & Sandwell, D. T. (2010). Decorrelation of L-Band and C-Band interferometry over vegetated areas in California. IEEE Transactions on Geoscience and Remote Sensing, 48, 2942–2952. https://doi.org/10.1109/TGRS.2010.2043442

Xue, X., Freymueller, J., & Lu, Z. (2020). Modeling the posteruptive deformation at Okmok based on the GPS and InSAR time series: Changes in the shallow magma storage system. Journal of Geophysical Research: Solid Earth, 125, e2019JB017801. https://doi.org/10.1029/2019JB017801

Zhan, Y., & Gregg, P. M. (2017). Data assimilation strategies for volcano geodesy. Journal of Volcanology and Geothermal Research, 344,13–25. https://doi.org/10.1016/j.jvolgeores.2017.02.015

CHAPTER 3
EVOLUTION OF THE MAGMA SYSTEM AT MAKUSHIN VOLCANO, ALASKA, FROM 2004 TO 2021

3.1 Abstract

Located in the northeast of Unalaska Island in the central part of the Aleutian, Alaska, Makushin volcano is one of the more active volcanoes in the United States, with the most recent eruption occurred in 1995. Pre-eruptive inflation and post-eruptive deflation were identified from 1993 to 1995 and 1996 to 2000, respectively, and were interpreted as volume changes associated with magma movement within the plumbing system. In this study, we investigate the surface deformation of Makushin from 2004 to 2021 to evaluate its present-day activity, using Synthetic Aperture Radar (SAR) interferometry technique. SAR images acquired from C-band Envisat and Sentinel-1, X-band TerraSAR-X, and L-band ALOS-2 satellites are analyzed using an advanced multiple temporal Interferometric SAR (InSAR) algorithm. The produced deformation time series are then used to track the temporal evolution of the volcanic system with Ensemble Kalman Filter (EnKF) assuming Mogi sources. The results show that Makushin is characterized by time-varying deformation episodes including quiescence, and inflation/deflation cycles at varied rates since 2004. The derived deformation histories can be well reproduced by a spatially stationary pressure source located to the east-northeast of the summit, at a depth of about 6 km beneath the sea level (BSL). The inflation/deflation cycles with distinct temporal patterns are interpreted as results from volatile-dominated volume accumulation/loss in the magmatic reservoir. A secondary reservoir connected to the main magma chamber is revealed from the

deformation time series. No surface displacement associated with the large earthquake swarm in 2020 is identified from the InSAR-derived deformation. The cumulative volume change in the magma reservoir is about $-6 \times 10^6\ m^3$ from 2004 to 2021, indicating a volume/pressure deficit in the magma plumbing system.

3.2 Introduction

The 2500-km-long Aleutian Island Arc, produced by subduction of the Pacific Plate beneath the North American plate, holds more than 50 historically active volcanoes which produce an average of about two eruptions each year since the 1950s (Miller et al., 1998). Although the volcanoes of the Aleutian Arc are remote in terms of population, more than 70,000 passenger and cargo flights fly in circumpolar air routes over the region each year (Dean et al., 1998). Additionally, activity from eruptions impacts local populations, industry, and fisheries. The Aleutian Arc's remote location poses difficulties in effectively monitoring its active volcanic systems for early eruption warnings. The establishment of permanent stations, as well as the increasing availability of remote-sensed data, provide valuable insights for the investigation of the complex magma plumbing systems and tracking their temporal evolution for hazard forecasting and mitigation.

Mount Makushin, located on the northwestern part of Unalaska Island in the central Aleutians (Figure 3.1), is among one of the more active volcanoes in the Aleutians (Lu and Dzurisin, 2014). Recent seismicity monitoring revealed a large swarm of earthquakes located about 12 km southeast of the summit at a depth of 7 to 10 km BSL from June to September 2020 (Lanza et al., 2022). The 2020 earthquake swarm is the largest seismicity surge recorded at Makushin since the last eruption in 1995 and has led to concerns about possible impending eruptions. In this study, we focus on mapping the surface deformation history of the Makushin

volcano with SAR data collected across platforms from 2004 to 2021, using time-series InSAR techniques, and investigation of the magma plumbing systems and their temporal evolution with deformation modeling using EnKF.

3.3 Background

The Makushin volcano is a large, truncated stratovolcano with an ice cap on its summit at an elevation of about 1800 m. The current landscape of Makushin volcano formed during two eruptive periods separated by an interval of pronounced erosion (Drewes et al., 1961). The first episode can be dated back to Pliocene or early Pleistocene time, during which extensive flow and subordinate pyroclastic deposits of basaltic and andesitic composition were produced (Drewes et al., 1961; Wood and Kienle, 1990). Preceding the early Holocene, multiple large eruptions including two caldera-forming events produced the current summit caldera, several satellite flank vents, and active fumaroles (McConnell et al., 1997).

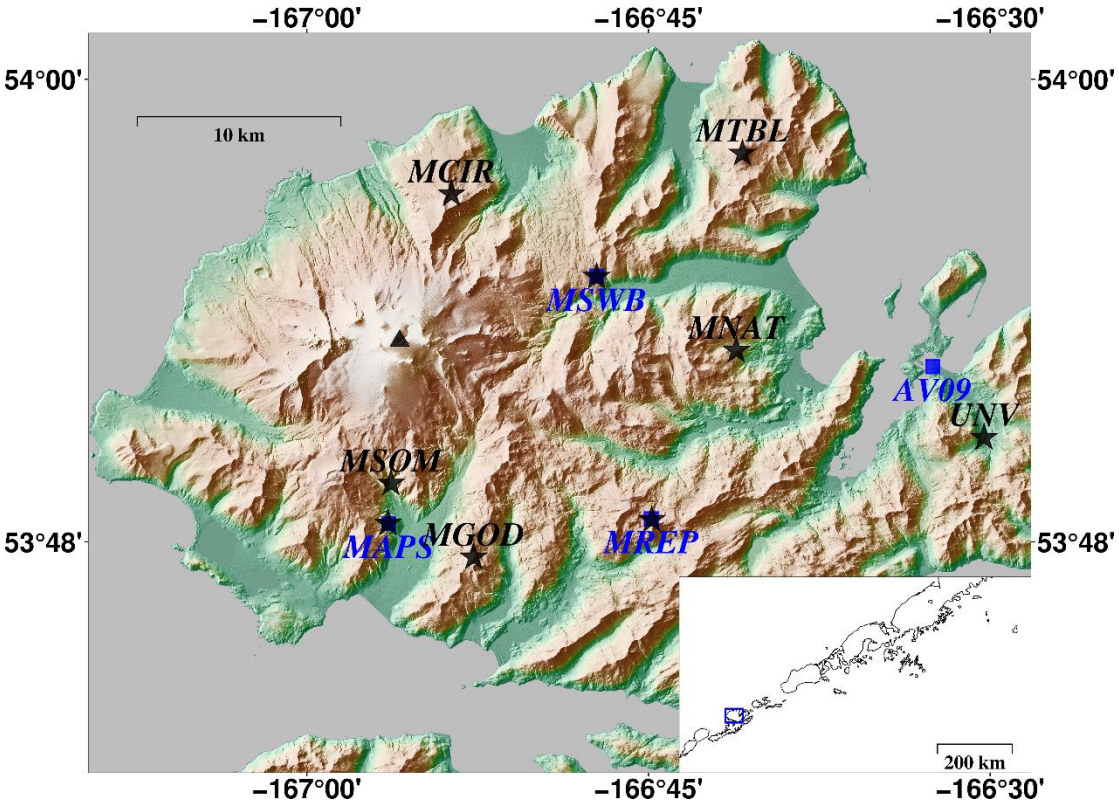

Figure 3.1. Shaded relief of Makushin volcano. The black triangle represents the caldera summit, which is further used as the reference point in deformation modeling. The blue squares are the continuous GNSS stations. Black pentagrams represent the continuous seismic stations. The inset shows the location of the Makushin volcano in the Aleutian arc.

Since the late 1700s, more than 18 eruptions have been produced from the summit caldera of Makushin volcano (Miller et al., 1998; McConnell et al., 1997), with a relatively small VEI of 1-3 (Miller et al., 1998). The latest eruptive activity, which occurred in January 1995 and lasted only for a few hours, is a small eruption with a maximum VEI of 1. A small steam and ash cloud rising to ~ 2.4 km was reported by pilots. Additionally, a thin layer of ash deposited in the snow on the upper south flank as well as volcanic ejecta covering the summit area were observed in a geologic mapping survey conducted in the summer of 1996. Although not as active as some of

its neighboring Aleutian volcanoes which have produced several explosive eruptions during the last century (e.g., Okmok), Makushin still poses a significant hazard to the local communities on the Unalaska Island, fishery and nautical infrastructures in the Dutch Harbor, and passengers and cargos traversing the north Pacific air routes.

Geodetic monitoring of surface deformation at Makushin has been ongoing since the early 1990s. SAR images from ERS-1 and ERS-2 satellites taken in the summer of 1993 and each year from 1995 to 2000 have been previously analyzed to measure the surface displacements using two-pass InSAR (Lu et al., 2002). Results from previous efforts indicate an edifice-wide uplift of ~ 7 cm centered at the east flank from 1993 to 1995 followed by minor subsidence near the upper flank from 1995 to 2000 (Lu et al., 2002). Subsequent SAR images from 2003 to 2010 collected from the Envisat satellite revealed persistent subsidence with a maximum average rate of ~ 1 cm/yr centered near the active inflation center from 1993 to 1995 (Lu and Dzurisin., 2014). Using observations from the Global Navigation Satellite System (GNSS), Xue et al. (2020) found that the Makushin was inflating from 2016-2018 at a similar rate as that during 2001-2004, after being relatively quiescent without producing significant displacements from 2010 to 2015. Despite the distinct displacement behavior during different periods, the deformation signals can be reproduced by a Mogi source, i.e., a point source embedded in a homogeneous and isotropic elastic half-space (Mogi, 1958), located ~ 6 km BSL, indicating a potentially long-lived pressure source with complicated magmatic processes (Lu et al., 2002; Lu and Dzurisin, 2014; Xue et al., 2020).

Real-time seismological monitoring of the Makushin volcano started in 1996. The current permanent network comprises eight continuous seismometers maintained by the Alaska Volcano Observatory (AVO) and one operated by the University of Alaska, Fairbanks (UAF). Seismic

observations indicate that the seismicity is distributed among several clusters beneath or beyond the summit area (Syracuse et al., 2015; Power et al., 2019, 2020; Lanza et al., 2022). Consistent with the geodetic observations, seismic tomography studies reveal a broad region with low P wave velocity (V_P) and high attenuation located slightly offset from the volcano summit, with a depth between 5 to 7 km BSL, indicating the presence of a melt-rich magma body (Syracuse et al., 2015; Lanza et al., 2020).

3.4 Data and Methods

3.4.1 Dataset

In this study, SAR images collected from different platforms and operation bands are used to map the deformation history from 2004 to 2021 (Figure 3.2). The C-band Envisat track P408 spans the period from 2004 to 2010. The X-band TerraSAR-X data was acquired from 2011 to 2015. The C-band Sentinel-1 and L-band ALOS2 data cover the period from about 2015 to 2021. To alleviate the decorrelation effect due to snow and ice cover in the summit area, we focus on scenes acquired in summer from June to October (Lu and Dzurisin 2014). Deformation time series are produced with PSInSAR to track the temporal evolution of the magma source (Hooper et al., 2004). Starting from 2011, three continuous Global Navigation Satellite System (cGNSS) stations have been deployed at Makushin volcano, i.e., MAPS, MREP and MSWB (Freymueller et al., 2011, 2012a, 2012b; cleaned data download from AVO website: https://apps.avo.alaska.edu/geodesy/public; Figure 3.1). After the correction for tectonic displacements by subtracting measurements from the baseline site which sits away from the volcano and thus is free of volcanic deformation, i.e., AV09 (UNAVCO, 2004), observations from these cGNSS stations are used for both validation of the InSAR measurements and magma source modeling.

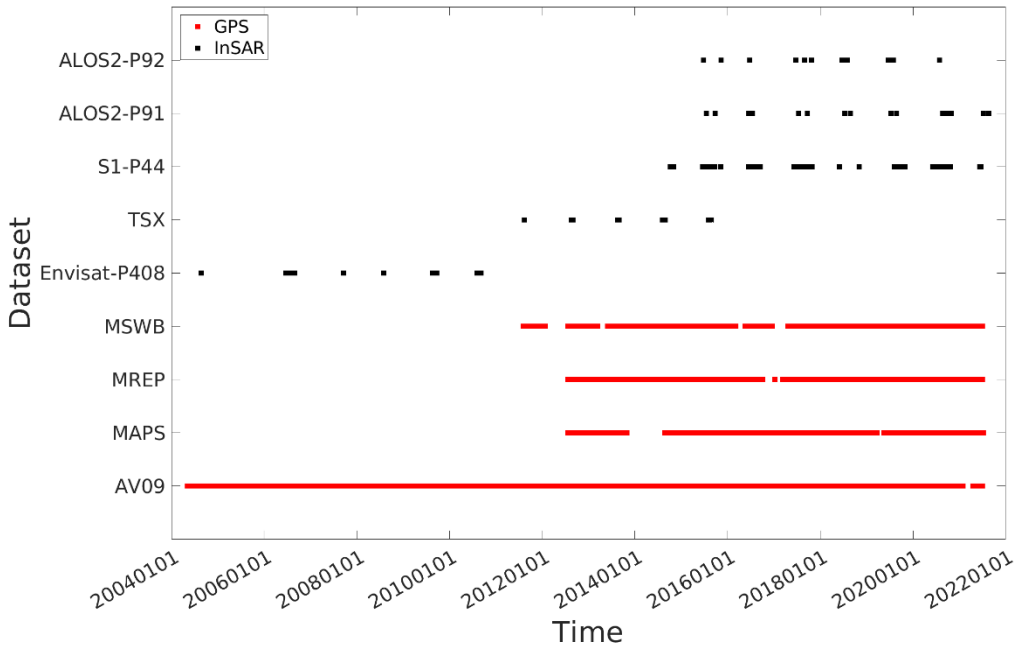

Figure 3.2. Temporal coverage of SAR and cGNSS data used in this study. All SAR images are taken from summertime in order to reduce the decorrelation effect induced by the snow and ice coverage. The three Stations, MSWB, MREP and MAPS are located near the summit caldera (Figure 1). After corrections of tectonic motions using records from AV09, which is deployed near the Dutch Harbor and free of volcanic deformation, the cGNSS data are used for validation of the InSAR deformation and magmatic source modeling.

3.4.2 InSAR deformation mapping

Since its first demonstration for volcanic deformation mapping at Mount Etna, Italy (Massonnet et al., 1995), InSAR has been proven to be an effective tool for volcano monitoring. However, it is challenging to apply conventional InSAR algorithms to Makushin due to the decorrelation effect introduced by thick ice and snow covers in the summit area (Lu et al., 2002). Taking advantage of the long-term SAR observations, we use the PSInSAR technique to extract the ground scatterers which are stable over time, and reconstruct the surface deformation history (Hooper et al., 2004; Hooper, 2008). For detailed description of the algorithm, readers should

refer to Chapter 1 and Hooper (2008) and Hooper et al. (2007). After the selection of the persistent scatterers (PS) in a stochastic scheme and the weeding of noisy points, the deformation time series is reconstructed using 3D phase unwrapping (Hooper et al., 2007). Atmospheric phase screen (APS) corrections are performed with PyAPS (Jolivet et al., 2011) using the ERA5 weather model. Deformation histories produced from InSAR are validated by comparison with the cGNSS measurements projected to the SAR line-of-sight (LOS) directions.

3.4.1 Deformation modeling

The deformation time series mapped from SAR and cGNSS are used to track the temporal evolution of the magmatic source using EnKF (Zhan and Gregg, 2018; Evensen, 2009; Gregg and Pettijohn, 2016, Evensen, 2003). Previous studies have shown that a spherical Mogi source is sufficient to model the deformation source at Makushin volcano (Lu et al., 2002, Xue et al., 2020). Thus, following the data assimilation framework developed by Zhan and Gregg (2018), we model the volcanic deformation using an ensemble of Mogi sources updated by EnKF.

Source modeling is applied to three different observation groups: 1) Time-series LOS displacements derived from Envisat are used to investigate the magmatic sources from 2004 to 2010. During the Envisat observation period, no near-field cGNSS observations are available. Since the deformation time series derived from different SAR datasets have different reference times and it is difficult to convert them into the same imaging geometry due to low PS density and limited SAR data from across tracks sharing the same observation periods, deformation time series derived from InSAR are modeled individually. 2) Time-series LOS deformation produced from Sentinel-1 and three-dimensional deformation at Sentinel-1 acquisition dates produced from cGNSS stations MSWB and MREP are assimilated to track the temporal evolution source from 2014 to 2021. 3) cGNSS observations downsampled to monthly average bins are also

utilized to produce the volume change history at finer temporal resolution from a fixed source inferred from the average source locations derived from 1) and 2). MREP is not utilized in source modeling considering its records are potentially saturated by a secondary deforming (Section 3.6.1). The inverted volume change histories are joined by assuming there is no deformation from 2010 to 2014. Considering the short intervals between those SAR datasets and no pronounced displacements shown during the gaps from available cGNSS observations (Section 3.5 and Xue et al., 2020), no prominent bias should be introduced to the estimated cumulative volume changes.

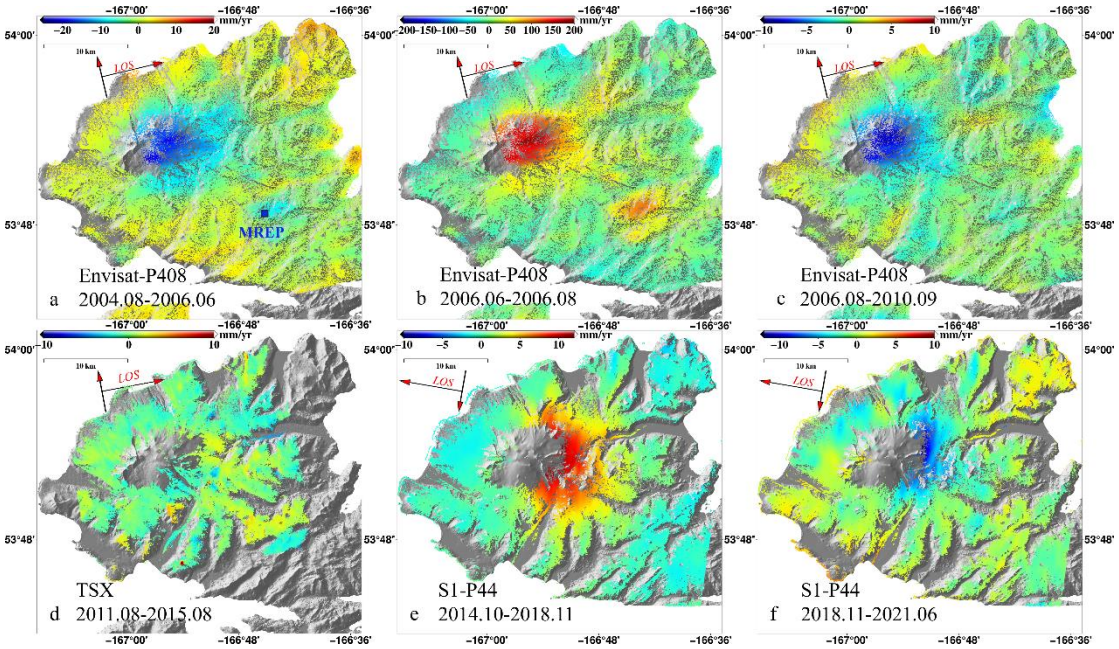

Figure 3.3. Average LOS deformation rates over each observation period. The dominant deformation patterns are intermittent episodes of deflations (a, c, f), quiescence (d), and inflations (b, e). Platform, track, and time spans (in year-month format) of each panel are labeled near the bottom left corners, respectively. The location of cGNSS station MREP is labeled as a blue square in panel a.

3.5 Results

Several volcano-wide deformation episodes with time-dependent rates have been identified at Makushin (Figure 3.3). From August 2004 to June 2006, the volcano was deflating at an average peak rate of about 2 cm/yr near the central caldera. Subsequently, a period of rapid inflation occurred from June to August 2006, producing cumulative uplifts with amplitude comparable to the subsidence generated in two years during the previous deflation episode. The transient episode of inflation came to an abrupt halt, transitioning into another deflation phase, with an average rate of approximately 1 cm/yr from August 2006 to August 2010. Since 2011, a period of quiescence commenced and lasted through 2015. No clear evidence of surface deformation associated with magmatic processes has been detected from the deformation time series during this period. Another inflation episode started in 2016 and lasted through 2018, with an average peak rate of ~2 cm/yr, which is much smaller than that during the 2006 rapid inflation episode. Since late 2018, there has been another persistent deflation episode, characterized by a subsiding rate of ~1 cm/yr. All the volcano-wide deformation recorded at Makushin, both inflations and deflations, are located near the east-northeast of the central caldera. This is concordant with the pre-eruptive inflation observed prior to the 1995 eruption and the post-eruptive deflation observed from 1996 to 2000 (Lu et al., 2002).

A secondary deforming region is also detected to the southeast of the volcano, located near the cGNSS station MREP. This deforming area has a much smaller spatial extent with temporal patterns consistent with the volcano-wide main deformation and has never been detected in other deformation surveys. The magnitude of this secondary deformation is much smaller than the main deformation across the caldera, with an average rate of about only half of the coeval main deformation, making it indistinct during 2014 to 2018 and 2018 to 2021. Deformation time series

derived from the TerraSAR-X and Sentinel-1 datasets are compared with the records from available cGNSS records from MREP, MSWB and MAPS stations (Figure S3.2) in the LOS direction. The InSAR measurements agree well with the cGNSS observations with all the standard deviations of their difference smaller than 10 mm.

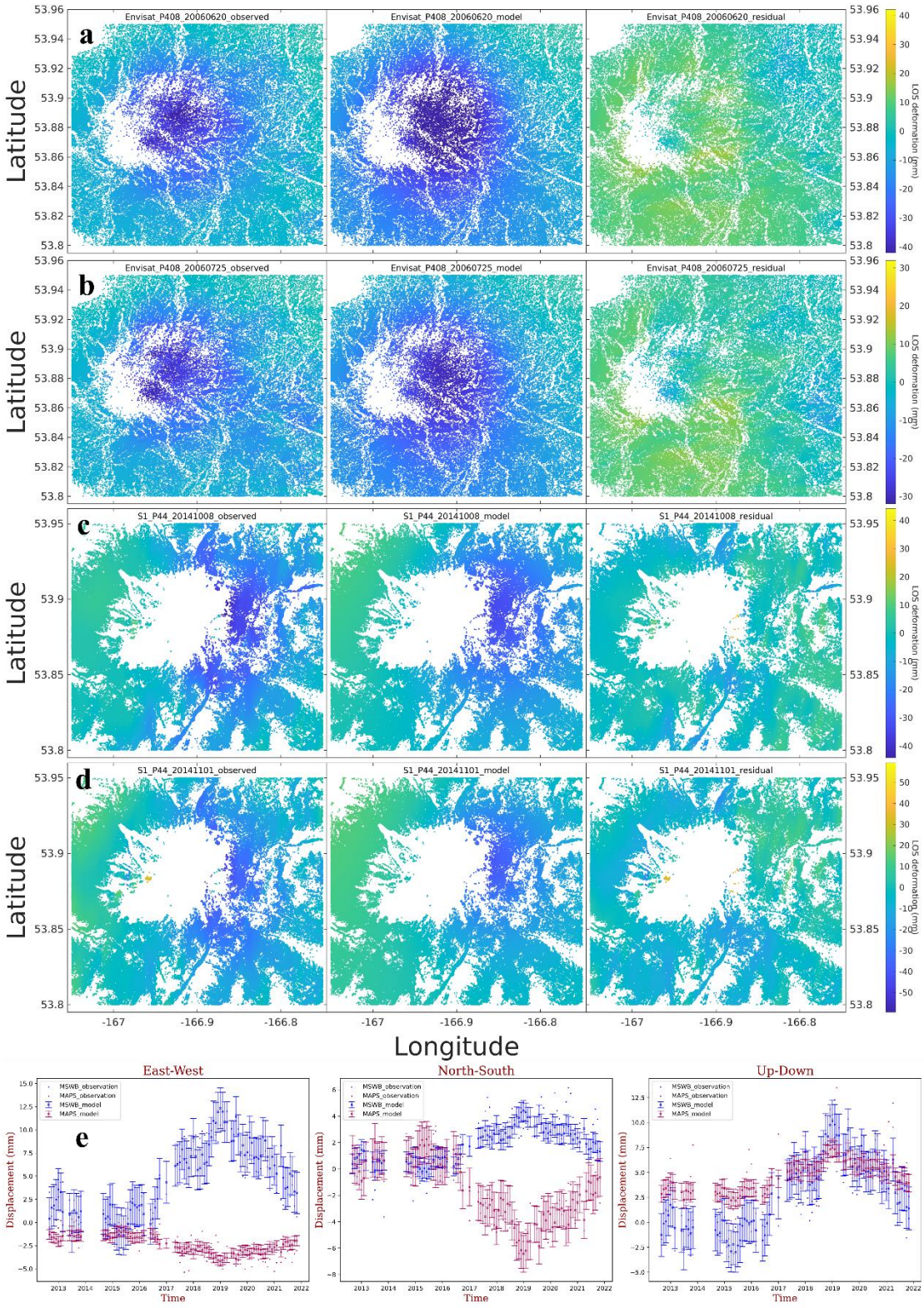

Figure 3.4. Example of observed (left), modeled (middle) LOS displacements and their residual (right) for Envisat (a and b) and Sentinel-1 (c and d) datasets. e) East-west (left), north-south

(middle), and up-down (right) GNSS observations and the model predicted displacements for MSWB (blue) and MAPS (red) stations.

Time series deformations across the volcano are used for modeling the magmatic source of the volcanic system using Mogi sources. The estimated source parameters including source locations and volume change are shown in Figure 3.5, where X and Y are the locations of the source in the east and north directions relative to the caldera summit, respectively. Our results show that the deformation sources for both the inflation and deflation episodes are highly consistent. Most of the sources are concentrated ~ 3 km to the east and ~ 1 km to the north of the summit caldera, located at depths ~6 km BSL. The persistent source locations throughout different periods of deformation suggest that all the deformation signals are likely produced from a stationary source, despite their distinct deformation rates. Cumulative volumetric change is about $-6 \times 10^6\ m^3$ from 2004 to 2021, indicating a deficit in the volume/pressure inside the magmatic reservoir. The long-term volume/pressure loss of the magmatic system suggests stronger depressurization processes dominant during our observation periods.

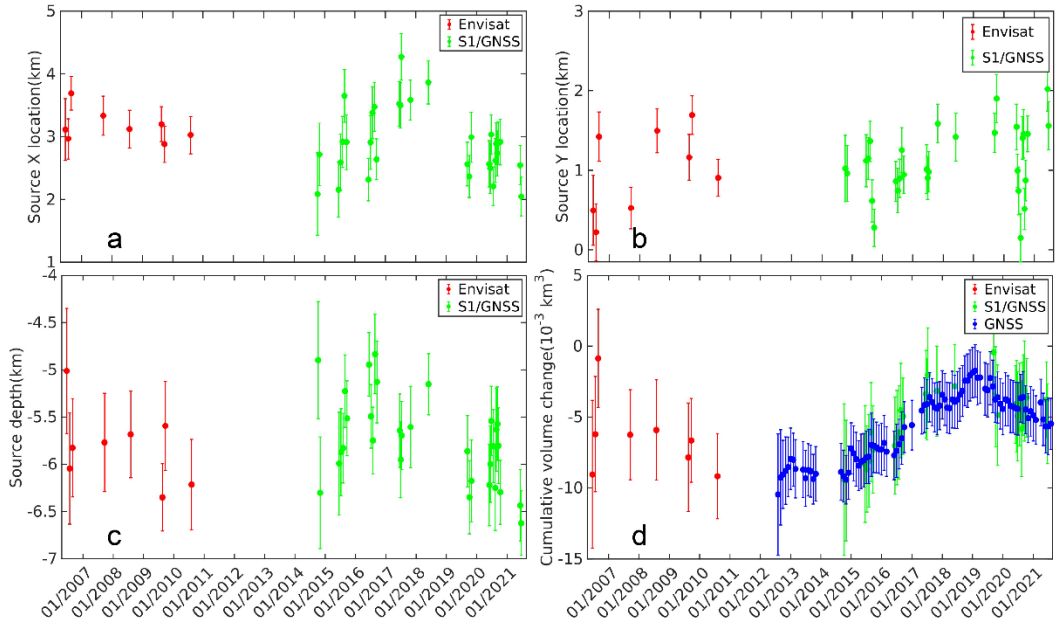

Figure 3.5. Inferred deformation source locations in a) east-west direction, b) north-south direction, and c) up-down direction. The east-west and north-south locations are relative to the peak of the volcano labeled as a black triangle in Figure 3.1. Depth is estimated relative to the sea level. d) cumulative volume change since August 2004. The average location inferred from Envisat and Sentinel-1/GNSS (MSWB and MAPS) is further used to track the volume change history since 2012 with cGNSS records (MSWB and MAPS).

3.6 Discussion

3.6.1 Magmatic source mechanism

Source parameters derived from the surface displacement histories suggest that the episodic inflation and deflation episodes with time-varying rates are produced from the same magmatic source. Moreover, the source locations during our observation period are highly consistent with the ones producing the pre-eruptive inflations and post-eruptive deflations from 1993 to 2000 (Lu et al., 2002), indicating that a stationary magmatic source is responsible for the deformations produced at Makushin since 1993. The derived source locations are also consistent with the area

of low Q_p (i.e., high seismic attenuation), low V_P and high V_P/V_S revealed from 3-D seismic tomography (Lanza et al., 2020; Syracuse et al., 2015), which usually indicate the presence of fluid. Anomalies of high seismic b-value were also identified above and around the source locations derived in our study (Bridges & Gao, 2006). The seismic b-value is a factor that describes the frequency of the earthquake size distribution, with a higher b-value usually associated with highly fractured rocks (Gutenberg & Richter, 1994). High seismic b-value, along with the concentration of relocated seismicity surrounding the derived sources (Lanza et al., 2020), may be an indicator that outlines the rigid rock walls of the regime of ductile magmas.

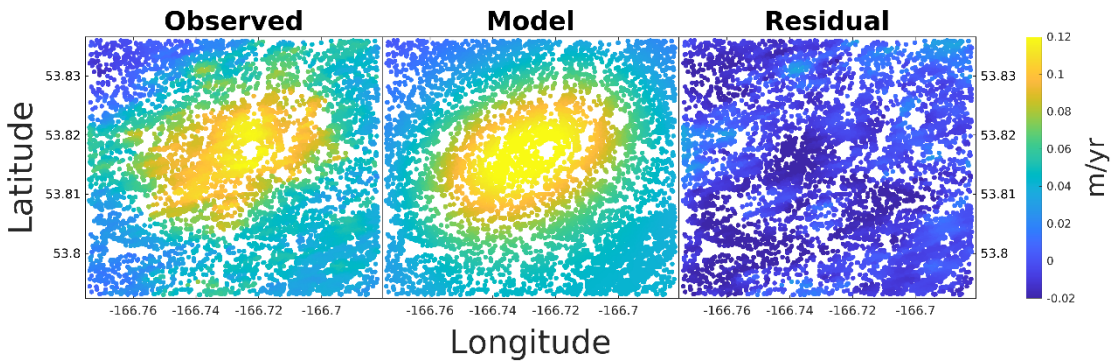

Figure 3.6. Observed (left), modeled (middle) LOS displacements, and their residual (right) of the secondary deformation during the rapid inflation (Figure 3.3b).

Inflation patterns identified from Makushin are diverse. The periods of inflation between 2016-2018, 1993-1995 (Lu et al., 2002), and 2000-2003 (Xue and Freymueller, 2020) each spanned several years, with average inflation rates ranging approximately from 20 to 40 mm/yr.The inflationary episode during the summer of 2006 is short-lived, characterized by a high average inflation rate reaching ~200 mm/yr. Volcano-wide inflation is generally associated with volume/pressure accumulations in the magmatic reservoir, with either magma or

exsolved volatiles ascending from a deeper magma source. The inflation episodes during our observation period are seamlessly followed by deflation episodes with various patterns. The accumulated volume/pressure during the 2006 inflations is almost dissipated by a rapid volume loss process within one year. The subsequent deflations until 2010 have smaller rates comparable to the one during 2018 and 2021. Long-term deflations without eruptions at volcanoes are usually interpreted as consequences of degassing, crystallization, or thermal contraction of the magma body (Watson et al., 2000; Lu and Dzurisin, 2014; Caricchi et al., 2014). Subsidence produced by thermal contractions of magma body and crystallization usually decay exponentially and have relatively steady rates in a short period of a few years after the emplacements (Wang and Aoki, 2019; Wittmann et al., 2017; Caricchi et al., 2014). The time-varying rates in a short period suggest that degassing may play an important role in the deflation episodes. Rapid volume loss immediately following the 2006 rapid inflation may be indicative of the dominant volatile phase during the pressurization/depressurization process. Makushin has well-known hydrothermal fields consisting of fumaroles, gas vents and bubble pools located on the south flank of the volcano, producing substantial gas emissions and steaming (Motyka et al., 1993; Werner et al., 2020). Seismic tomography data reveals areas of possible densely fractured rocks that may incubate vapor-filled cracks and fissures connecting the magma reservoir with the hydrothermal fields (Lanza et al., 2020; Syracuse et al., 2015). Those structures may serve as the gas migration pathways from the magma reservoir to the hydrothermal system.

Volatiles pressurizing the magmatic reservoir during inflation episodes may be the source of the gas emissions from the hydrothermal fields. Sulfur dioxide (SO_2) emission observations from various space-based spectrometers also agree with the volatile-dominated inflation-deflation hypothesis. Higher SO_2 emissions are noticed during the inflation periods, i.e., 2006 and 2016-

2018, compared with that during the deflation and quiescent periods (Figure 7a, Fioletov et al., 2023), suggesting significant degassing going on at Makushin all the time as well as more rapid degassing and volatile exsolution from deep magmatic source to the shallow chamber during the inflation periods. The high emission rate in 2008 is likely produced by another rapid inflation episode associated with high gas emission that is not revealed in the deformation time series as a result of the coarse temporal resolution of the Envisat data.

Although the volatile-dominated deflations are favored by the time-varying subsidence rates, we still cannot rule out the possibility of cooling- and crystallization-dominated deflations since we do not know whether these time-varying deflation rates are the net effects of near-steady contractions by cooling/crystallization and volume accumulations at time-dependent rates. In that scenario, consider a minimum constant cooling/crystallization contraction rate of $\sim 5 \times 10^{-3} km^3/yr$ (volume loss rate from 2006 to 2007), a time-dependent volume increase with a minimum average rate of $\sim 4.6 \times 10^{-3}\ km^3/yr$ is required to compensate for the cumulative volume change from 2004 to 2021, which is close to that of Okmok ($\sim 5.8 \times 10^{-3}\ km^3/yr$) and Westdahl ($\sim 5.9 \times 10^{-3}\ km^3/yr$). A peak rate of $\sim 4.6 \times 10^{-2}\ km^3/yr$ is required to produce the rapid inflation in mid-2006, which is substantially larger than that of Makushin's active neighbors (less than $\sim 2.5 \times 10^{-2}\ km^3/yr$), (Xue et al., 2020, Wang et al., 2021). Considering the less active volcanic activities at Makushin, the likelihood of such a high magmatic influx is low.

A secondary deforming area is identified near cGNSS station MREP, with synchronous displacements as the volcano-wide main deformation but with smaller rates and spatial extent. We analyze the average deformation rates and find a best-fit sill source located about 2-3 km BSL striking to the NE-SW direction. The location of the source producing the secondary

deformation is highly consistent with the shallow region with low V_p, V_p/V_s, and Q_p revealed in Lanza et al. (2020) and Syracuse et al. (2015), which likely implies the location of a fluid and gas-rich secondary reservoir. The synchronization between the main and secondary deformation suggests that the secondary reservoir is connected to the main magmatic reservoir, probably through dike or conduit systems (Figure 3.7b). When the magma/volatile accumulates in the main reservoir, the secondary reservoir will also be intruded to reach pressure balance. When volatiles extrude from the hydrothermal fields, both reservoirs get discharged. However, no significant displacements are detected in the vicinity of the secondary reservoir during the periods of 2014-2018 and 2018-2021, which may be attributed to small deformation rates or possible closure of the connection between the main and secondary reservoir. The presence of secondary deformation poses significant challenges to source modeling of the main deformation using exclusively cGNSS data, considering the limited number of available cGNSS stations established in the vicinity of Makushin volcano and measurements from MREP may be greatly impacted by the secondary deformation. Furthermore, this circumstance emphasizes the critical need to expand the network of cGNSS stations deployed at Makushin to effectively monitor volcanic activities.

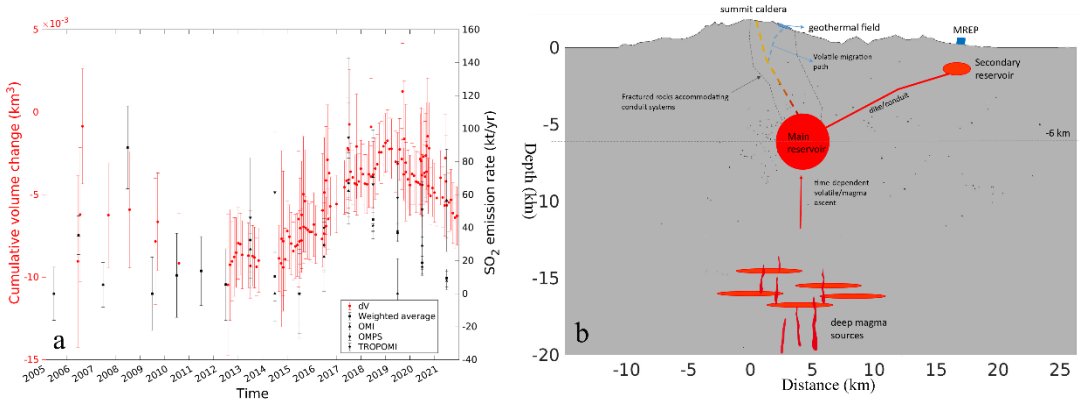

Figure 3.7. Cumulative volume change (red) vs annual SO_2 emission rates (black) derived from different datasets. (Weighted average: weighted average of 3 measurements; OMI: Ozone Monitoring Instrument; OMPS: Ozone Mapping and Profiler Suite; TROPOMI: TROPOspheric Monitoring Instrument; see Fioletov et al. (2023) for more details). b). A conceptual model for the Makushin plumbing system (values are not to scale).

3.6.2 The 2020 seismic anomaly

In June 2020, a large earthquake swarm occurred at Makushin, with two main shocks > M4 and a few long-period events located ~15 km west of Dutch Harbor (Figure S3.3). This seismic swarm was by far the most substantial surge in seismic activity recorded at Makushin since 1996, raising concerns about an impending eruption (Lanza et al., 2022). Earthquakes typically result from brittle failure of the rocks, which frequently serve as a precursor of volcanic activities, e.g., fluid movements and dike intrusions. Some eruptions are preceded by intense short-term seismicity, making it a signal that is usually used for the prediction of impending eruptions (Pesicek et al., 2018, Chouet, 1996; Dzurisin, 2003; Rubin and Gillard, 1998). In the case of magma movement-induced earthquakes, surface deformation is usually found as a response to the evolving volume/pressure changes within the magmatic plumbing system (Jakobsdóttir et al., 2008; Cannavo' et al., 2019). We examined the averaged LOS deformation rates (Figure S3)

throughout the period of the seismic anomaly from early June to mid-October in 2020, which is more resistant to temporally uncorrelated artifacts than individual interferograms (Kwoun et al., 2006). No sign of surface displacements was detected near the epicenters of the seismic anomaly during this period.

Lanza et al. (2022) interpreted the 2020 seismic anomaly as a result of stress perturbation over pre-existing weak zones during small rapid magma intrusion. The absence of surface deformation associated with the hypothesized magma intrusion may be a result of limited intrusion volume, or the intrusion may be too deep to produce notable surface deformations. 3-D seismic tomography analyses show that the hypocenters of the seismic swarm in mid-2020 are located near a region characterized by a transition from higher V_P/V_S, lower V_P and Q_P, to lower V_P/V_S, higher V_P and Q_P (Lanza et al., 2020), which may represent the boundary between the weaker, hotter, and fracture-evolved magma reservoir and the colder, rigid host crust. Dike intrusion may be driven by fluid fracturing at the magmatic chamber base, promoted by the volatile-dominated magma plumbing system, as inferred from surface deformation patterns. In that case, the seismicity rate during dike propagation frequently lacks a clear and monotonic hypocenter migration following dike propagation for basaltic volcanoes (Rubin, 1993b, 1993a; Me´riaux and Jaupart, 1998; Roper and Lister, 2005) which may explain the lack of spatial-temporal evolution of the earthquakes during the intrusion (Lanza et al., 2022). The rapid volume accumulation required to generate the large magnitude (M3+) earthquakes (Lanza et al., 2022) may be a result of another rapid volatile intrusion as the one during 2006, with a magnitude too small to produce surface deformation discernible with InSAR.

3.6.3 Evidence of surface erosion

Persistent lengthening in LOS directions (hereafter referred as deflation) are detected from the valleys to the west and east of the volcano from two ALOS-2 SAR tracks (outlined by the red polygons 1 and 2 in Figure 3.8 a and b). Although more similar deformation patterns can be found from other valleys, only the ones outlined by polygons 1 and 2 are the strongest and can be identified easily from both ALOS-2 tracks. For simplicity, we focus on these two deflation areas in the subsequent discussion. The deflation strengthens gradually from the origin of the valleys off the summit to the end near the coast, with maximum rates ~10-20 mm/yr in the flat plains near the estuary. The small spatial extent indicates that the deflations are likely produced by near surface sources.

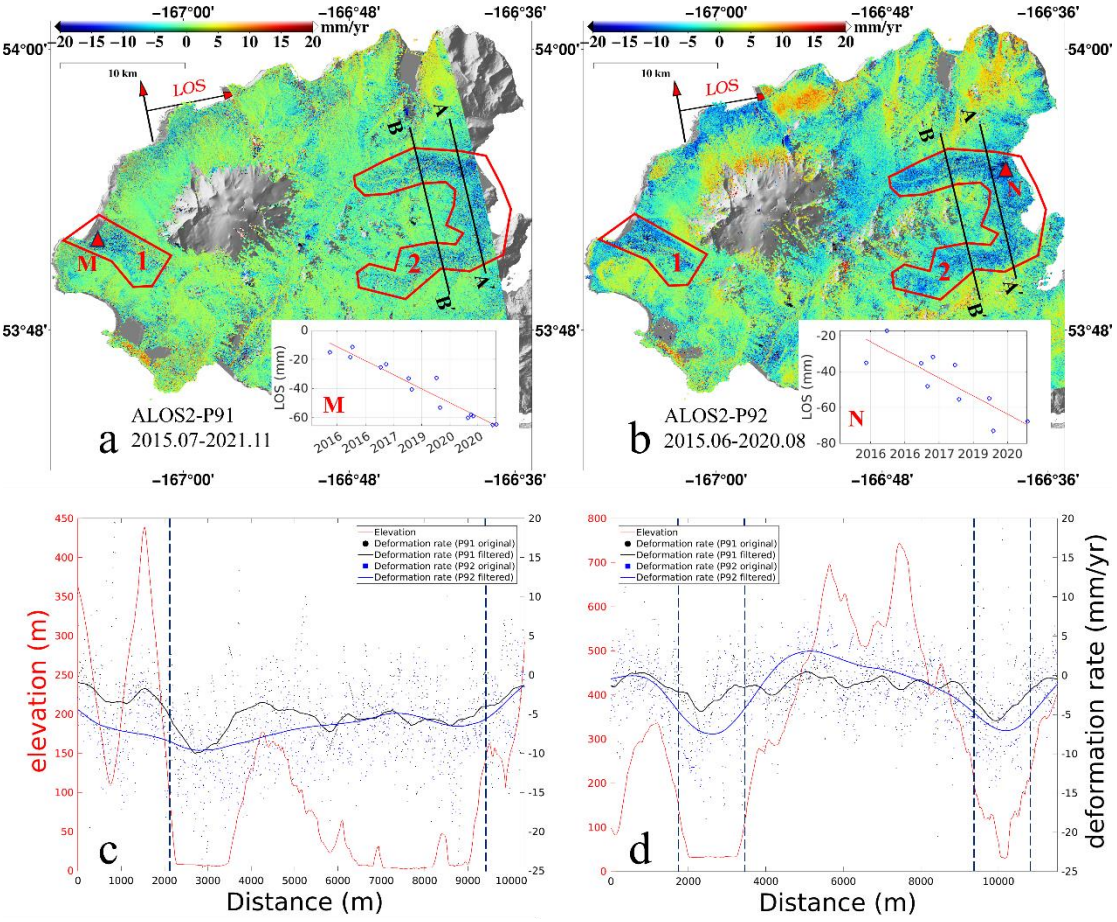

Figure 3.8. a, b). Average LOS deformation rates derived from ALOS-2 P91 track and P92 track, respectively. Platform, track, and time spans (in year-month format) of each panel are labeled near the bottom left corners, respectively. c, d) Cross section of LOS deformation rates along profile AA' and BB' shown in a) and b), respectively. The deflations are outlined by the red polygons to the west and east of the volcano. Inset in a and b are the LOS deformation history at locations denoted by red triangles (M, N) in polygon 1 (a) and 2 (b), respectively. The dark blue dashed lines in c and d outline the location of the plains and valleys along the profiles.

A wide variety of processes can produce similar persistent deflations, e.g., landslides, contraction of the lava flow, and erosion of the sediment underneath vegetation. Landslides in volcanoes can be induced by earthquakes, eruptions, and other volcanic activities, which is especially common on the steep volcano flanks and inside the caldera craters (Tsuchiya et al.,

2009; Schöpa et al., 2017). Additionally, landslides have been previously observed at Makushin (Allan et al., 2018; Beget et al., 2000). While landslides may be responsible for part of the subsidence observed along the steep flanks, they cannot account for the wide deflations in the flat plains near the coast. Surficial deflations are usually seen at the emplaced lava flows and pyroclastic deposits, produced from thermal contraction and volatile exsolution (Lu et al., 2005; Stevens et al., 2001). The absence of eruptions larger than VEI 3 at Makushin for nearly two centuries suggests that the likelihood of a thick, hot lava flow reaching to valley away from the volcano is minimal. Geological maps of Makushin also show that the surface of the valley is covered mainly by alluvium deposits (Miller et al., 1998, McConnell et al., 1998), which produce relatively lower SAR intensity and InSAR coherence than typical lava flows within the valleys (Lu and Dzurisin, 2014).

The most preferred explanation for the large area of deflation is the erosion of the vegetated alluvium deposits in the valleys. Locations of the deflations are highly consistent with the distribution of the loose alluvium deposits along the valleys and near the flat plains (Figure 8c and 8d). The deflation reaches peak rates at the valley base where the erosion is strongest and diminishes as it extends towards the valley edges. The erosions in the deflating areas are most likely results of hydro-meteorological corrosion of the pyroclastic debris, with water playing a critical role. Acidic hydrothermal fluid discharged from the geothermal field and the seasonal freeze and thawing cycle in the low elevations weaken the sediments. The dense precipitation provides massive meteorological water (Wendler et al., 2017), along with the water from the melting of the dense snow and ice capes in the flank and summit area, wash away the loose alluvium deposits beneath vegetation and transport them through the streams and rivers incubated in the valleys. Erosion of the sediments results in rapid-changing surface dielectric

properties, along with the dense seasonal vegetations, explain in part why only the L-band ALOS-2 datasets maintain coherence in this region, considering L-band signal has larger penetration depth and thus is more resistant to changes in the surface (Wei and Sandwell, 2009). The large-scale LOS lengthening with rates comparable to volcanic deformation poses extra challenges to source modeling with L-band SAR data. It is necessary to mask out the valleys before source inversions to avoid introducing significant bias.

3.7 Conclusion

By applying the PSInSAR technique using datasets taken from across platforms, we map the displacement history at Makushin volcano, Alaska, from 2004 to 2021. Several long-term volcano-wide deflation episodes, along with one rapid and one long-term inflation located to the northeast of the summit caldera are identified. We model the derived deformation time series with Mogi models and derive the source parameters including locations and source strengths using EnKF. The inferred source locations suggest a stationary magmatic source located ~6 km BSL, which is consistent with the sources that produced the displacements from 1993 to 2000. The rapid inflation in the summer of 2006 is suggested to be a result of the accumulation of volatile-dominated extrusions from deep magma sources and the time-varying deflations are probably produced by degassing from the magma reservoir that is responsible for the volcano-wide deflations. A shallow secondary reservoir connected to the main magmatic chamber, which was not identified in previous GNSS surveys, is revealed to the southeast of the volcano. The discovery of the secondary reservoir underscores the importance of InSAR data for the monitoring of volcanoes with complex magma plumbing systems. Cumulative volume changes

in the magma reservoir and proposed volatile-dominated surface deformation indicate that Makushin was undergoing volume-deficient processes from 2004 to 2021.

3.8 Acknowledgements

This research is funded by NASA Earth Surface & Interior Program (80NSSC19K0357), NASA NISAR Science Team (80NSSC22K1888), and the Shuler-Foscue Endowment at the Southern Methodist University. ALOS-2 PALSAR-2 datasets are copyrighted and provided by Japan Aerospace Exploration Agency's via the 3rd Research Announcement on the Earth Observations (PI No. ER3A2N132).

3.9 References

Bagnardi, M., Hooper, A., 2018. Inversion of Surface Deformation Data for Rapid estimates of Source Parameters and Uncertainties: a Bayesian Approach. Am. Geophys. Union (AGU). https://doi.org/10.1029/2018gc007585.

Beget, J.E., Nye, C.J., Bean, K.W., 2000. Preliminary Volcano-Hazard Assessment for Makushin Volcano. Alaska. Rep, Invest, p. 4. Bridges, D.L., Gao, S.S., 2006. Spatial variation of seismic b-values beneath Makushin Volcano, Unalaska Island, Alaska. Earth Planet. Sci. Lett. 245 (1), 408–415. https://doi.org/10.1016/j.epsl.2006.03.010.

Cannavo', F., Sciotto, M., Cannata, A., Di Grazia, G., 2019. An integrated geophysical approach to track magma intrusion: the 2018 Christmas Eve eruption at Mount Etna. Geophys. Res. Lett. 46 (14), 8009–8017.

Caricchi, L., Biggs, J., Annen, C., Ebmeier, S., 2014. The influence of cooling, crystallisation and re-melting on the interpretation of geodetic signals in volcanic systems. Earth Planet. Sci. Lett. 388, 166–174. https://doi.org/10.1016/j.epsl.2013.12.002.

Chouet, B.A., 1996. Long-period volcano seismicity: its source and use in eruption forecasting. Nature (London) 380 (6572), 309–316. https://doi.org/10.1038/380309a0.

Dean, K., Servilla, M., Roach, A., Foster, B., Engle, K., 1998. Satellite monitoring of remote volcanoes improves study efforts in Alaska. EOS Trans. Am. Geophys. Union 79 (35), 413–423.

Drewes, H., Fraser, G.D., Snyder, G.L., Barnett Jr., H.F., 1961. Geology of Unalaska Island and adjacent insular shelf, Aleutian Islands, Alaska: in Investigations of Alaskan volcanoes, 1028-S. U.S. Geological Survey Bulletin, pp. 583–676. https://doi.org/10.3133/b1028S.

Dzurisin, D., 2003. A comprehensive approach to monitoring volcano deformation as a window on the eruption cycle. Rev. Geophys. 41 (1) https://doi.org/10.1029/2001RG000107.

Evensen, G., 2003. The ensemble Kalman filter: Theoretical formulation and practical implementation. Ocean Dyn. 53, 343–367. https://doi.org/10.1007/s10236-003-0036-9.

Evensen, G., 2009. The ensemble Kalman filter for combined state and parameter estimation. IEEE Control. Syst. Mag. 29 (3), 83–104. https://doi.org/10.1109/MCS.2009.932223.

Fioletov, V.E., McLinden, C.A., Griffin, D., Abboud, I., Krotkov, N., Leonard, P.J., Li, C., Joiner, J., Theys, N., Carn, S., 2023. Version 2 of the global catalogue of large anthropogenic and volcanic SO 2 sources and emissions derived from satellite measurements. Earth System Science Data 15 (1), 75–93.

Freymueller, Jeffrey T., Grapenthin, Ronni, Paskievitch, John, 2011. Alaska Volcano Observatory GPS Network Makushin - MSWB-MSWB P.S., the GAGE Facility Operated by EarthScope Consortium, GPS/GNSS Observations Dataset. https://doi.org/10.7283/T5668BJ3.

Freymueller, Jeffrey T., Grapenthin, Ronni, Paskievitch, John, 2012a. Alaska Volcano Observatory GPS Network - MREP-Makushin Repeater P.S., the GAGE Facility Operated by EarthScope Consortium, GPS/GNSS Observations Dataset. https://doi.org/10.7283/T5P8492X.

Freymueller, Jeffrey T., Grapenthin, Ronni, Paskievitch, John, 2012b. Alaska Volcano Observatory GPS Network - MAPS-Makushin Pakushin SE P.S., the GAGE Facility Operated by EarthScope Consortium, GPS/GNSS Observations Dataset. https://doi.org/10.7283/T5T151S7.

Gregg, P.M., Pettijohn, J.C., 2016. A multi-data stream assimilation framework for the assessment of volcanic unrest. J. Volcanol. Geotherm. Res. 309, 63–77. https://doi.org/10.1016/j.jvolgeores.2015.11.008.

Gutenberg, B., Richter, C.F., 1944. Frequency of earthquakes in California. Bull. Seismol. Soc. Am. 34 (4), 185–188.

Hooper, A., 2008. A multi-temporal InSAR method incorporating both persistent scatterer and small baseline approaches. Geophys. Res. Lett. 35 (16) https://doi.org/10.1029/2008GL034654.

Hooper, A., Zebker, H.A., 2007. Phase unwrapping in three dimensions with application to InSAR time series. J. Opt. Soc. Am. A Opt. Image Sci. Vis. 24 (9), 2737–2747. https://doi.org/10.1364/JOSAA.24.002737.

Hooper, A., Zebker, H., Segall, P., Kampes, B., 2004. A new method for measuring deformation on volcanoes and other natural terrains using InSAR persistent scatterers. Geophys. Res. Lett. 31 (23), L23611-n/a. https://doi.org/10.1029/2004GL021737.

Jakobsd´ottir, S.S., Roberts, M.J., Guđmundsson, G.B., Geirsson, H., Slunga, R., 2008. Earthquake swarms at Upptyppingar, north-East Iceland: a sign of magma intrusion? Stud. Geophys. Geod. 52, 513–528.

Jolivet, R., Grandin, R., Lasserre, C., Doin, M.-., Peltzer, G., 2011. Systematic InSAR tropospheric phase delay corrections from global meteorological reanalysis data. Geophys. Res. Lett. 38 (17), L17311–n/a. https://doi.org/10.1029/2011GL048757.

Kwoun, O., Lu, Z., Neal, C., Wicks, C., 2006. Quiescent deformation of the Aniakchak Caldera, Alaska, mapped by InSAR. Geology 34 (1), 5–8.

Lanza, F., Thurber, C.H., Syracuse, E.M., Power, J.A., Ghosh, A., 2020. Seismic tomography of compressional wave velocity and attenuation structure for Makushin Volcano, Alaska. J. Volcanol. Geotherm. Res. 393 (C), 106804 https://doi.org/10.1016/j.jvolgeores.2020.106804.

Lanza, F., Roman, D.C., Power, J.A., Thurber, C.H., Hudson, T., 2022. Complex magmatic-tectonic interactions during the 2020 Makushin Volcano, Alaska, earthquake swarm. Earth Planet. Sci. Lett. 587 https://doi.org/10.1016/j.epsl.2022.117538.

Lerner, A.H., Crowley, P.D., Nicolaysen, K.P., Hazlett, R.W., 2018. Stratigraphy, distribution, and evidence for mafic triggering of the ca. 8.5 ka Driftwood Pumice eruption, Makushin Volcano, Alaska, U.S.A. J. Volcanol. Geotherm. Res. 357, 362–377. https://doi.org/10.1016/j.jvolgeores.2018.05.006.

Lu, Z., Dzurisin, D., 2014. InSAR imaging of Aleutian volcanoes. In: InSAR Imaging of Aleutian Volcanoes. Springer, pp. 87–345.

Lu, Z., Power, J.A., McConnell, V.S., Wicks Jr., C., Dzurisin, D., 2002. Preeruptive inflation and surface interferometric coherence characteristics revealed by satellite radar interferometry at Makushin Volcano, Alaska: 1993–2000. Journal of Geophysical Research - Solid. Earth 107 (B11), ECV 1-1-1. https://doi.org/10.1029/2001JB000970.

Lu, Z., Masterlark, T., Dzurisin, D., 2005. Interferometric synthetic aperture radar study of Okmok volcano, Alaska, 1992-2003: Magma supply dynamics and postemplacement lava flow deformation. J. Geophys. Res. Solid Earth 110 (B2). https://doi.org/10.1029/2004JB003148.

Massonnet, D., Briole, P., Arnaud, A., 1995. Deflation of Mount Etna monitored by spaceborne radar interferometry. Nature 375 (6532), 567–570.

McConnell, V.S., Beg´et, J.E., Roach, A.L., Bean, K.W., Nye, C.J., 1998. Geologic map of the Makushin Volcanic Field, Unalaska Island. Alaska. Alaska Div Geol Geophys Surv. Report of Investigations 97–20, unpaged, 2 sheets, scale 1:63,500.

M´eriaux, C., Jaupart, C., 1998. Dike propagation through an elastic plate. J. Geophys. Res. Solid Earth 103 (B8), 18295–18314. https://doi.org/10.1029/98JB00905.

Miller, T.P., McGimsey, R.G., Richter, D.H., Riehle, J.R., Nye, C.J., Yount, M.E., Dumoulin, J.A., 1998. Catalog of the Historically Active Volcanoes of Alaska. United States Department of the Interior, United States Geological Survey.

Mogi, K., 1958. Relations between the eruptions of various volcanoes and the deformations of the ground surfaces around them. Earthq Res Inst 36, 99–134.

Motyka, R.J., Liss, S.A., Nye, C.J., Moorman, M.A., 1993. Geothermal resources of the Aleutian arc. Professional Report PR 0114. Alaska Division of Geological & Geophysical Surveys.

Pesicek, J.D., Wellik, J.J., Prejean, S.G., Ogburn, S.E., 2018. Prevalence of Seismic Rate Anomalies Preceding Volcanic Eruptions in Alaska. Front. Earth Sci. 6 https://doi.org/10.3389/feart.2018.00100.

Power J. A. and others (2020). Goals and Development of the Alaska Volcano Observatory Seismic Network and Application to forecasting and Detecting Volcanic Eruptions. Seismol. Res. Lett., 91 (2A), 647–659, https://doi.org/10.1785/0220190216.

Power, J.A., Friberg, P.A., Haney, M.M., Parker, T., Stihler, S.D., Dixon, J.P., 2019. A unified catalog of earthquake hypocenters and magnitudes at volcanoes in Alaska—1989 to 2018: U.S. Geological Survey Scientific Investigations Report 2019–5037, 17 p. https://doi.org/10.3133/sir20195037.

Roper, S.M., Lister, J.R., 2005. Buoyancy-driven crack propagation from an overpressured source. J. Fluid Mech. 536, 79–98.

Rubin, A.M., 1993a. Dikes vs. diapirs in viscoelastic rock. Earth Planet. Sci. Lett. 119 (4), 641–659. https://doi.org/10.1016/0012-821X(93)90069-L.

Rubin, A.M., 1993b. Tensile fracture of rock at high confining pressure: Implications for dike propagation. J. Geophys. Res. 98 (B9), 15919–15935. https://doi.org/10.1029/93JB01391.

Rubin, A.M., Gillard, D., 1998. Dike-induced earthquakes: Theoretical considerations. J. Geophys. Res. Solid Earth 103 (B5), 10017–10030.

Sch¨opa, A., Chao, W., Lipovsky, B.P., Hovius, N., White, R.S., Green, R.G., Turowski, J. M., 2018. Dynamics of the Askja caldera July 2014 landslide, Iceland, from seismic signal analysis: precursor, motion, and aftermath. Earth Surf. Dyn. 6 (2), 467–485. https://doi.org/10.5194/esurf-6-467-2018.

Stevens, N.F., Wadge, G., Williams, C.A., Morley, J.G., Muller, J., Murray, J.B., Upton, M., 2001. Surface movements of emplaced lava flows measured by synthetic aperture radar interferometry. J. Geophys. Res. 106 (B6), 11293–11313. https://doi.org/10.1029/2000JB900425.

Sudhaus, H., Sigurj´on, J., 2009. Improved source modelling through combined use of InSAR and GPS under consideration of correlated data errors: application to the June 2000 Kleifarvatn earthquake, Iceland. Geophys. J. Int. 176 (2), 389–404.

Syracuse, E.M., Maceira, M., Zhang, H., Thurber, C.H., 2015. Seismicity and structure of Akutan and Makushin Volcanoes, Alaska, using joint body and surface wave tomography. J. Geophys. Res. Solid Earth 120 (2), 1036–1052. https://doi.org/10.1002/2014JB011616.

Tsuchiya, S., Sasahara, K., Shuin, S., Ozono, S., 2009. The large-scale landslide on the flank of caldera in South Sulawesi, Indonesia. Landslides 6 (1), 83–88. https://doi.org/10.1007/s10346-009-0143-x.

UNAVCO Community, 2004. PBO GPS Network – AV09-Haystack__AK2004 P.S., the GAGE Facility operated by EarthScope Consortium. GPS/GNSS Observations Dataset. https://doi.org/10.7283/T5GQ6VP0.

Wang, X., Aoki, Y., 2019. Posteruptive thermoelastic deflation of intruded magma in Usu volcano, Japan, 1992–2017. J. Geophys. Res. Solid Earth 124 (1), 335–357.

Wang, J., Lu, Z., Gregg, P.M., 2021. Inflation of Okmok Volcano during 2008–2020 from PS analyses and Source Inversion with Finite Element Models. Journal of Geophysical research. Solid. Earth 126 (10), n/a. https://doi.org/10.1029/2021JB022420.

Watson, I.M., Oppenheimer, C., Voight, B., Francis, P.W., Clarke, A., Stix, J., Miller, A., Pyle, D.M., Burton, M.R., Young, S.R., 2000. The relationship between degassing and ground deformation at Soufriere Hills Volcano, Montserrat. J. Volcanol. Geotherm. Res. 98 (1–4), 117–126.

Wei, M., Sandwell, D.T., 2010. Decorrelation of L-Band and C-Band Interferometry over Vegetated areas in California. IEEE Trans. Geosci. Remote Sens. 48 (7), 2942–2952. https://doi.org/10.1109/TGRS.2010.2043442.

Wendler, G., Gordon, T., Stuefer, M., 2017. On the Precipitation and Precipitation Change in Alaska. Atmosphere 8 (12), 253. https://doi.org/10.3390/atmos8120253.

Werner, C., Kern, C., Kelly, P.K., 2020. Chemical evaluation of water and gases collected from hydrothermal systems located in the central Aleutian arc, August 2015. U.S. Geological Survey Scientific Investigations Report 2020–5043, 35 p. https://doi.org/10.3133/sir20205043.

Wittmann, W., Sigmundsson, F., Dumont, S., Lavall´ee, Y., 2017. Post-emplacement cooling and contraction of lava flows: InSAR observations and a thermal model for lava fields at Hekla volcano, Iceland. J. Geophys. Res. Solid Earth 122 (2), 946–965.

Wood, C.A., Juergen, Kienle, 1990. Volcanoes of North America: United States and Canada. Cambridge University Press, New York.

Xue, X., Freymueller, J.T., 2020. A 25-year history of Volcano Magma Supply in the East Central Aleutian Arc, Alaska. Geophys. Res. Lett. 47 (15), n/a. https://doi.org/10.1029/2020GL088388.

Zhan, Y., Gregg, P.M., 2017. Data assimilation strategies for volcano geodesy. J. Volcanol. Geotherm. Res. 344, 13–25. https://doi.org/10.1016/j.jvolgeores.2017.02.015.

3.10 Supplementary

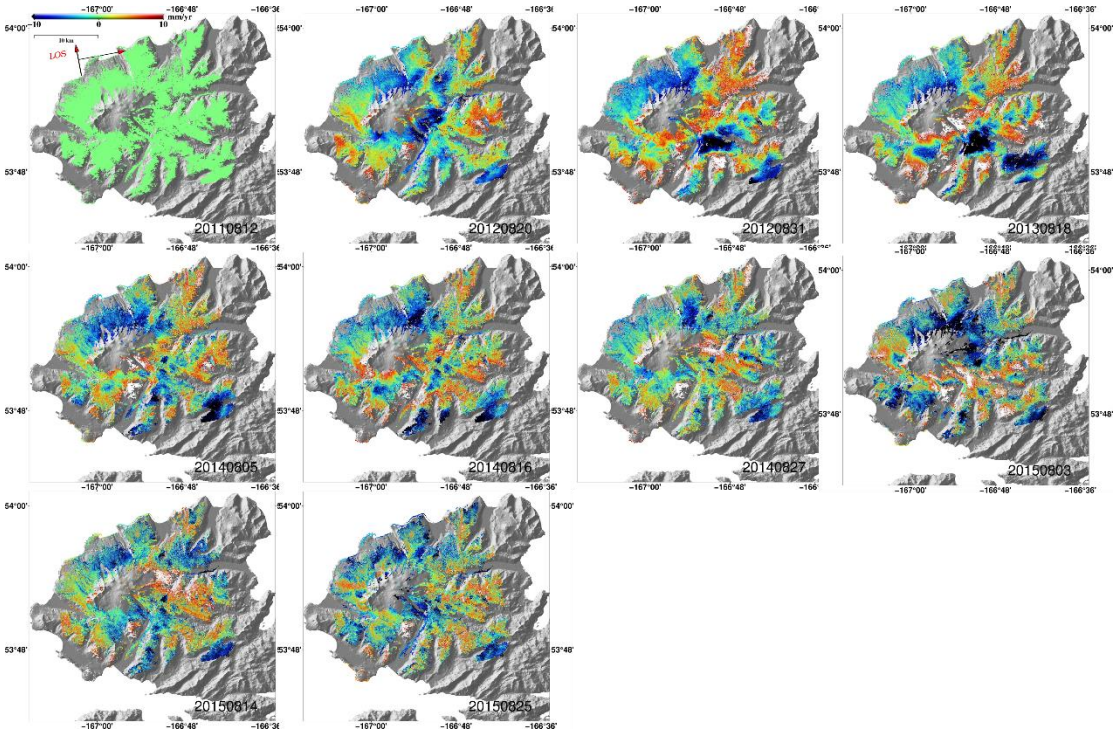

Figure S3.1. LOS deformation time series produced from TerraSAR-X data. No clear deformation can be identified from the dense atmospheric artifacts.

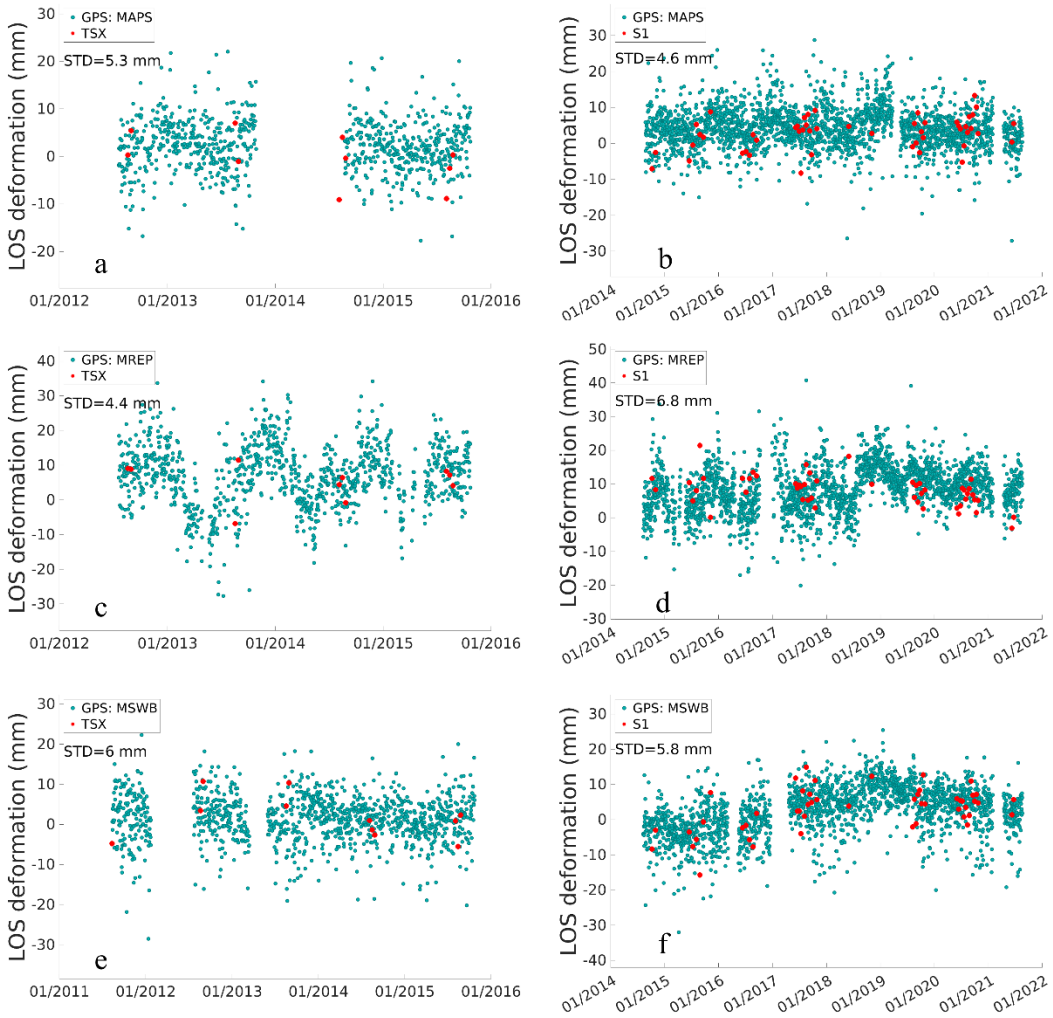

Figure S3.2. Comparison between InSAR and GNSS measurements in LOS direction for a), c), e). TerraSAR-X and b), d), f). Sentinel-1 data. GNSS records at each SAR acquisition are calculated as the average of the observations one week before and after the corresponding acquisition time. The InSAR-derived deformation agrees well with the GNSS records, with standard deviation of the measurement errors less than 7 mm at all stations.

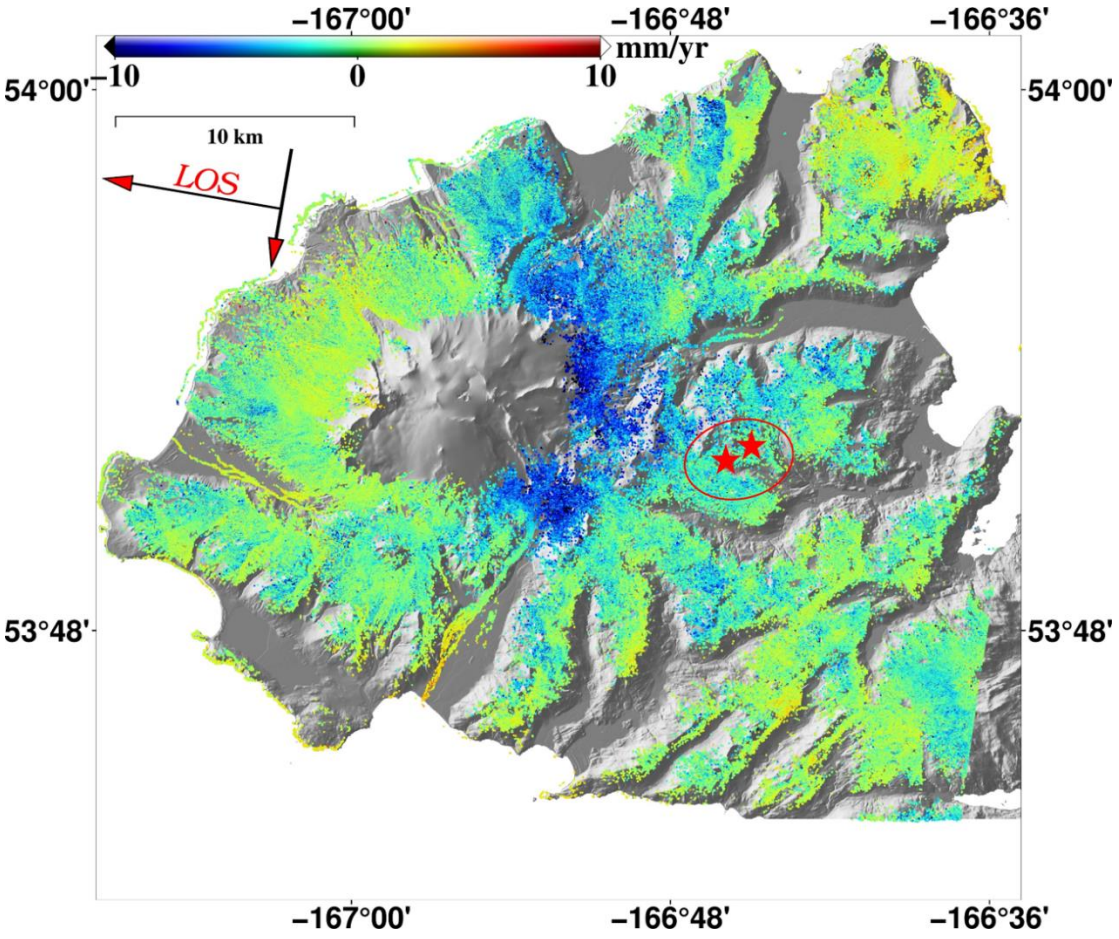

Figure S3.3. Average LOS deformation rate of Makushin during early June to mid-September in 2021 produced from Sentinel-1 data. The red stars represent the locations of the two large earthquakes with magnitudes larger than M4. The red ellipse delineates the locations of the earthquake swarm. No deformation associated with the seismic anomaly can be identified.

CHAPTER 4
ALONG-ARC VOLCANISM IN THE WESTERN AND CENTRAL ALEUTIAN FROM 2015 TO 2021 REVEALED BY CLOUD-BASED INSAR PROCESSING

4.1 Abstract

Leveraging a cloud-based interferometric synthetic aperture radar (InSAR) time-series processing framework, we map the surface deformation along the western and central Aleutian volcanoes from 2015 to 2021. The observed crustal deformation from more than 15 volcanoes is attributed to a wide range of magmatic or tectonic processes, e.g., magma accumulation in the magmatic reservoir, steady cooling or degassing of magma or hydrothermal systems, and faulting. More vigorous magmatism in the central Aleutian is noticed and appears to be related to higher magma production rates or higher magma ascent rates as a result of oblique subduction. New deformation patterns never observed in previous studies are detected and modeled at Tanaga, Great Sitkin and Yunaska. This study showcases the cloud-processing capability to generate interferograms at scale and processing tools to analyze these time series over large, tectonically active areas.

4.2 Introduction

The western and central Aleutian volcanic arc, accommodating more than 20 active volcanoes (Figure 4.1), is one of the most volcanically and seismically active areas in the world. Volcanic deformation with diverse patterns has been identified at multiple sites in the western and central Aleutian since the 1990s, reflecting complex magmatic processes occurring in the volcanic system. Okmok and Seguam are periodically inflating and subsiding in response to

magma intrusion and withdrawal (Lu et al., 2010; Lee et al., 2013). Persistent surficial subsidence has been detected at Kanaga and Amukta as a result of the cooling of erupted deposits (Lu and Dzurisin, 2014). Persistent subsidence with deeper sources produced by magma or hydrothermal cooling or degassing is observed at Fisher and Aniakchak (Gong et al., 2014; Kwoun et al., 2006). Surface deformation can also be absent from InSAR observations prior to eruptions at open-conduit volcanoes like Cleveland and Shishaldin (Wang et al., 2015).

InSAR measures the two-dimensional deformation field at promising temporal and spatial resolution, providing comprehensive details on the deformation field from a broad view. Previous InSAR deformation studies on the Aleutian volcanoes are generally limited to single or multiple volcanoes due to the restriction of data quality, and computation and processing complexities (Lu and Dzurisin, 2010; Lu et al., 2003; Wang et al., 2015); an arc-wide deformation survey took several years (Lu and Dzurisin, 2014). Instead, our study aims at rapid mapping of the arc-wide volcanic deformation since 2015 by leveraging the cloud-based InSAR processing capabilities to evaluate the status of the volcanic activities in the western and central Aleutian. In partnership with JPL's Advanced Rapid Imaging and Analysis (ARIA) project and the Alaska Satellite Facility (ASF), we used the ARIA- Hybrid Pluggable Processing Pipeline (HYP3) InSAR processing framework to produce a dense time series with Sentinel-1 Synthetic Aperture Radar (SAR) acquisitions from 2015 to 2021.

Our ARIA-HyP3 framework uses state-of-the-art InSAR processing algorithms (i.e., InSAR Scientific Computing Environment 2, ISCE2; Rosen et al, 2012) to generate standardized sensor-neutral products (i.e., the ARIA-S1-GUNWs; Bekaert et al., 2019), that are then published to the ASF Distributed Active Archive Center (DAAC), where they are stored and are freely available for download. This significantly simplifies the processing workflow by reducing the redundant

exertion of interferogram generation on the user side. Cloud-compatible tools such as OpenSARlab (Meyer et al., 2021) allow the possibility to run data accessing and processing within the cloud alongside the ASF DAAC InSAR archive. The elimination of the need for data downloading improves processing efficiency and diminishes the cost of data storage remarkably, especially for large-area applications. The generated InSAR displacement time series are validated by comparison with Global Navigation Satellite System (GNSS) observations. Temporal and spatial patterns of the crustal deformation are used to track the evolution of the along-arc volcanism and evaluate the interaction between regional tectonic environments and magmatism.

4.3 Data and Methods

ARIA S1-GUNW products generated from the Sentinel-1 A/B datasets are used to produce the line of sight (LOS) deformation time series for more than 20 volcanoes, from Mt. Gareloi in the west to Mt. Veniaminof in the east (figure 1a). A total of ~4700 geocoded unwrapped interferograms are produced from SAR images acquired from 14 different satellite acquisition tracks (figure 1b), spanning the observation period from 2015 to 2021. Only SAR data collected during summers from June to October are exploited for the analyses to avoid coherence loss induced by snow/ice coverage in winter (Lu and Dzurisin, 2014). Only SAR pairs in the neighboring summers are used to produce the ARIA GUNW products. The Sentinel-1 images acquired from ascending and descending orbits are processed within a multi-looked scheme to suppress the noise and improve the interferometric coherence (Lee et al., 1994). Look numbers of 7 and 19 in azimuth and range directions are used, respectively, which are standard ARIA processing parameters. The interferograms in radar coordinates are geocoded to geographic coordinates with 3 by 3 arc second resolution for further analysis.

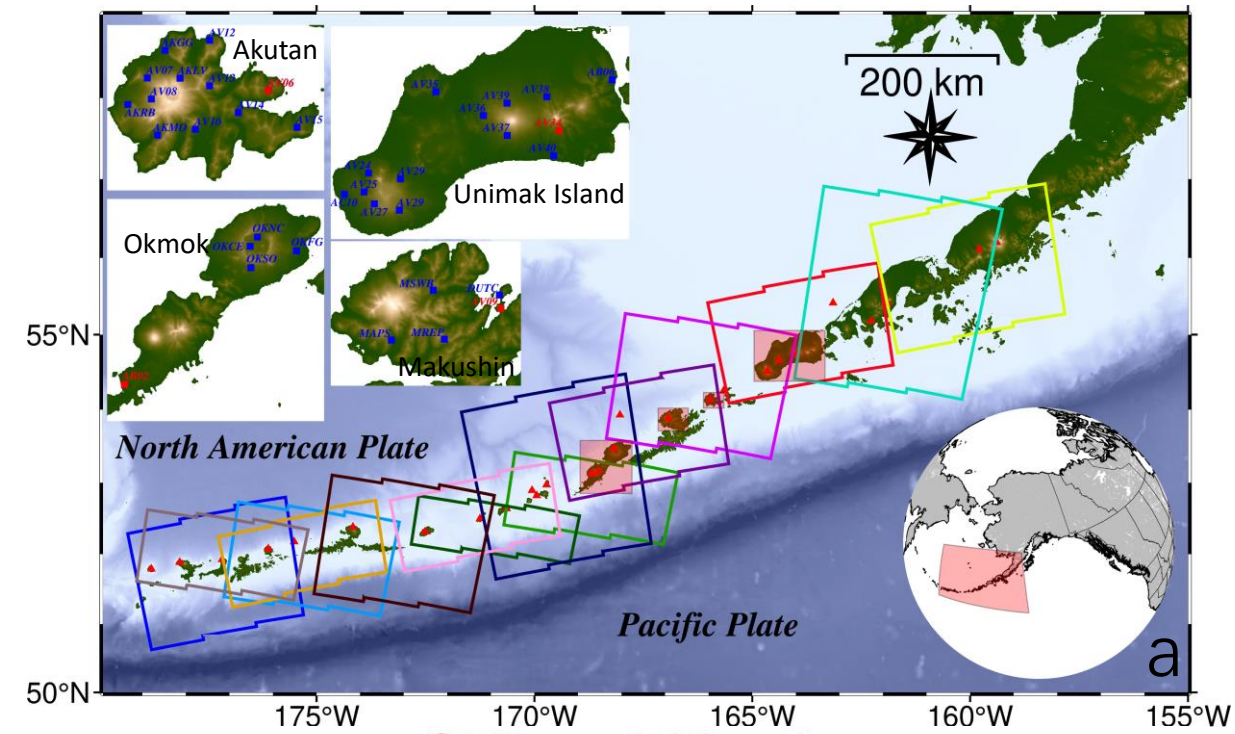
Akutan
Unimak Island
Okmok
Makushin
200 km
North American Plate
Pacific Plate
55°N
50°N
175°W
170°W
165°W
160°W
155°W
a

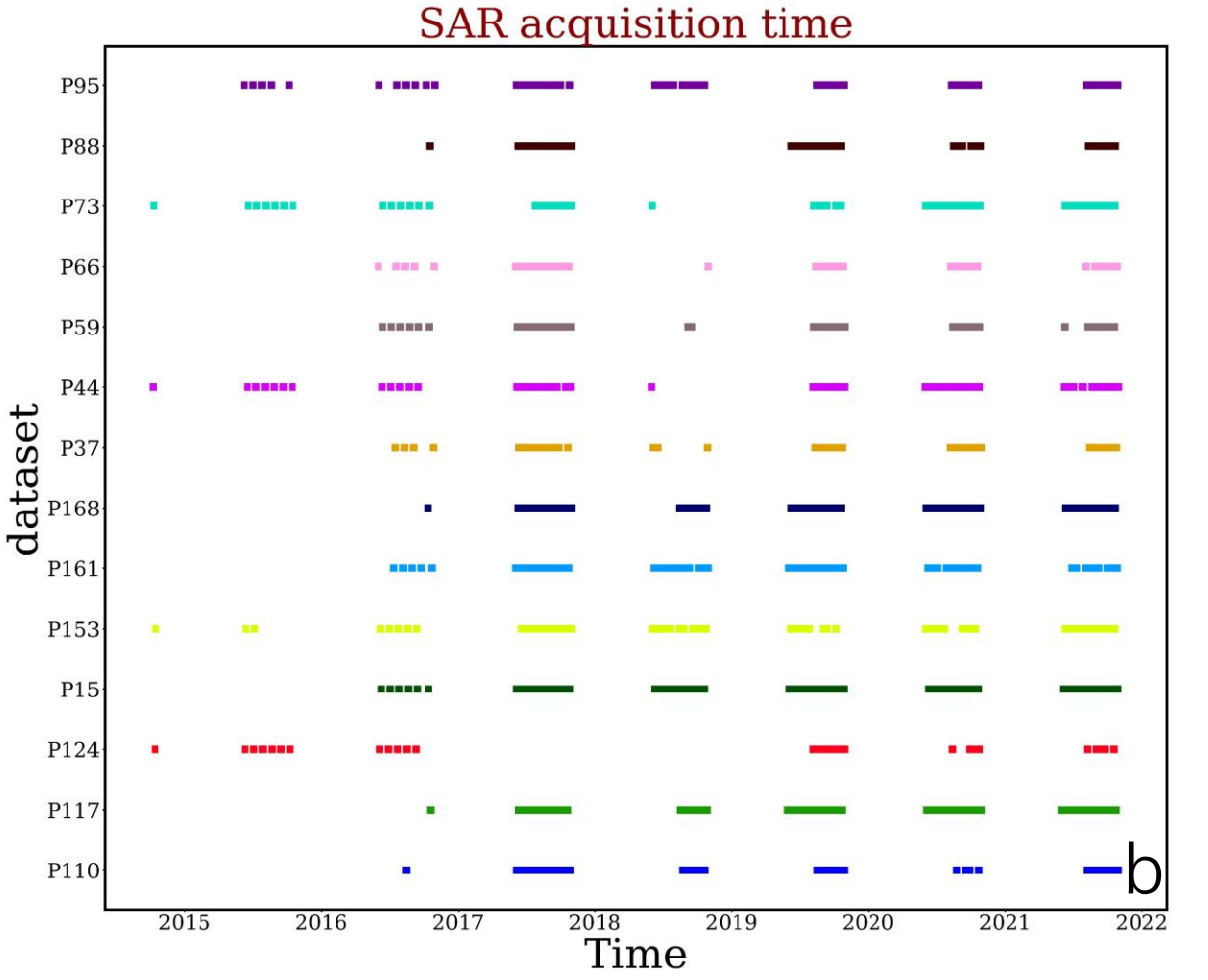
SAR acquisition time
dataset
P95
P88
P73
P66
P59
P44
P37
P168
P161
P153
P15
P124
P117
P110
2015
2016
2017
2018
2019
2020
2021
2022
Time
b

Figure 4.1. (a) Spatial coverage of the Sentinel-1 SAR acquisitions used for deformation mapping in the western and central Aleutian. Historically active volcanoes are marked with red triangles. Solid line boxes are the footprints of the ARIA S1-GUNW frames, colored by track names in (b) Insets are the four locations, i.e., Okmok, Makushin, Akutan, and Unimak Island, used for validation of the derived InSAR results, using the continuous GNSS stations (blue squares) and reference stations (red squares). (b) Temporal distribution of the SAR data.

InSAR measurements are prone to perturbation by multiple types of noise, e.g., phase delay due to atmospheric phase screen (APS), phase ramp induced by baseline errors, and unwrapping errors caused by low coherence or phase discontinuities ((Bekaert et al., 2015; Fattahi & Amelung, 2014; Li et al., 2009; Zhang et al., 2019). Some of the central Aleutian volcanoes are deployed with continuous GNSS (cGNSS) stations, which provide sustained observations of crustal movement (Blewitt et al., 2018). The derived InSAR time-series measurements are compared and validated with the cGNSS records at four locations (Okmok, Makushin, and Akutan volcanoes and Unimak Island; Figure 4.1a). A total of 36 stations maintained by the University of Alaska Fairbanks (UAF) and EarthScope are installed at these locations. All stations were operational during the observation period from 2015 to 2021 coinciding with the InSAR measurements, and stations are all covered in the coherent InSAR deformation maps, providing great test sites for our application.

The production of InSAR time-series deformation maps over the western and central Aleutian volcanoes is accomplished through two stages - the large-scale production of the ARIA S1-GUNW products and then the time series inversion with the multi-temporal InSAR stacks. We perform the time-series processing within the OpenSARlab. Layers of the ARIA GUNW products are extracted for time-series ingestion with the ARIA tools (Buzzanga et al., 2020; Sangha, 2021). Sentinel-1 tracks with multiple adjacent frames along the satellite track are

stitched to generate seamless interferograms with complete spatial coverage. We leveraged the ARIA-tools virtual data processing which allows accessing of virtual files from uniform resource locator pointing to on-cloud data and data loading from memory to save computation resources. Due to the spatially segregated characteristics of the Aleutian Islands, pronounced phase jumps between islands may be introduced during phase unwrapping. We employ an island-wise processing strategy to avert this situation. Isolated islands with reliable relative measurements are detected and separated with Global Self-consistent Hierarchical High-resolution Shorelines (GSHHS) water mask. The separated islands are then used in subsequent analysis.

The open-source Miami InSAR Time-series software in Python (MintPy) (Zhang et al., 2019) is applied to reconstruct the surface displacement history based on Small Baseline Subset (SBAS) algorithm (Berardino et al., 2002). The SBAS network is designed to keep robust connectivity and maximize the common intersection of the connected components for each interferogram, which is a metric for the quality of phase unwrapping with SNAPHU (Chen and Zebker, 2002). Unwrapping error correction is applied using the bridging and phase closure methods (Zhang et al., 2019). APS effects are mitigated with PyAPS (Jolivet et al., 2011) using the ERA5 weather model. To validate the InSAR measurements, constant tectonic corrections are made to the cGNSS records at Okmok, Akutan, Makushin, and Unimak Island, by subtracting the measurements of stations located in regions with no volcanic deformation (Figure S4.1). The three-dimensional cGNSS records are then projected to the LOS direction and compared with the InSAR measurements. The derived displacement time series at several volcanoes are used to model deformation source parameters using Geodetic Bayesian Inversion Software (GBIS) (Bagnardi & Hooper, 2018).

4.4 Results

Surface displacement histories in the LOS direction have been produced at 25 historically active volcanoes from 2015 to 2021 illuminating diverse spatial and temporal deformation patterns (Figure 4.2). Persistent surficial subsidence on the flanks of volcanoes or inside volcanic calderas is identified at Gareloi, Kanaga, Atka, Amukta, Cleveland and Pavlof, with amplitudes ranging from 0 to about 20 mm/yr. The spatial distributions of the subsidence are highly correlated with the surface lava flow and pyroclastic deposits produced by previous eruptions (Lu and Dzurisin, 2014), and have relatively stable subsidence rates. Persistent, caldera-centered subsidence with steady rates and spatial patterns produced from deeper processes are revealed at the western caldera (7.2, Figure 4.2) and eastern caldera (7.3, Figure 4.2) of Seguam, and Fisher caldera (21, Figure 4.2), with deflating rates of about 10, 5, and 10 mm/yr, respectively. Persistent dominant subsidence as well as minor uplift episodes have been recorded at the Atka volcanic center since 2016. Yunaska has been subsiding at a steady rate of about 20 to 30 mm/yr in the central caldera since 2016.

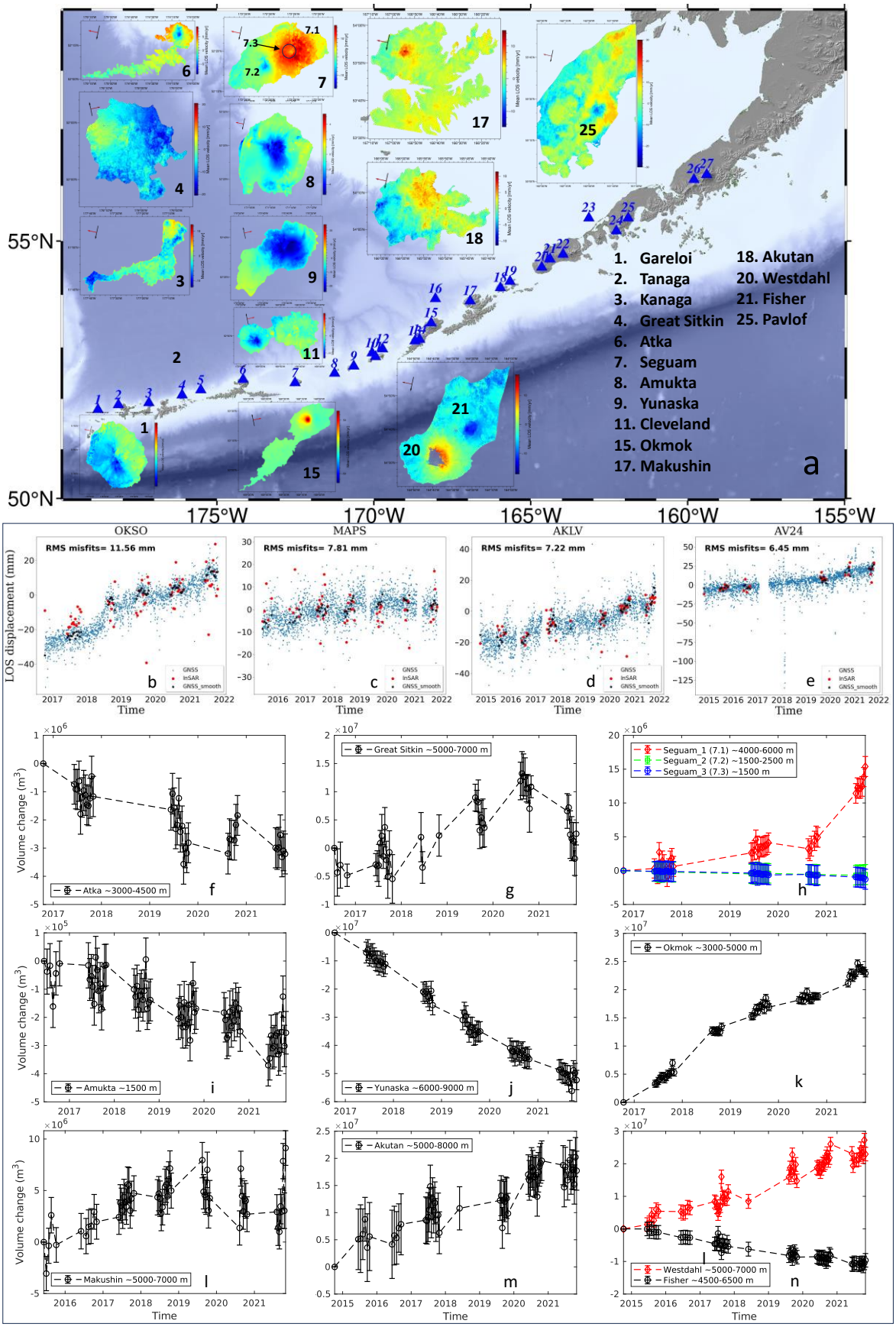
55°N
50°N
175°W
170°W
165°W
160°W
155°W
1. Gareloi
2. Tanaga
3. Kanaga
4. Great Sitkin
6. Atka
7. Seguam
8. Amukta
9. Yunaska
11. Cleveland
15. Okmok
17. Makushin
18. Akutan
20. Westdahl
21. Fisher
25. Pavlof
a
OKSO
MAPS
AKLV
AV24
RMS misfits= 11.56 mm
RMS misfits= 7.81 mm
RMS misfits= 7.22 mm
RMS misfits= 6.45 mm
LOS displacement (mm)
GNSS
InSAR
GNSS_smooth
Time
Volume change (m³)
Great Sitkin ~5000-7000 m
Seguam_1 (7.1) ~4000-6000 m
Seguam_2 (7.2) ~1500-2500 m
Seguam_3 (7.3) ~1500 m
Atka ~3000-4500 m
Amukta ~1500 m
Yunaska ~6000-9000 m
Okmok ~3000-5000 m
Akutan ~5000-8000 m
Makushin ~5000-7000 m
Westdahl ~5000-7000 m
Fisher ~4500-6500 m

Figure 4.2. (a) Surface deformation velocity in LOS direction estimated from the Sentinel-1 acquisitions over the western and central Aleutian volcanoes. Color ranges are different for each volcano due to the wide range of velocities. The volcano's location is shown as the number tag. The three different deformations at Seguam, i.e., eastern caldera, western caldera, and center of the eastern caldera, are labeled 7.1, 7.2 and 7.3, respectively. Volcanoes with no observed deformation or loss of interferometric coherence are not listed here. (b-e) Comparison between InSAR and GNSS measurements in the LOS direction at example GNSS stations shown in Figure 1a. Additional comparison results can be found in Figure S1. (f-n) Volume change histories at volcanoes with deep-seated inflation/deflation sources. The approximate depths of the Mogi sources are labeled.

Caldera-wide inflations with time-varying rates and spatially stable distributions are revealed at Seguam, Okmok, Makushin, Akutan, and Westdahl. Rapid inflation at a rate of about 60 to 80 mm/yr is identified from the eastern caldera of Seguam from 2020 to 2021 (7.1). Episodic exponential uplifts have been observed from the central caldera of Okmok since 2015, with an average deformation rate larger than 70 mm/yr. An uplift episode with an average rate of about 10 mm/yr has been identified at Makushin covering the whole caldera from 2015 to 2018, followed by subsidence with a similar spatial scale. Multiple episodic inflation events with average rates at about 5 mm/yr are observed to the northeast of the Akutan caldera. Westdahl has been persistently inflating from the central caldera at a steady rate of about 10 mm/yr since 2015. Great Sitkin exhibits inflation between the 2018 and 2020 eruption, and then contraction in 2021.

Most of the deep-seated deformation can be reproduced with a single Mogi source, i.e., a point source embedded in a homogeneous and isotropic elastic half space (Kiyoo, 1958). Deep-seated subsidence at Seguam, Amukta, Fisher, and Yunaska (section 4.6.1) can be reproduced from Mogi sources located at a depth range of about 1500 to 9000 meters BSL (Figure 4.2).

Deformation at Atka and Makushin have the best-fit Mogi source located at a depth from about 3000 to 7000 meters BSL (Figure 4.2). Inflation observations at the eastern caldera of Seguam, Okmok, Akutan, and Westdahl are produced by sources located about 4000 to 7000 km BSL (Figure 4.2). Inflation at Great Sitkin can be approximated by a Mogi source at a depth of about 5000-7000 meters BSL (section 4.6.2). Deformation at Tanaga can be fit by a strike-slip fault at a depth of about 4 km BSL (Section 4.6.3).

The general consistency between InSAR and cGNSS measurements, with root mean square (RMS) misfits of around or less than 1 cm at most stations, indicates that the InSAR results capture the volcanic deformation well (Figure 4.2 (b-e) and Figure S4.1). The notable deviation between InSAR and cGNSS at Okmok's OKCE is most likely a consequence of the decorrelation noise in regions with rapid deformation. It can be resolved by using datasets with higher spatial resolution and temporal sampling. The overall good agreements between the cGNSS and InSAR results validate the accuracy and robustness of the cloud-based time-series InSAR deformation mapping framework.

4.5 Temporal and spatial characteristics of the along-arc volcanism

Diversities in temporal and spatial domains are the most pronounced characteristics of the deformation patterns in the western and central Aleutian volcanoes. Two major inflation patterns are identified - continuous inflation events produced from spatially steady sources at time-varying rates at Okmok, Akutan and Westdahl, and episodic inflation events that occur intermittently at Great Sitkin, Seguam and Makushin. The persistent inflation events are the continuation of successive inflation periods that started prior to 2015, with similar source locations and depths (Lu et al., 2010; Wang et al, 2018, 2021; Xue & Freymueller, 2020). The inflating episodes detected at Seguam and Makushin are analogous to the ones in previous

deformation surveys and are very likely produced from the same sources (Lee et al., 2013; Xue & Freymueller, 2020). The persistent inflation observations likely indicate continued magma supply to the existing magmatic reservoirs and are usually associated with more persistent temporal patterns while the episodic inflation episodes show more intermittent features and are typically suggestive of magma accumulations in stages. Despite the deficiency of effective deformation monitoring before the 1990s, persistent inflation events are only seen over the central Aleutians while episodic inflation is widely seen in both the western and central Aleutians. Temporally and spatially steady shallow deflations correlated to the emplaced lava flow and pyroclastic deposits are produced from thermoelastic contraction (Dzurisin et al., 2019; Lu and Dzurisin, 2014). Persistent deep-seated deflation observations are likely produced by degassing, viscoelastic relaxation, or contractional hydrothermal/magma cooling (Hamling et al., 2014; Lee et al., 2013; Lu & Dzurisin, 2014; Mann & Freymueller, 2003). Long-term subsidence at varying spatial scales is rather common in the western and central Aleutian. This is indicative of recent eruptive activity and active magmatic systems. The subsidence is usually accompanied by other volcanic deformation, e.g., episodical inflations at Atka and Makushin. Volcanoes can also erupt without deforming the crust. Several eruptions have been produced from Cleveland, Shishaldin, and Pavlof during our observation period. However, no appreciable deformation was found associated with these eruptions. The absence of co-eruptive deformation has also been confirmed in previous observations and is likely produced by open-conduit plumbing systems or deep magma reservoirs (Lu and Dzurisin, 2010). Eruptions without volcano-wide deformation are only observed in the central Aleutian and are associated with much higher eruption frequency (Figure S4.2). Deformation at Tanaga is believed to be produced from strike-slip faulting (section 4.6.3). Earthquake-induced crustal deformations are rarely observed in InSAR at

volcanoes in the western and central Aleutian since volcanic-tectonic (VT) earthquakes are usually not big enough to produce crustal deformation appreciable to InSAR.

Significantly higher magma influx rates are observed in the central Aleutian, represented by the much larger volume accumulations from Okmok, Akutan, and Westdahl, as well as more frequent eruptions produced from Cleveland, Shishaldin and Pavlof during our observation period. The much higher magma influx rates are also consistent with the higher historic eruption frequency in the central Aleutian (Figure S4.2). A majority of the confirmed eruptions in the western and central Aleutian were produced from 7 volcanoes from Cleveland to Pavlof since about 1800s. Observations from volcanic CO_2 emissions, which have been measured 1 order of magnitude larger than those in the western Aleutian (Fischer et al., 2021), also agree with the high magma influx rate in the central Aleutian. The distinction in volcanism between the western and central Aleutian is likely a result of spatial variations in regional tectonics. The higher down-slip rates of the subducting Pacific Plate in the central Aleutian provide more water-rich sediments for the production of primitive magma from the partial melting of the mantle wedge (Buurman et al., 2014; DeMets et al., 1994; Kelemen et al., 2003; Kreemer et al., 2014). The dominant extensional tectonic setting created by probably the curvature of the arc may promote the magma ascent rate in the central Aleutian by providing a preferential pathway for magma migration (Magee et al., 2013; Ruppert et al., 2012).

4.6 Newly discovered deformation

4.6.1 Yunaska

Persistent caldera-wide deflation with a constant rate has been detected at Yunaska since 2015, where only surficial subsidence attributed to thermoelastic contraction of historically emplaced lava flows were detected in previous InSAR survey from 2004 to 2009 (Lu and

Dzurisin, 2014). Our modeling results suggest a best-fit Mogi source located about 8 km beneath the center of the caldera, with an average volumetric change rate of about $-58 \times 10^6\ m^3/yr$ (Figure S4.3). A wide variety of volcanic processes have been suggested to explain large-scale deep-seated surface deflation at volcanoes worldwide such as magma drainage from the reservoir during eruption (Geist et al., 2008; Lu & Dzurisin, 2010; Ofeigsson et al., 2011), viscoelastic relaxation of the crustal shell surrounding the magma chamber (Townsend, 2022), thermal contraction produced by magma/hydrothermal system cooling (Gong et al., 2015; Lee et al., 2013; Wang & Aoki, 2019), degassing or fluid loss (Nakaboh et al., 2003; Shreve et al., 2022; Trasatti et al., 2019). The most recent eruption recorded at Yunaska occurred in 1937, rejecting the co-eruptive deflation scenario (Lu and Dzurisin, 2014). Cooling-induced subsidence is typically initiated after the magma intrusion and can be persistent over a long time, in which case deflation should have also been detected in previous InSAR surveys. Degassing and fluid loss are usually associated with hydrothermal systems, yet no hot springs or active fumaroles are known to exist on Yunaska Island (avo.alaska.edu). One possible interpretation for the volume loss is magma or hydrothermal fluid drainage from the magmatic reservoir through fractures and accommodated by space produced in the crust by regional extensional stress regime, which may also be responsible for the continuous deflation observed at Askja and Krafla volcanoes in Iceland (de Zeeuw-van Dalfsen et al. 2005; Rymer et al., 1998). Draining to a deeper level is not favorable for undegassed magma, for which horizontal sills are more likely to propagate (Tibaldi et al., 2010). Lateral or upward movement of mass in the plumbing system is expected to be associated with signals in the form of earthquake swarms or seismic tremors. Yunaska is among one of the most seismically quiescent islands in the Aleutian arc, no seismic anomaly coeval the deflation is detected. However, this hypothesis cannot be ruled out. The absence of seismic

anomaly may be a result of the lack of nearby seismic stations as the nearest seismic stations are located on Herbert and Chuginadak Island in the east, with an average distance of about 50 km, which may not be able to detect the microseismicity produced during the magma/hydrothermal fluid transportation. Surface deformation is expected to be seen if magma migrates laterally or flows into shallow ponds in the scenario of incompressible magma and host rocks. While de Zeeuw-van Dalfsen et al (2013) showed that in the case of variable compressibility of magma residing in the plumbing system and host rocks, the strain change in the crust can be accommodated without producing detectable surface deformation. Further work is needed to provide additional constraints to the observed deflation, e.g., seismological observations to outline the pathways for mass transportation and micro-gravity observations to confine the magnitude of the possible mass relocation.

4.6.2 Great Sitkin

Two explosive eruptions were produced at Great Sitkin from the center crater in 2018 and 2021. The 2018 event started in June 2018 and ended in December 2018. The 2021 eruption started in May 2021 and has been characterized by sustained, slow lava effusions as of October 2023. With both these two eruptions captured in our InSAR observation period, we have identified one inflation episode that initiated around September 2018 and peaked around September 2020, and then diminished rapidly around October 2021. The inflation can be well reproduced by a Mogi source located ~800 m south and ~1.5 km west of the caldera center at a depth of about 5-7 km BSL, with a volume change rate of about $5.4 \times 10^6\ m^3/yr$ (Figure S4.4).

The inflating Mogi source from 2018 to 2020 is most likely indicative of magma accumulation in the magma chamber below the summit caldera that fed the 2021 eruption. Pesicek et al. (2008) identified a low P wave velocity region with appreciable thickness

extending from the surface to ~10 km depth beneath the summit caldera, with shallow earthquakes (<5 km) spread in a wide depth range within a small region beneath the summit. The shallow part (<5 km) of the low P-wave velocity region with high seismicity concentration and shallow long-period (LP) events is interpreted as the active hydrothermal system of Great Sitkin. The deeper part (>5 km) of the low P-wave velocity region is suggested to be a region with high-temperature anomaly and/or partially molten rock which may represent the magma storage (Pesicek et al., 2008). The location and depth of this low P-wave velocity zone are highly consistent with the Mogi source derived from our InSAR observation. Deep LP events have also been recorded at Great Sitkan in Power et al. (2004), in which the deep LP events are suggested to represent magma ascent from the upper mantle or lower crust to feed a shallow magma chamber. From 2015 to 2021, several seismic swarms were detected mainly in a NW-SE trending zone at Great Sitkin, distributed in a cap-like zone across the summit caldera (Figure S4.5). The deeper area (>5 km) with sparse seismicity capped by the seismic swarms may represent the region of the proposed magma reservoir. The shallow seismic swarms beneath the caldera concentrated from 2018 to 2020 may represent the elevated hydrofluid-magma interaction during the magma accumulation. The earthquake swarm right beneath the caldera in 2021 may be indicative of the rupture of the host rock surrounding the magma reservoir and the migration of the magma along the conduit. The deflation starting in August 2021 is consistent with the onset of the 2021 eruption. Furthermore, the volume of the lava dome produced during the 2021 eruption is estimated to have a volume of $\sim 2.4 \times 10^7\ m^3$ by October 2021 (https://avo.alaska.edu/activity/report.php?type=4&id=395381&mode=hans), which is close to the modeled volume loss in 2021 from InSAR ($\sim 1.5 \times 10^7\ m^3$, figure 2g). It is also worth noting that persistent volume increase is observed even during the 2018 eruption, considering the

phreatic nature of the 2018 eruption and the high seismicity rate between the 2018 and 2021 eruptions, we presume that both the two eruptions pertain to the same unrest cycle.

4.6.1 Tanaga

The Tanaga volcanic center is comprised of three young stratovolcanoes, i.e., Sajaka in the west, Tanaga in the middle, and Takawangha in the east. During October-November 2005, caldera-wide inflation centered between the Tanaga and Takawangha volcanoes was found accompanied by seismic unrest and was modeled as pressurization in a shallow dipping prolate spheroid source located about 3−5 km BSL (Lu and Dzurisin, 2014). In our InSAR observation, a large-scale transient deformation that occurred between November 2019 and August 2020 is found covering the whole northeastern part of Tanaga island, aligned near west-east with the northern part moving to the east and the southern part moving towards the west. The best-fit model is a nearly vertically dipping strike-slip fault located $10\ km$ east and $2500\ m$ north to the Takawangha caldera, striking to $\sim 80°$ clockwise to the north at a depth of $\sim 4\ km$ BSL, with a length of $\sim 11\ km$, a width of $\sim 600\ m$ and slip of $\sim 4\ m$ (Figure S4.6).

According to the USGS Comprehensive Earthquake Catalog (ComCat), several large swarms of earthquakes have been recorded in the E-SE of Takawangha from 2015 to 2021 (Figure S4.7). The 2020 earthquake swarm struck a large area extending from the peak of Takawangha to about 24 km to the N-NE, with more than 1000 events distributed at depths ranging from 18 km BSL to the surface. This seismic swarm coincides spatially with the deformation signal. Another seismic swarm between January 24 to 27 of 2017 includes about 100 events and is mainly distributed in a depth range of 4-12 km BSL. The shallowing depth trend with time may be indicative of stress perturbation due to the migration of magma or hydrofluid in cracks. The distribution of seismic clusters is consistent with the N70° trend of possible magma paths

derived from morphometric characteristics of the Tanaga volcanic center, which likely played a critical role in the activation of the large-scale strike-slip events in 2020 (Tibaldi and Bonali, 2017). Furthermore, the temporal distribution of seismic moment release, derived by converting the magnitude from local magnitude M_l and body-wave magnitude m_b to moment magnitude M_w using the imperial relation in Ruppert and Hansen (2010), shows very high moment concentrations in January 2020 (Figure S4.8). This is coeval with the occurrence of the transient deformation and is very likely accounting for the energy needed to produce the large-scale deformation. The strike angle and slip direction of the modeled fault are highly consistent with the nearby M5.0 and M6.6 earthquakes that occurred between Tanaga Volcano to the west and Kanaga Volcano to the east in May 2008 (Ruppert et al., 2012), suggesting the seismic swarm is a result of regional tectonics instead of magmatism. The strike-slip faulting may have been activated by stress perturbation or the presence of possible hydrofluid. Further investigation into the earthquake swarms and local fault information is needed to produce a better understanding of tectonic processes in this area.

4.7 Conclusion

Advanced cloud-based ARIA-HyP3 InSAR processing has been used to map the surface deformation history for the western and central Aleutian volcanoes. The ARIA tools and OpenSARlab cloud-based utilities remarkably reduce the computational resources and workflows for time-series deformation mapping over a large region. The framework shows great capability in capturing regional volcanic/nonvolcanic deformation with promising accuracy in challenging areas, providing a new option to better explore the value of both the archived and coming SAR data for the science community. The mapped deformation time series of the western and central Aleutian volcanoes show diverse spatial and temporal patterns and

variations, suggesting that the magmatic plumbing systems and tectonic settings along the arc are inherently complicated. An overall higher magmatism observed at the central Aleutian volcanoes is identified and may imply higher magma production rates or ascent rates as a result of regional tectonic settings. Most of the investigated volcanoes exhibit deformation identical to the historically observed patterns in previous studies, indicating similar magmatic activity occurring in their plumbing systems. New deformation patterns have been revealed at Tanaga, Great Sitkin and Yunaska, greatly enriching our knowledge of the spectrum of volcanism in the Aleutian arc. Transient deformation at Tanaga is suggested to be a result of multiple strike-slip earthquakes in response to regional tectonics. The 2018 eruption at Great Sitkin is interpreted as a result of magmatic reservoir rupture which accommodated lava dome emplacement during the 2021 eruption. The continuous deflation at Yunaska is speculated to be a consequence of magma withdrawal induced by the regional extensional tectonic setting. Updates on arc-wide volcanism are critical for further understanding of magmatism and tectonism, as well as volcanic hazard monitoring and mitigation.

4.8 Acknowledgements

We thank the ARIA-HYP3 team for producing the ARIA-GUNW data. This work was supported through the “enabling cloud based InSAR science” ACCESS 2019 award. Part of this work was carried out at the Jet Propulsion Laboratory, California Institute of Technology, under a contract with the National Aeronautics and Space Administration. J. Wang, Z. Lu and P. Gregg were also supported by NASA Earth & Surface Interior Program (80NSSC19K0357).

4.9 References

Bagnardi, M., & Hooper, A. (2018). Inversion of surface deformation data for rapid estimates of source parameters and uncertainties: A Bayesian approach. Geochemistry, Geophysics, Geosystems, *19*, 2194 – 2211. https://doi.org/10.1029/2018gc007585

Bekaert, D., Walters, R. J., Wright, T. J., Hooper, A. J., & Parker, D. J. (2015). Statistical comparison of InSAR tropospheric correction techniques. *Remote Sensing of Environment*, *170*, 40 – 47. https://doi.org/10.1016/j.rse.2015.08.035

Bekaert, D. P., Karim, M., Linick, J. P., Hua, H., Sangha, S., Lucas, M., et al. (2019). Development of open-access standardized InSAR displacement products by the advanced rapid imaging and analysis (ARIA) project for natural hazards. AGU Fall Meeting Abstracts. Retrieved from https://ui.adsabs.harvard.edu/abs/2019AGUFM.G23A..04B/abstract

Berardino, P., Fornaro, G., Lanari, R., & Sansosti, E. (2002). A new algorithm for surface deformation monitoring based on small baseline differential SAR interferograms. *TGRS*, *40*(11), 2375 – 2383. https://doi.org/10.1109/TGRS.2002.803792

Blewitt, G., Hammond, W. C., & Kreemer, C. (2018). Harnessing the GPS data explosion for interdisciplinary science [Dataset]. Eos, *99*(1029). 485. https://doi.org/10.1029/2018eo104623

Buurman, H., Nye, C. J., West, M. E., & Cameron, C. (2014). Regional controls on volcano seismicity along the Aleutian arc. *Geochemistry, Geophysics, Geosystems*, *15*(4), 1147 – 1163. https://doi.org/10.1002/2013GC005101

Buzzanga, B., Bekaert, D. P. S., Hamlington, B. D., & Sangha, S. S. (2020). Toward sustained monitoring of subsidence at the coast using InSAR and GPS: An application in Hampton roads, Virginia. *Geophysical Research Letters*, *47*(18), e2020GL090013. https://doi.org/10.1029/2020gl090013

Chen, C. W., & Zebker, H. A. (2002). Phase unwrapping for large SAR interferograms: Statistical segmentation and generalized network models. *IEEE Transactions on Geoscience and Remote Sensing*, *40*(8), 1709 – 1719. https://doi.org/10.1109/tgrs.2002.802453

de Zeeuw-van Dalfsen, E., Rymer, H., Sigmundsson, F., & Sturkell, E. (2005). Net gravity decrease at Askja volcano, Iceland: Constraints on processes responsible for continuous caldera deflation, 1988 – 2003. *Journal of Volcanology and Geothermal Research*, *139*(3), 227 – 239. https://doi.org/10.1016/j.jvolgeores.2004.08.008

de Zeeuw-van Dalfsen, E., Rymer, H., Sturkell, E., Pedersen, R., Hooper, A., Sigmundsson, F., & ófeigsson, B. (2013). Geodetic data shed light on ongoing caldera subsidence at Askja, Iceland. *Bulletin of Volcanology*, *75*(5), 1 – 13. https://doi.org/10.1007/s00445-013-0709-2

DeMets, C., Gordon, R. G., Argus, D. F., & Stein, S. (1994). Effect of recent revisions to the geomagnetic reversal time scale on estimates of current plate motions. *Geophysical Research Letters*, *21*(20), 2191 – 2194. https://doi.org/10.1029/94GL02118

Dzurisin, D., Lu, Z., Poland, M. P., & Wicks, C. W. (2019). Space-based imaging radar studies of U.S. Volcanoes. *Frontiers in Earth Science*, *6*. https://doi.org/10.3389/feart.2018.00249

Fattahi, H., & Amelung, F. (2014). InSAR uncertainty due to orbital errors. *Geophysical Journal International*, *199*(1), 549 – 560. https://doi.org/10.1093/gji/ggu276

Fischer, T. P., Lopez, T. M., Aiuppa, A., Rizzo, A. L., Ilanko, T., Kelley, K. A., & Cottrell, E. (2021). Gas emissions from the western Aleutians volcanic arc. *Frontiers in Earth Science*, *9*, 9. https://doi.org/10.3389/feart.2021.786021

Geist, D. J., Harpp, K. S., Naumann, T. R., Poland, M., Chadwick, W. W., Hall, M., & Rader, E. (2008). The 2005 eruption of Sierra Negra volcano, Galápagos, Ecuador. *Bulletin of Volcanology*, *70*(6), 655 – 673. https://doi.org/10.1007/s00445-007-0160-3

Gong, W., Meyer, F. J., Lee, C.-, Lu, Z., & Freymueller, J. (2015). Measurement and interpretation of subtle deformation signals at Unimak Island from 2003 to 2010 using weather model-assisted time series InSAR. *Journal of Geophysical Research: Solid Earth*, *120*(2), 1175 – 1194. https://doi.org/10.1002/2014JB011384

Hamling, I. J., Wright, T. J., Calais, E., Lewi, E., & Fukahata, Y. (2014). InSAR observations of post-rifting deformation around the Dabbahu rift segment, Afar, Ethiopia. *Geophysical Journal International*, *197*(1), 33 – 49. https://doi.org/10.1093/gji/ggu003

Jolivet, R., Grandin, R., Lasserre, C., Doin, M.-, & Peltzer, G. (2011). Systematic InSAR tropospheric phase delay corrections from global meteorological reanalysis data. Geophysical Research Letters, *38*(17), L17311. https://doi.org/10.1029/2011GL048757

Kelemen, P. B., Yogodzinski, G. M., & Scholl, D. W. (2003). Along-strike variation in lavas of the Aleutian island arc: Implications for the genesis of high Mg# andesite and the continental crust, inside the subduction factory. *Geophysical Monograph*, *138*, 223 – 276.

Kiyoo, M. (1958). Relations between the eruptions of various volcanoes and the deformations of the ground surfaces around them. *Earthquake Engineering Research Institute*, *36*, 99 – 134.

Kreemer, C., Blewitt, G., & Klein, E. C. (2014). A geodetic plate motion and global strain rate model. *Geochemistry, Geophysics, Geosystems*, *15*(10), 3849 – 3889. https://doi.org/10.1002/2014GC005407

Kwoun, O., Lu, Z., Neal, C., & Wicks, C. (2006). Quiescent deformation of the Aniakchak caldera, Alaska, mapped by InSAR. *Geology*, *34*(1), 5 – 8. https://doi.org/10.1130/G22015.1

Lee, C., Lu, Z., Won, J., Jung, H., & Dzurisin, D. (2013). Dynamic deformation of Seguam Island, Alaska, 1992 – 2008, from multi-interferogram InSAR processing. *Journal of Volcanology and Geothermal Research*, *260*, 43 – 51. https://doi.org/10.1016/j.jvolgeores.2013.05.009

Lee, J., Papathanassiou, K. P., Ainsworth, T. L., Grunes, M. R., & Reigber, A. (1998). A new technique for noise filtering of SAR interferometric phase images. *IEEE Transactions on Geoscience and Remote Sensing*, *36*(5), 1456 – 1465. https://doi.org/10.1109/36.718849

Li, Z., Fielding, E. J., & Cross, P. (2009). Integration of InSAR time-series analysis and water-vapor correction for mapping postseismic motion after the 2003 Bam (Iran) earthquake. *TGRS*, *47*(9), 3220 – 3230. https://doi.org/10.1109/TGRS.2009.2019125

Lu, Z., & Dzurisin, D. (2010). Ground surface deformation patterns, magma supply, and magma storage at Okmok volcano, Alaska, from InSAR analysis: 2. Coeruptive deflation, July-August 2008. *Journal of Geophysical Research*, *115*(B5), B00B03. https://doi.org/10.1029/2009JB006970

Lu, Z., & Dzurisin, D. (2014). *InSAR imaging of Aleutian volcanoes*. Springer.

Lu, Z., Dzurisin, D., Biggs, J., Wicks, C., Jr., & McNutt, S. (2010). Ground surface deformation patterns, magma supply, and magma storage at Okmok volcano, Alaska, from InSAR analysis: 1. Intereruption deformation, 1997 – 2008. *Journal of Geophysical Research*, *115*(B5), B00B02. https://doi.org/10.1029/2009jb006969

Lu, Z., Masterlark, T., Dzurisin, D., Rykhus, R., & Wicks, C., Jr. (2003). Magma supply dynamics at Westdahl volcano, Alaska, modeled from satellite radar interferometry. *Journal of Geophysical Research*, *108*(B7), 2354 – n/a. https://doi.org/10.1029/2002JB002311

Magee, C., Jackson, C. A. L., & Schofield, N. (2013). The influence of normal fault geometry on igneous sill emplacement and morphology. *Geology*, *41*(4), 407 – 410. https://doi.org/10.1130/G33824.1

Mann, D., & Freymueller, J. (2003). Volcanic and tectonic deformation on Unimak Island in the Aleutian arc, Alaska. *Journal of Geophysical Research*, *108*(B2), 2108. https://doi.org/10.1029/2002JB001925

Meyer, F. J., Rosen, P. A., Flores, A., Anderson, E. R., & Cherrington, E. A. (2021). Making sar accessible: Education & training in preparation for Nisar. In *2021 IEEE international geoscience and remote sensing symposium IGARSS*.

Nakaboh, M., Ono, H., Sako, M., Sudo, Y., Hashimoto, T., & Hurst, A. W. (2003). Continuing deflation by fumaroles at Kuju volcano, Japan. *Geophysical Research Letters*, *30*(7), 1396 – n/a. https://doi.org/10.1029/2002GL016047

Ofeigsson, B. G., Hooper, A., Sigmundsson, F., Sturkell, E., & Grapenthin, R. (2011). Deep magma storage at Hekla volcano, Iceland, revealed by InSAR time series analysis. *Journal of Geophysical Research*, *116*(B5), B05401. https://doi.org/10.1029/2010JB007576

Pesicek, J. D., Thurber, C. H., DeShon, H. R., Prejean, S. G., & Zhang, H. (2008). Three-dimensional P-wave velocity structure and precise earthquake relocation at Great Sitkin Volcano, Alaska. *Bulletin of the Seismological Society of America*, *98*(5), 2428 – 2448. https://doi.org/10.1785/0120070213

Power, J. A., Stihler, S. D., White, R. A., & Moran, S. C. (2004). Observations of deep long-period (DLP) seismic events beneath Aleutian arc volcanoes; 1989 – 2002. *Journal of Volcanology and Geothermal Research*, *138*(3), 243 – 266. https://doi.org/10.1016/j.jvolgeores.2004.07.005

Rosen, P. A., Gurrola, E., Sacco, G. F., & Zebker, H. (2012). The InSAR scientific computing environment. In *EUSAR 2012; 9th European conference on synthetic aperture radar*.

Ruppert, N. A., & Hansen, R. A. (2010). Temporal and spatial variations of local magnitudes in Alaska and Aleutians and comparison with bodywave and moment magnitudes. *Bulletin of the Seismological Society of America*, *100*(3), 1174 – 1183. https://doi.org/10.1785/0120090172

Ruppert, N. A., Kozyreva, N. P., & Hansen, R. A. (2012). Review of crustal seismicity in the Aleutian Arc and implications for arc deformation. *Tectonophysics*, *522–523*, 150 – 157. https://doi.org/10.1016/j.tecto.2011.11.024

Rymer, H., Cassidy, J., Locke, C. A., & Sigmundsson, F. (1998). The 1998 debris avalanche at Casita volcano, Nicaragua – Investigation of structural deformation as the cause of slope instability using remote sensing. *Journal of Volcanology and Geothermal Research, 87*(1 – 4), 141 – 149. https://doi.org/10.1016/S0377-0273

Sangha, S. S. (2021). *Characterizing the deformation field in Afar from radar interferometry and topography data*. University of California. Shreve, T., Grandin, R., & Boichu, M. (2022). Reservoir depressurization driven by passive gas emissions at Ambrym volcano. *Earth and Planetary Science Letters, 584*, 117512. https://doi.org/10.1016/j.epsl.2022.117512

Tibaldi, A., & Bonali, F. L. (2017). Intra-arc and back-arc volcano-tectonics: Magma pathways at Holocene Alaska-Aleutian volcanoes. *Earth-Science Reviews, 167*, 1 – 26. https://doi.org/10.1016/j.earscirev.2017.02.004

Tibaldi, A., Pasquarè, F., & Tormey, D. (2010). Volcanism in reverse and strike-slip fault settings. *New Frontiers in Integrated Solid Earth Sciences*, 315 – 348. https://doi.org/10.1007/978-90-481-2737-5_9

Townsend, M. (2022). Linking surface deformation to thermal and mechanical magma chamber processes. *Earth and Planetary Science Letters, 577*, 117272. https://doi.org/10.1016/j.epsl.2021.117272

Trasatti, E., Acocella, V., Di Vito, M. A., Del Gaudio, C., Weber, G., Aquino, I., et al. (2019). Magma Degassing as a source of long-term seismicity at volcanoes: The Ischia Island (Italy) case. *Geophysical Research Letters, 46*(24), 14421 – 14429. https://doi.org/10.1029/2019GL085371

Wang, J., Lu, Z., & Gregg, P. M. (2021). Inflation of Okmok volcano during 2008 – 2020 from PS analyses and source inversion with finite element models. *Journal of Geophysical Research: Solid Earth*, *126*(10), e2021JB022420. https://doi.org/10.1029/2021jb022420

Wang, T., DeGrandpre, K., Lu, Z., & Freymueller, J. T. (2018). Complex surface deformation of Akutan volcano, Alaska revealed from InSAR time series. *International Journal of Applied Earth Observation and Geoinformation*, *64*, 171 – 180. https://doi.org/10.1016/j.jag.2017.09.001

Wang, T., Poland, M. P., & Lu, Z. (2015). Dome growth at Mount Cleveland, Aleutian Arc, quantified by time series TerraSAR-X imagery. *Geophysical Research Letters*, *42*(24), 10614 – 10621. https://doi.org/10.1002/2015GL066784

Wang, X., & Aoki, Y. (2019). Posteruptive thermoelastic deflation of intruded magma in Usu volcano, Japan, 1992 – 2017. *Journal of Geophysical Research: Solid Earth*, *124*(1), 335 – 357. https://doi.org/10.1029/2018jb016729

Xue, X., & Freymueller, J. T. (2020). A 25-year history of volcano magma supply in the east central Aleutian arc, Alaska. *Geophysical Research Letters*, *47*(15), e2020GL088388. https://doi.org/10.1029/2020gl088388

Zhang, Y., Fattahi, H., & Amelung, F. (2019). Small baseline InSAR time series analysis: Unwrapping error correction and noise reduction. Computers & Geosciences, *133*, 104331. https://doi.org/10.1016/j.cageo.2019.104331

4.10 Supplementary

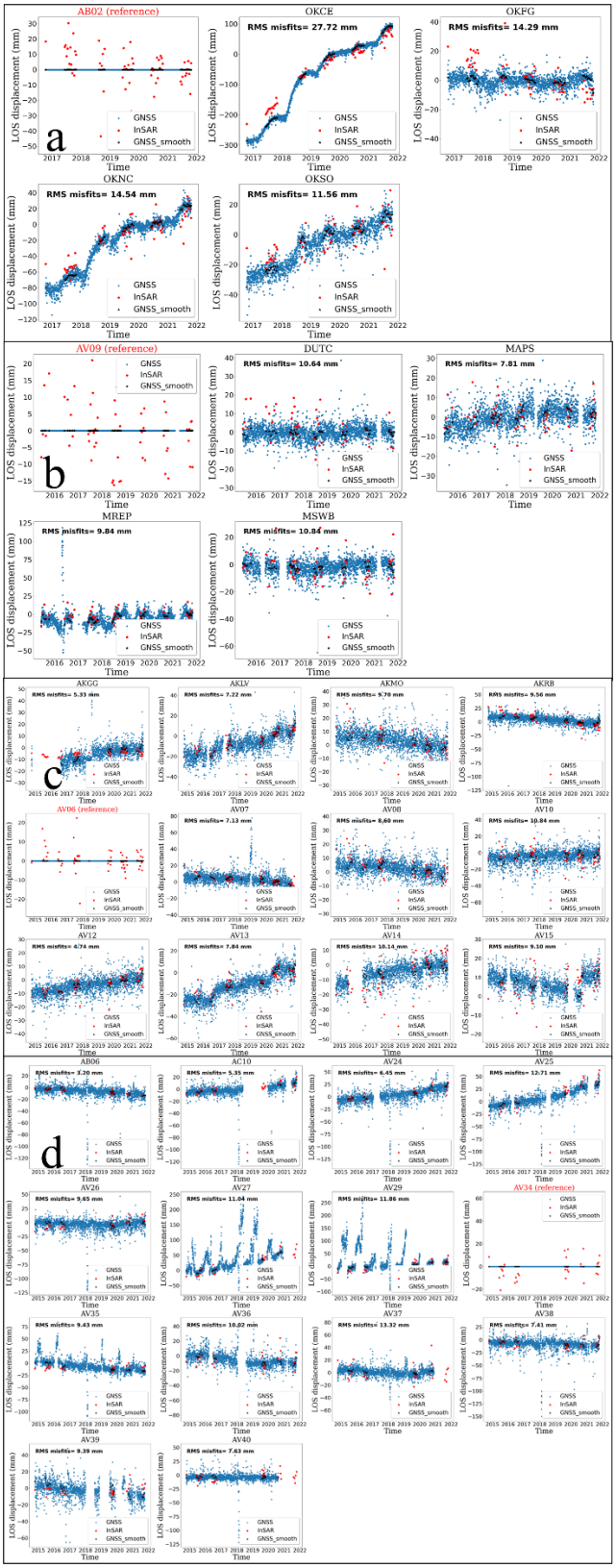

Figure S4.1. Comparison between InSAR and cGNSS at stations deployed at (a) Okmok, (b) Makushin, (c) Akutan, and (d) Unimak Island. GNSS records are referenced to sites without volcanic deformation (marked as reference) by subtracting the measurement of the reference station to remove tectonic deformation and then projected to the LOS direction of the corresponding InSAR track. At most of the GNSS sites, InSAR observations match well with the cGNSS records.

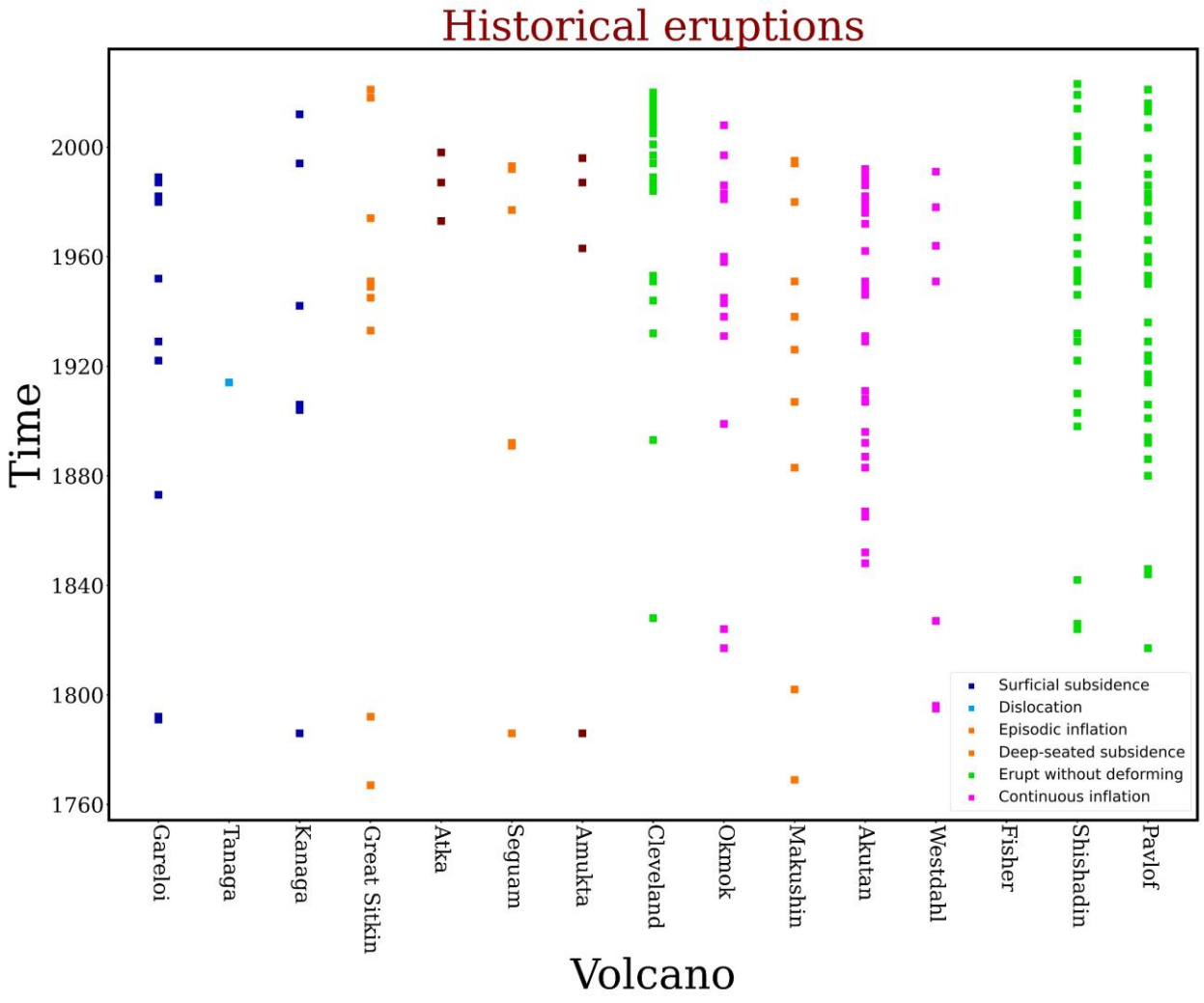

Figure S4.2. Confirmed historical eruption records started about 1800 for volcanoes with deformations. Volcanoes are sorted by locations and colored by dominant deformation types. Much higher eruption frequency can be identified from the central Aleutian from Cleveland to Pavlof.

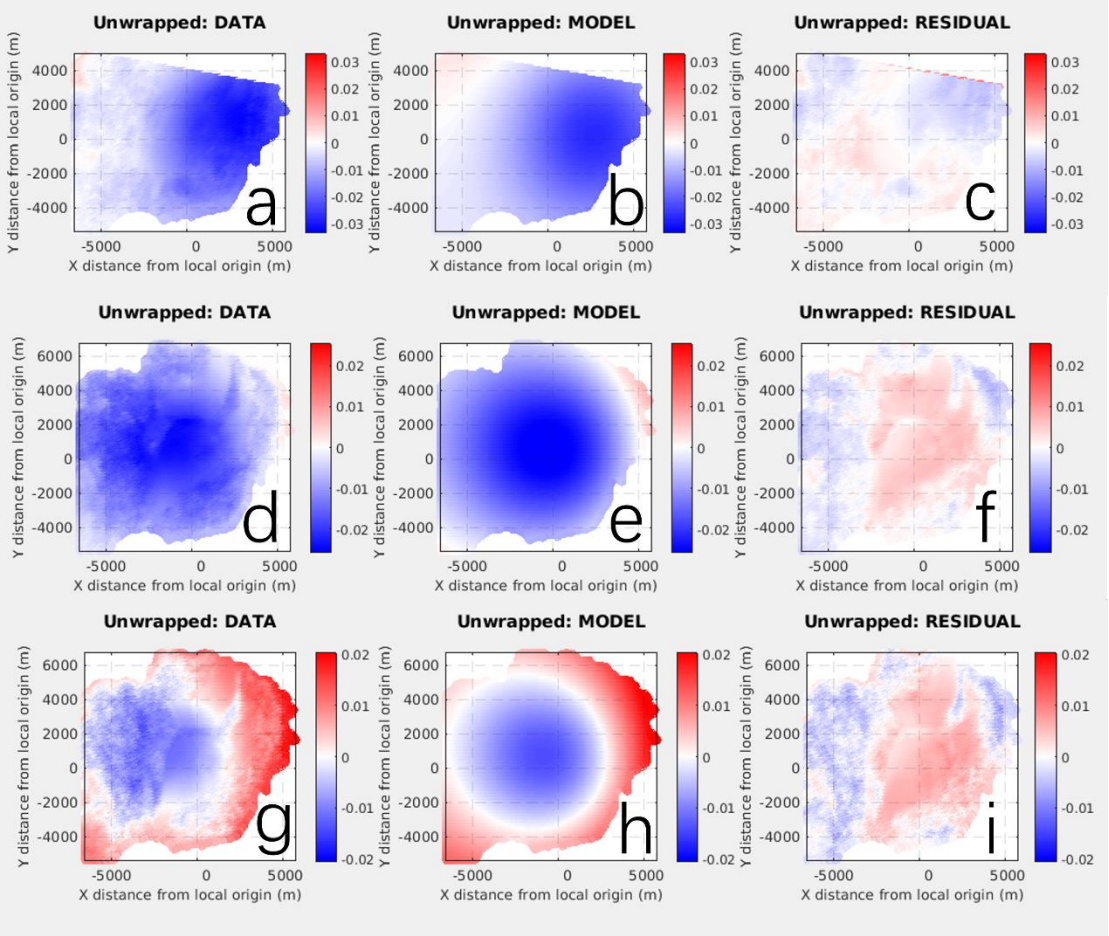

Figure S4.3. Observed (left column), modeled (middle column) and residual (right column) deformation velocity for Yunaska from InSAR track P15 (a, b, c, respectively), P168 (d, e, f, respectively), and P66 (g, h, i, respectively).

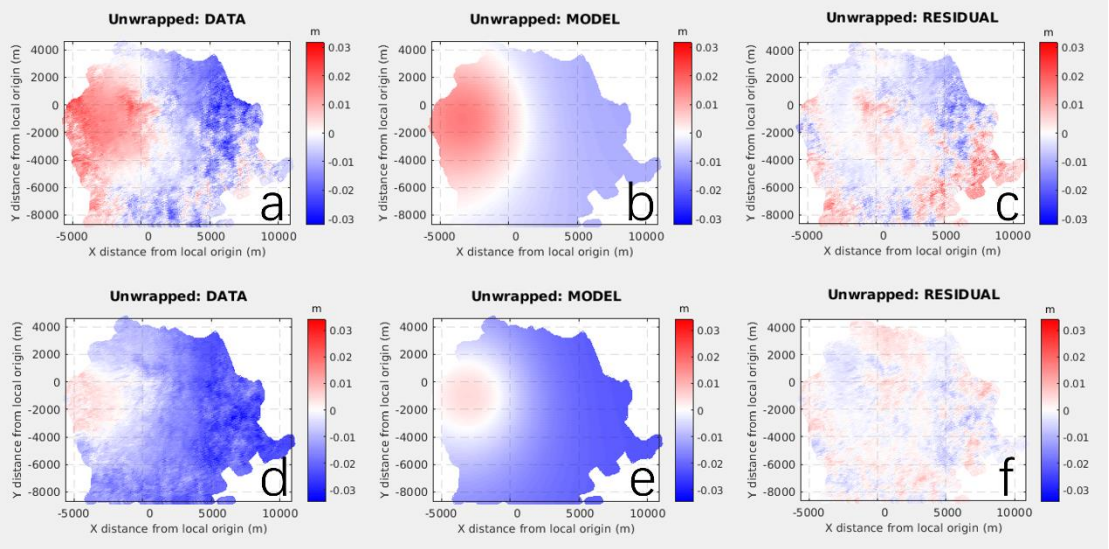

Figure S4.4. Observed (left column), modeled (middle column) and residual (right column) deformation velocity for Great Sitkin from InSAR track P110 (a, b, c, respectively), and P37 (d, e, f, respectively).

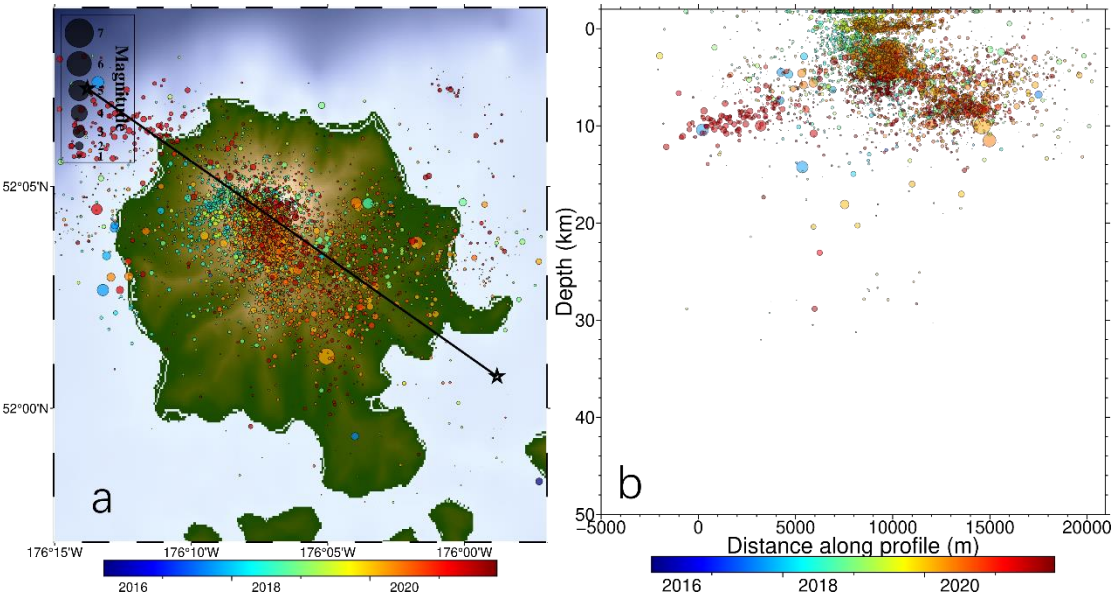

Figure S4.5. (a) Temporal-spatial distribution of seismic swarms (colored circles) at Great Sitkin from 2016 to 2021 during the InSAR observation period. (b) Earthquake locations projected to the profile denoted by the black line between the two black stars. The magnitude of the earthquake is represented by the circle size and the time by color.

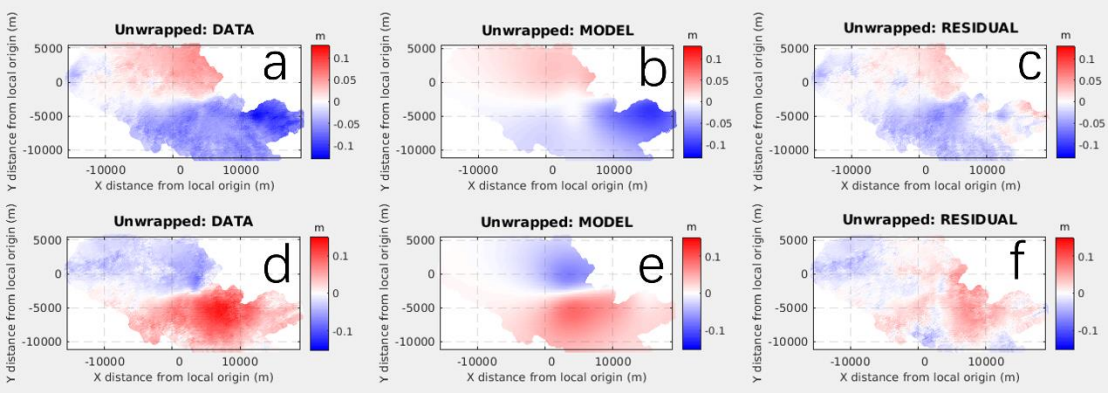

Figure S4.6. Observed (left column), modeled (middle column) and residual (right column) deformation velocity for Tanaga from InSAR track P59 (a, b, c, respectively) and P110 (d, e, f, respectively).

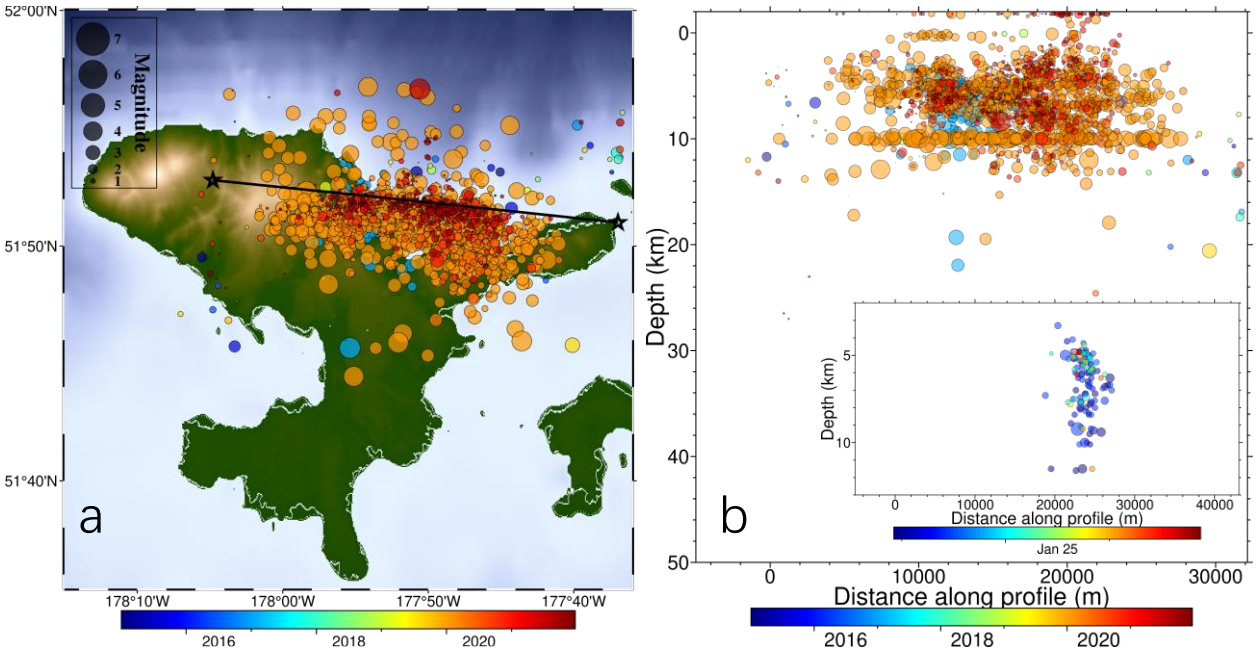

Figure S4.7. (a) Temporal-spatial distribution of seismic swarms (colored circles) at Tanaga from 2015 to 2021 during the InSAR observation period. (b) Earthquake locations projected to the profile denoted by the black line between the two black stars. The magnitude of the earthquake is represented by the circle size and the time by color. Inset is the earthquake swarm occured in January 2017.

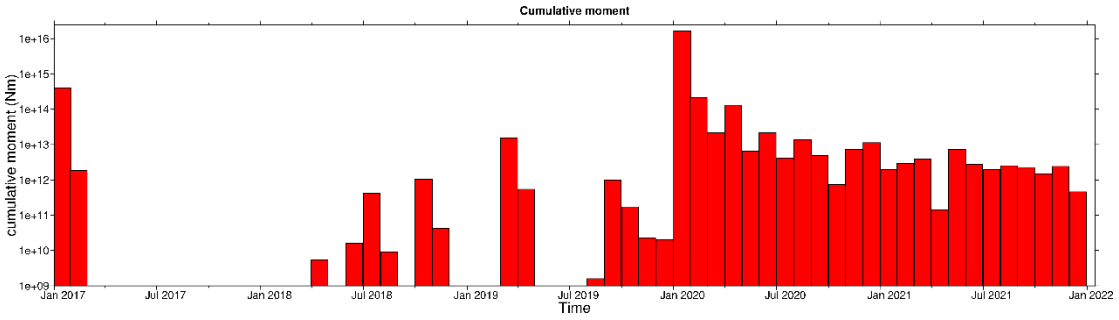

Figure S4.8. Cumulative monthly Moment distribution of the seismic swarms at Tanaga. Most of the energy release is concentrated in January 2020, which shares the same period of the transient deformation observed from InSAR.

CHAPTER 5
TOWARDS RECONCILIATION OF SEISMIC TOMOGRAPHY AND GEODETIC DEFORMATION OBSERVATION: A CASE STUDY AT OKMOK VOLCANO

5.1 Abstract

Surface deformation and seismic tomography are both crucial components for the study of volcanoes, providing insightful constraints to magma migration, storage, and subsurface structures. However, it is observed at many volcanoes that source locations derived from surface deformation and seismic tomography do not agree. In this study, leveraging comprehensive seismic observations and geodetic deformation measurements, we model the magma storage inside the complicated magmatic system with multi-physical models for the Okmok volcano. The predicted deformation suggests locations of the magmatic intrusion are characterized by regions with low V_p and V_s and moderate V_p/V_s ratio, instead of the regions with high V_p and V_p/V_s ratio and low V_s that are often interpreted as the presence of magma reservoirs or conduits (Kasatkina et al., 2022). This difference in interpretation underscores the complexity of magma reservoir dynamics, provides valuable insights into the nuanced interpretation of seismic data in volcanic environments, and highlights the needs for multi-disciplinary observations and multi-physical models to improve the interpretations of complex magma plumbing systems.

5.2 Introduction

Developments in both in-situ and remote-sensed earth observations have greatly increased the availability and volume of data for volcano monitoring and provide valuable insights to the magmatic systems. Seismic tomography images the 3D seismic wave velocity of the crust

materials, outlining the location, size, and structure of the plumbing systems while inverse models of surface deformation provide critical constraints on the locations and degree of magma migration/storage inside the reservoirs. However, it is often observed at many volcanoes that the source locations derived from geodetic deformation don't agree with those inferred from seismic tomography, e.g., Atka (Zhan et al., 2021; Koulakov et al., 2020), Great Sitkin (Wang et al., 2023; Yang et al., 2023), and Okmok volcano (Wang et al., 2021; Kasatkina et al., 2022). Derivation of the source parameters from inverse analysis of the surface deformation is highly dependent on the crust material heterogeneity and usually nonunique. Seismic tomography has been used to infer the specific distribution of the rheological properties of the crustal material, with which the modeled source depth can vary significantly, but still cannot explain the inconsistencies in the horizontal positions (Masterlark et al., 2012; 2016).

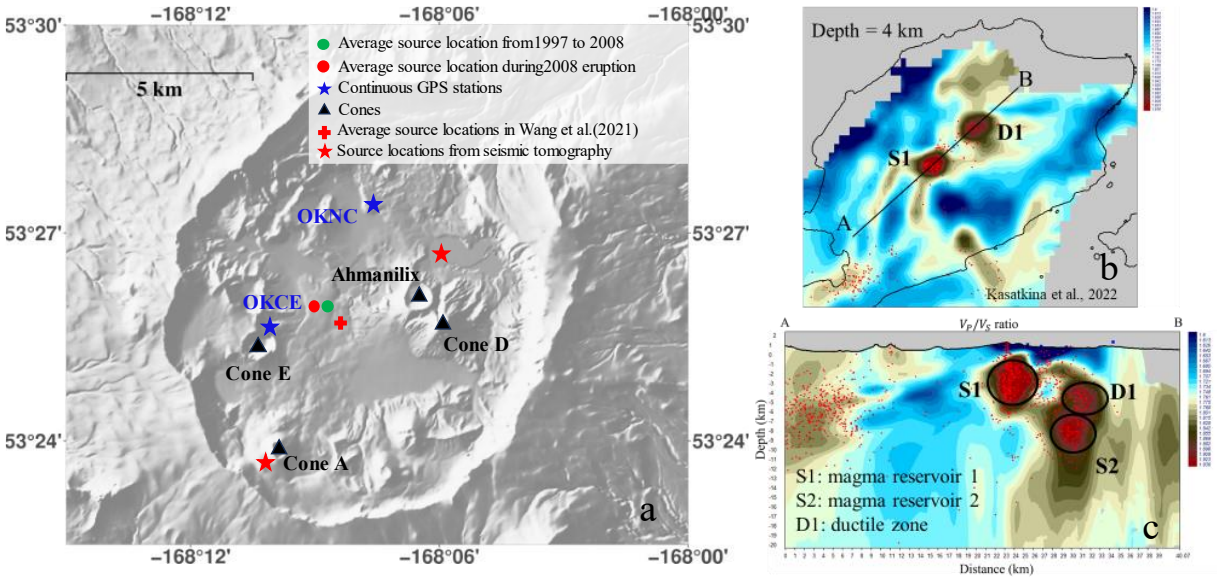

Figure 5.1. a) Average source locations derived from geodetic measurements (red/green circles and red cross) and the distributed sources inferred from seismic tomography (red stars). The distributed sources inferred from seismic tomography are represented by regions with high V_p and V_p/V_s ratio and low V_s. b) horizontal profile of V_p/V_s ratio of Okmok at 4 km depth. Solid line AB indicates the vertical profile shown in c).

Previous deformation surveys at Okmok volcano have identified magmatic sources located beneath the center of the caldera, at depth range ~2 km to ~5 km beneath sea level (Biggs et al., 2010; Mann et al., 2002; Lu et al., 2010). The latest seismic tomography results, on the contrary, suggest multiple distributed sources. Kasatkina et al. (2022) interpreted the regions with high V_p, low V_s and corresponding high V_p/V_s ratio scattered around the major cones, i.e., Cone A and D, as connected magmatic reservoirs (Figure 5.1). State-of-the-art modeling techniques allow integration of complicated source geometry, heterogeneous materials, tectonic stress conditions, as well as coupled hydro, thermal and mechanical processes, providing critical constraints to the location, strength, and evolution of the magmatic source (Segall et al., 2013, 2020; Zhan et al., 2021). In this study, we aim to interpret the discrepancies in magmatic sources derived from inverse models of surface deformation and seismic tomography using Finite Element Models (FEM). Source locations inferred from the seismic tomography are used to determine rheologic properties of the crustal material and are used to predict the crustal deformation, which is further compared with the geodetic measurements, providing valuable constraints for the interpretation of seismic tomography data and integration of multi-disciplinary observations for physical modeling of the complicated magmatic systems.

5.3 Numerical Models of the Okmok Volcanic System

Following Zhan et al. (2021), we build FEMs for Okmok volcano with COMSOL Multiphysics 6.1. The study area is modeled as a $100 \times 100 \times 30\ km$ block centered at the central caldera of Okmok. The crust materials are featured by spatially heterogenous rheology. Due to the large uncertainty, limited spatial coverage, and sparse resolution of the local seismic tomography, instead of deriving an elastic moduli with the empirical relationships between seismic wave velocity from the local seismic tomography and the linear elastic parameters, we

define the elastic moduli of the crust with constant Poisson's ratio (v) and depth- and temperature-dependent Young's modulus (E_{td}; Zhan et al., 2021):

$$E_{td} = \beta_T E_d$$

where E_d is the far field Young's modulus in the adjacent areas derived from regional mean crustal velocities assuming it is not affected by the heat from the magma (Fliedner & Klemperer, 1999). E_d is represented by

$$E_d = -0.0125z^2 - 1.25z + 40.25$$

where z is the depth. β_T is the temperature dependence coefficient defined as:

$$\beta_T = \frac{1}{2-2e}\left[\exp\left(\frac{T-T_d}{T_c-T_d}\right) + 1 - 2e\right]$$

where e is the base of the natural logarithm and $T_d = zdT/dZ$, with dT/dZ being the geothermal gradient (~$30°C/km$; Currie & Hyndman, 2006). Temperature distribution is calculated by solving a static thermal conduction model with the temperature of magmatic reservoir T_c set to $1100°C$ based on the basaltic and basaltic andesite products from previous eruptions (Larsen et al., 2009; 2013).

The initial stress of the FEM is determined based on gravity loading of water and crust materials. The surface elevation of the block is from the Copernicus Digital Elevation Model (DEM) and the SYNthetic BATHymetry (SYNBATH; Sandwell et al., 2022). The loading effect can produce vertical subsidence up to ~190 m, which is not negligible compared to the mean caldera elevation (~500 m). An iterative optimization is used to minimize the effect

$$h_{n+1} = h_n - \Delta h$$

where h_{n+1} is the updated input elevation and h_n is the input elevation for gravity loading computation during the n_{th} iteration, Δh is the surface deformation produced by the loading

effect. After initialization of the stress distribution, an overpressure is applied to the magma chamber walls to calculate the crustal deformation due to pressurization in the magmatic reservoir in response to magma accumulations. For a $1000 \times 1000 \times 500\ m$ spheroid source with overpressure of $2 \times 10^8\ Pa$ at $5000\ m$ depth, predicted surface deformation produced from the overpressure in the magma chamber can be deviated up to ~7% from that of models without topography optimizations (Figure 5.2).

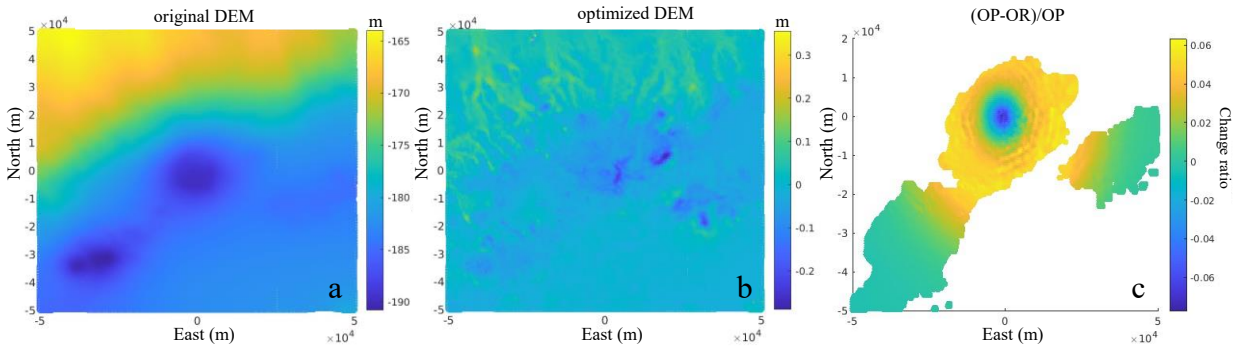

Figure 5.2. Difference between deformed crust elevation and the realistic elevation for model with original (a; OR) and optimized topography (b; OP) after gravity loading. Difference of surface deformation produced by overpressure between OR and OP.

5.4 Results

Two forward models are developed and tested based on the local seismic tomography (Kasatkina et al., 2022). The first model is featured by a multiple distributed source in the plumbing system with two ellipsoid magma chambers, each with a half-width of 1000 m and a half-heigh of 500 m, connected by a narrow cylindrical conduit C1 (Figure 5.3). The two magma chambers, hereafter referenced as S1 and S2, are positioned roughly beneath Cone A and Cone D, at depths of 4 km and 7 km BSL, respectively. S1 and S2 correspond to the magma reservoir

1 and 3 in Kasatkina et al. (2022), which are characterized by high V_p, low V_s and high V_p/V_s ratio. A ductile zone D1, which corresponds to the ductile zone 2 in Kasatkina et al. (2022) and lays above S2 at a depth of 5 km BSL characterized by weaker crust materials, is defined by a spheroid with the same size as S1 and S2 at a temperature of T_c. An overpressure ΔP is applied to the wall of S1, S2 and the conduit after the static heat transfer and gravity loading model. With the source locations and sizes fixed, we find an overpressure of $\sim 1.56 \times 10^8\ Pa$ produce the surface deformation that fits the geodetic measurements best. The peak of the predicted surface deformation is found in the vicinity of Cone A (Figure 5.4), contradictory to the deformation patterns observed from InSAR, which are centered near the central caldera and can be well approximated with Mogi sources (Wang et al., 2021).

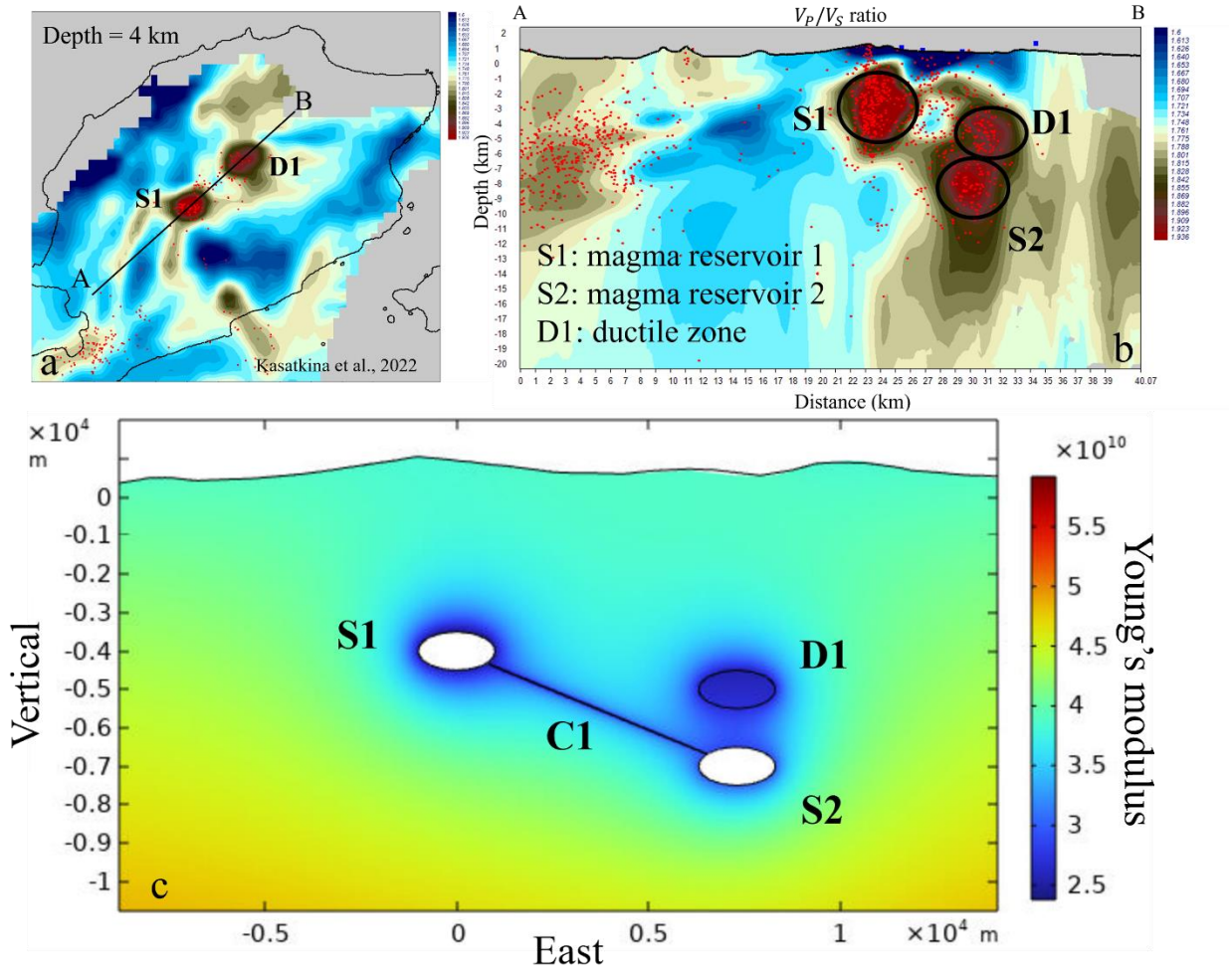

Figure 5.3. (a) Horizontal profile of V_p/V_s ratio at depth of 4 km BSL for Okmok volcano. Solid black line AB represents the cross-sections in figure (b). (b) shows the vertical profile of V_p/V_s ratio. (c) is a profile of the estimated Young's modulus for part of the areas shown in (b), with reference set to the point on the sea level above S1. Red dots in (a) and (b) are projections of the earthquakes within distances of 1 km to the profile. Magma chamber S1 and S2 are connected by a narrow conduit C1. Ductile zone D1 is featured as a hot solid spheroid.

The other model comprises of a single reservoir with the size same as S1 and S2, located beneath the center of the caldera at a depth of 4 km BSL, which corresponds to a region featured by anomalous low V_p and V_s and moderate V_p/V_s ratio surrounded by regions with high V_p/V_s

ratio (Figure 5.5). An overpressure of $\sim 1.51 \times 10^8\ Pa$ applied to the chamber wall produces LOS deformation that fits the InSAR observations well (Figure 5.6). The single reservoir model fits the deformation measurements much better than the distributed model. It should also be noted that the location of the source in this model is only about 1.5 km away from the ones derived from geodetic deformation measurements (Wang et al., 2021), suggesting that the single reservoir model might offer greater reliability in pinpointing the locations of magma intrusion within the plumbing system compared to the distributed reservoir model.

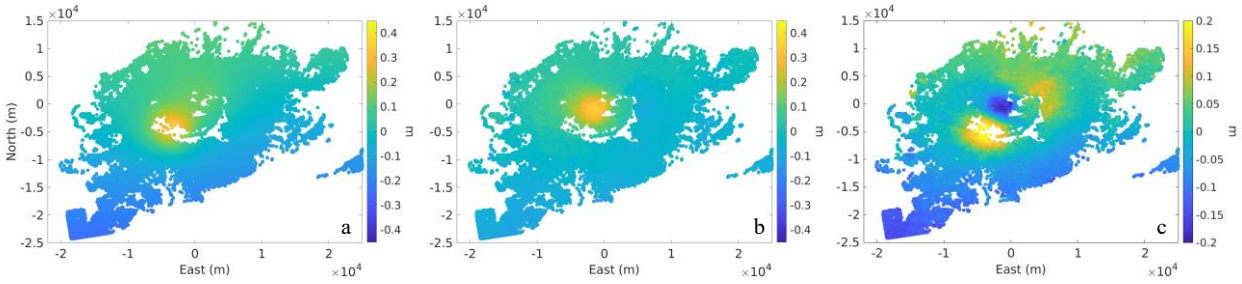

Figure 5.4. (a) Surface deformation predicted by the best fit distributed reservoir model. (b) cumulative deformation from 2015 to 2021 derived from InSAR (Wang et al., 2021). (c) Difference between figure a and b, note the color scale is different from a and b.

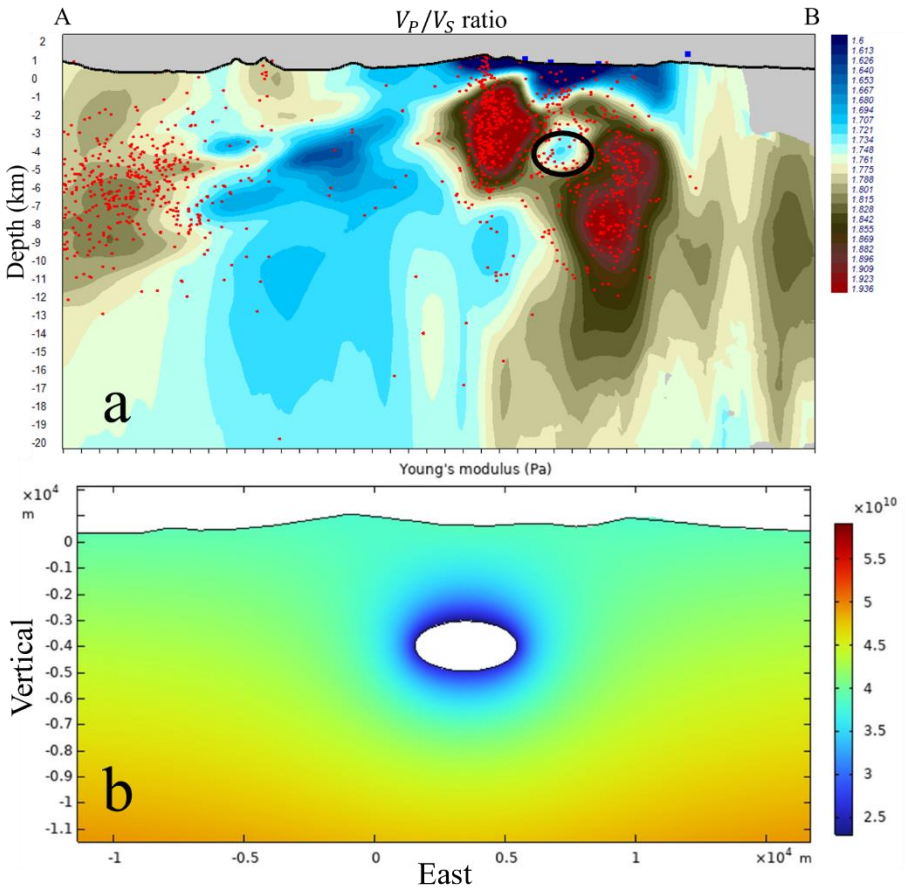

Figure 5.5. (a). Similar as Figure 5.3b, with the reservoir location marked as black solid ellipsoid. (b). Profile of Young's modulus for part of the cross-section in (a).

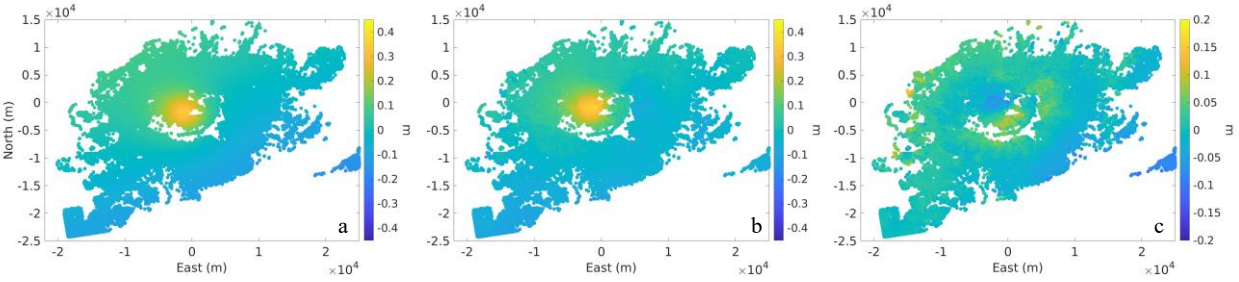

Figure 5.6. (a) Surface deformation predicted by the best fit single reservoir model. (b) cumulative deformation from 2015 to 2021 derived from InSAR (Wang et al., 2021). (c) Difference between figure a and b, note the color scale is different from a and b.

5.5 Discussion and Conclusion

The better fit between the single reservoir model and the InSAR observation compared to the distributed reservoir model indicates that, for Okmok volcano, the magma intrusion may be characterized by low V_p, V_s and moderate V_p/V_s ratio, instead of high V_p and V_p/V_s ratio and low V_s suggested by Kasatkina et al. (2022). The seismic wave velocities are strongly dependent on the rock temperature, composition, pressure, the presence of fluid phase and crack density (Sanders et al., 1995; Lees, 2007). The high V_p and V_p/V_s ratio and low V_s anomaly beneath volcanoes are usually interpreted as a result of the presence of partial melting and volcanic fluids, e.g., Popocatépetl volcano in Mexico (Kuznetsov and Koulakov, 2014), Kluchevskoy volcano group in Russia (Koulakov et al., 2011), and Redoubtt volcano in Alaska (Kasatkina et al., 2014). However, these anomalies can also be representative of solidified mafic magmatic intrusion with fluid-filled cracks that form the core of the caldera (Lin et al., 2014; Karakonstantis et al., 2019; Feuillet et al., 2004; Foix et al., 2021). Furthermore, Miller et al. (2020) find that these anomalous bodies are characterized by positive radial anisotropy, i.e., the slow velocity axis for S wave is vertical and all orthogonal directions are faster, indicative of horizontally aligned features. The concentration of earthquakes inside the anomalous bodies may be a result of hydro-fracturing in response to pressure accumulation in the nearby magmatic reservoir, i.e., the region with low V_p, V_s, and moderate V_p/V_s ratio, which may have also promoted the dike propagations during the 1997 and 2008 eruption.

The position of the inferred magmatic reservoir is consistent with the location of the highest radial anisotropy and sparse earthquakes (Miller et al., 2020; Kasatkina et al., 2022). The moderate V_p/V_s ratio in the inferred regions of magma intrusion/storage may be a result of volatile-rich magmas. Previous studies find volatile content of the intruding magma at Okmok may exceed $\sim 4\ wt.\%$ (Fournier, 2008; Kilbride et al., 2016). Larger volatile contents may result in higher magma compressibility, thus lower effective bulk modulus to the magnitude of $10^8\ Pa$ for magma storage at depth ~3-4 km BSL at Okmok volcano, which is much lower than that of the unsaturated magma ($> 10^9\ Pa$; Huppert & Woods, 2002). The high volatile contents and possible degassing may result in a reduced V_p/V_s ratio compared to the high V_p/V_s ratio commonly seen associated with partial melting and volcanic fluids (Fournier, 2008; Vargas et al., 2017; Patanè wt al., 2006). It is worth noting that those models are only sensitive to dynamic magma/fluid migrations, we still cannot rule out the possibility of long-term steady partial melt residing in regions with high V_p and V_p/V_s ratio and low V_s.

The integration of seismic tomography and geodetic deformation measurements suggests that, for Okmok volcano, a magmatic reservoir located about 4 km beneath the central caldera is responsible for the previous 1997 and 2008 eruption and the associated surface deformation. While seismic tomography exhibits greater sensitivity to compositional and structural distributions, geodetic deformation measurements are more sensitive to mechanical processes. When considered separately, seismic tomography and geodetic deformation measurement, in many cases, cannot provide unambiguous constraints to the volcanic system. This study highlights the importance of incorporating multi-disciplinary observations for the modeling of the complex magmatic system and the interpretation of geophysical observations for volcano monitoring. It should be noted that the local earthquake tomography presented in Kasatkina et al.

(2022) is based on seismicity recorded spanning a long period from 2003 to 2017, during which a large eruption and several successive intrusion events occurred (Wang et al., 2021), which may change the seismic structure of P and S wave velocities with time (Londoño et al., 2018; Patanè et al., 2006). Additional efforts are needed to validate the robustness of the derived seismic tomography. Furthermore, inverse modeling of the geodetic deformation measurements incorporating more reliable material properties is needed to construct more robust plumbing system models.

5.6 Acknowledgements

This research is funded by NASA Earth Surface & Interior Program (80NSSC19K0357), and the Shuler-Foscue Endowment at the Southern Methodist University.

5.7 References

Biggs, J., Z. Lu, T. Fournier, and J. T. Freymueller (2010), Magma flux at Okmok Volcano, Alaska, from a joint inversion of continuous GPS, campaign GPS, and interferometric synthetic aperture radar, Journal of Geophysical Research: Solid Earth, 115(B12).

Currie, C. A. and R. D. Hyndman (2006), The thermal structure of subduction zone back arcs, Journal of Geophysical Research: Solid Earth, 111(B8).

Feuillet, N., C. Nostro, C. Chiarabba, and M. Cocco (2004), Coupling between earthquake swarms and volcanic unrest at the Alban Hills Volcano (central Italy) modeled through elastic stress transfer, Journal of Geophysical Research: Solid Earth, 109(B2).

Fliedner, M. M. and S. L. Klemperer (1999), Structure of an island‐arc: Wide‐angle seismic studies in the eastern Aleutian Islands, Alaska, Journal of Geophysical Research: Solid Earth, 104(B5), 10667-10694.

Foix, O., C. Aiken, J. Saurel, N. Feuillet, S. J. Jorry, E. Rinnert, and I. Thinon (2021), Offshore Mayotte volcanic plumbing revealed by local passive tomography, J. Volcanol. Geotherm. Res., 420, 107395.

Fournier, T. J. (2008), Analysis and Interpretation of Volcano Deformation in Alaska: Studies from Okmok and Mt. Veniaminof Volcanoes, University of Alaska fairbanks.

Huppert, H. E. and A. W. Woods (2002), The role of volatiles in magma chamber dynamics, Nature, 420(6915), 493-495.

Karakonstantis, A., P. Papadimitriou, C. Millas, I. Spingos, I. Fountoulakis, and G. Kaviris (2019), Tomographic imaging of the NW edge of the Hellenic volcanic arc, J. Seismol., 23, 995-1016.

Kasatkina, E., I. Koulakov, R. Grapenthin, P. Izbekov, J. F. Larsen, N. Al Arifi, and S. I. Qaysi (2022), Multiple magma sources beneath the Okmok caldera as inferred from local earthquake tomography, Journal of Geophysical Research: Solid Earth, 127(10), e2022JB024656.

Kasatkina, E., I. Koulakov, M. West, and P. Izbekov (2014), Seismic structure changes beneath Redoubt Volcano during the 2009 eruption inferred from local earthquake tomography, Journal of Geophysical Research: Solid Earth, 119(6), 4938-4954.

Kilbride, B. M., M. Edmonds, and J. Biggs (2016), Observing eruptions of gas-rich compressible magmas from space, Nature Communications, 7(1), 13744.

Koulakov, I., E. Boychenko, and S. Z. Smirnov (2020), Magma chambers and meteoric fluid flows beneath the Atka volcanic complex (Aleutian Islands) inferred from local earthquake tomography, Geosciences, 10(6), 214.

Koulakov, I., E. I. Gordeev, N. L. Dobretsov, V. A. Vernikovsky, S. Senyukov, and A. Jakovlev (2011), Feeding volcanoes of the Kluchevskoy group from the results of local earthquake tomography, Geophys. Res. Lett., 38(9).

Kuznetsov, P. Y. and I. Y. Koulakov (2014), The three-dimensional structure beneath the Popocatépetl volcano (Mexico) based on local earthquake seismic tomography, J. Volcanol. Geotherm. Res., 276, 10-21.

Larsen, J. F., M. G. Śliwiński, C. Nye, C. Cameron, and J. R. Schaefer (2013), The 2008 eruption of Okmok Volcano, Alaska: Petrological and geochemical constraints on the subsurface magma plumbing system, J. Volcanol. Geotherm. Res., 264, 85-106.

Larsen, J., C. Neal, P. Webley, J. Freymueller, M. Haney, S. McNutt, D. Schneider, S. Prejean, J. Schaefer, and R. Wessels (2009), Eruption of Alaska volcano breaks historic pattern, Eos, Transactions American Geophysical Union, 90(20), 173-174.

Lees, J. M. (2007), Seismic tomography of magmatic systems, J. Volcanol. Geotherm. Res., 167(1-4), 37-56.

Lin, G., P. M. Shearer, R. S. Matoza, P. G. Okubo, and F. Amelung (2014a), Three‐dimensional seismic velocity structure of Mauna Loa and Kilauea volcanoes in Hawaii from local seismic tomography, Journal of Geophysical Research: Solid Earth, 119(5), 4377-4392.

Londoño, J. M. and H. Kumagai (2018), 4D seismic tomography of Nevado del Ruiz Volcano, Colombia, 2000–2016, J. Volcanol. Geotherm. Res., 358, 105-123.

Lu, Z., D. Dzurisin, J. Biggs, C. Wicks Jr, and S. McNutt (2010), Ground surface deformation patterns, magma supply, and magma storage at Okmok volcano, Alaska, from InSAR analysis: 1. Intereruption deformation, 1997–2008, Journal of Geophysical Research: Solid Earth, 115(B5).

Mann, D., J. Freymueller, and Z. Lu (2002), Deformation associated with the 1997 eruption of Okmok volcano, Alaska, Journal of Geophysical Research: Solid Earth, 107(B4), ETG 7-12.

Masterlark, T., T. Donovan, K. L. Feigl, M. Haney, C. H. Thurber, and S. Tung (2016), Volcano deformation source parameters estimated from InSAR: Sensitivities to uncertainties in seismic tomography, Journal of Geophysical Research: Solid Earth, 121(4), 3002-3016.

Masterlark, T., K. L. Feigl, M. Haney, J. Stone, C. Thurber, and E. Ronchin (2012), Nonlinear estimation of geometric parameters in FEMs of volcano deformation: Integrating tomography models and geodetic data for Okmok volcano, Alaska, Journal of Geophysical Research: Solid Earth, 117(B2).

Miller, D., N. Bennington, M. Haney, P. Bedrosian, K. Key, C. Thurber, L. Hart, and S. Ohlendorf (2020), Linking magma storage and ascent to eruption volume and composition at an arc caldera, Geophys. Res. Lett., 47(14), e2020GL088122.

Sanders, C. O., S. C. Ponko, L. D. Nixon, and E. A. Schwartz (1995), Seismological evidence for magmatic and hydrothermal structure in Long Valley caldera from local earthquake attenuation and velocity tomography, Journal of Geophysical Research: Solid Earth, 100(B5), 8311-8326.

Sandwell, D. T., J. A. Goff, J. Gevorgian, H. Harper, S. Kim, Y. Yu, B. Tozer, P. Wessel, and W. H. Smith (2022), Improved bathymetric prediction using geological information: SYNBATH, Earth and Space Science, 9(2), e2021EA002069.

Segall, P., K. R. Anderson, F. Pulvirenti, T. Wang, and I. Johanson (2020), Caldera collapse geometry revealed by near‐field GPS displacements at Kīlauea Volcano in 2018, Geophys. Res. Lett., 47(15), e2020GL088867.

Segall, P., A. L. Llenos, S. Yun, A. M. Bradley, and E. M. Syracuse (2013), Time‐dependent dike propagation from joint inversion of seismicity and deformation data, Journal of Geophysical Research: Solid Earth, 118(11), 5785-5804.

Vargas, C. A., I. Koulakov, C. Jaupart, V. Gladkov, E. Gomez, S. El Khrepy, and N. Al-Arifi (2017), Breathing of the Nevado del Ruiz volcano reservoir, Colombia, inferred from repeated seismic tomography, Scientific Reports, 7(1), 46094.

Wang, J., Z. Lu, D. Bekaert, C. Marshak, M. Govorcin, S. Sangha, J. Kennedy, and P. Gregg (2023), Along‐Arc Volcanism in the Western and Central Aleutian From 2015 to 2021 Revealed by Cloud‐Based InSAR Processing, Geophys. Res. Lett., 50(23), e2023GL106323.

Wang, J., Z. Lu, and P. M. Gregg (2021), Inflation of Okmok volcano during 2008–2020 from PS analyses and source inversion with finite element models, Journal of Geophysical Research: Solid Earth, 126(10), e2021JB022420.

Yang, X., D. C. Roman, M. Haney, and C. A. Kupres (2023), Double reservoirs imaged below Great Sitkin Volcano, Alaska, explain the migration of volcanic seismicity, Geophys. Res. Lett., 50(11), e2022GL102438.

Zhan, Y., P. M. Gregg, H. Le Mével, C. A. Miller, and C. Cardona (2019), Integrating reservoir dynamics, crustal stress, and geophysical observations of the Laguna del Maule magmatic system by FEM models and data assimilation, Journal of Geophysical Research: Solid Earth, 124(12), 13547-13562.

Zhan, Y., P. M. Gregg, and Z. Lu (2021), Modeling magma system evolution during 2006–2007 volcanic unrest of Atka Volcanic Center, Alaska, Journal of Geophysical Research: Solid Earth, 126(2), e2020JB020158.

CHAPTER 6
CONCLUSION

By applying advanced time-series InSAR algorithms, I have mapped the deformation history for the volcanoes in the central and western Aleutian. The deformation time series are then utilized to track the temporal evolution of the magma migration/storage inside the magmatic plumbing systems with numerical models. The post-eruptive deformation at Okmok volcano since the 2008 eruption is produced with SAR data collected across platforms, i.e., X-band TerraSAR-X, C-band Envisat and Sentinel-1, L-band ALOS and ALOS2, using PSInSAR method. Continuous inflation episodes characterized by time-dependent rates ranging from $40-195\ mm/yr$ are identified at Okmok from 2008 to 2021. The InSAR measurements agree well with the continuous GNSS records with the standard deviation of their misfit less than 1 cm at most of the GNSS stations. The deformation time series calculated from InSAR and GNSS are assimilated into finite element models using the EnKF to track the evolution of the magma intrusion and storage within the magma system through time. The results suggest that the inflation episodes can be well explained by a spatially stable spherical source located about 3 km beneath the central caldera, which is consistent with the source responsible for the 1997 and 2008 eruption as well as the inter-eruptive deformation from 1997 to 2008. The cumulative volume change during 2008–2020 is ~160% and ~60% of the total volumes of the 1997 and the 2008 eruptions, respectively.

Chapter 3 presents another work using the PSInSAR and EnKF to track the temporal evolution of the magmatic system of the Makushin volcano. SAR scenes acquired from C-band Envisat and Sentinl-1, X-band TerraSAR-X, and L-band ALOS2 are used to produce the deformation history for Makushin volcano from 2004 to 2021. Multiple inflation/deflation cycles located to the northeast of the central peak with time-dependent rates ranging from $\sim 10 - 200\ mm/yr$ and distinct lifetimes are detected at Makushin. Another secondary deforming region located near the continuous GNSS station MREP with rates about half of the main is also identified. LOS deformation derived from TerraSAR-X, Sentinel-1 and ALOS-2 are verified with GNSS records and show good agreements. Time series deformations across the volcano are used for modeling the magmatic source of the volcanic system using Mogi sources. A spherical source with temporally stationary location located about 6 km BSL is believed responsible for the crustal deformation from 2004 and 2021. The cumulative volumetric change inside the inferred magma source is $\sim -6 \times 10^5\ m^3$, indicating long-term volume/pressure deficit processes within the plumbing system. The distinct temporal behaviors of the crustal uplift/subsidence cycles as well as the consistency between deformation cycle and annual SO_2 emission rates suggest a volatile intrusion/degassing dominated volcanic system. The secondary deformation can be modeled with a sill-like source about $2 - 3\ km$ BSL, likely implying a fluid/gas-rich reservoir. Persistent LOS lengthening independent of the volcanic deformation are detected over the valleys off the main peak, which may be possibly produced by surface erosion of the alluvium deposits.

In Chapter 4, a new time-series InSAR processing framework has been developed leveraging the ARIA GUNW products. Interferograms produced from Sentinel-1 scenes acquired during the summertime are used to map the deformation history for volcanoes from Gareloi to Veniaminof

in the western and central Aleutian from 2015 to 2021. The derived deformation time series is validated with continuous GNSS records at four sites. Deformation with distinct temporal and spatial patterns are identified from these volcanoes, e.g., persistent surficial subsidence related to thermal compaction of the lava flow and pyroclastic deposits emplaced during previous eruptions, continuous/episodic inflation in response to magma/fluid intrusion within the magmatic reservoir, cooling/degassing/crystallization induced persistent deflation, and transient tectonic deformation. Source locations and cumulative volume changes are derived with GBIS using Mogi sources for volcanoes with deep-seated displacements. Most of the volcanoes show deformation patterns similar to their historical behaviors. New deformation patterns have been identified at Tanaga, Great Siktin, and Yunaska volcano. The transient crustal shearing at Tanaga is believed to be a result of strike-slip earthquakes. Inflations/deflations identified from Great Sitkin are believed to be produced by the magma intrusion/withdraw associated with the 2018, 2019 and 2021 eruption (https://avo.alaska.edu/volcano/great-sitkin). The continuous deflation at Yunaska is probably produced by magma migration to locations that are not covered by the SAR observations. Overall higher magmatic activities in the central Aleutian are identified, which may be interpreted as consequences from higher magma production/ascent rate due to along-strike variation in the tectonic environments.

Chapter 5 shows some exploratory efforts on reconciliation between the geodetic deformation measurements and the seismic tomography for resolving the magmatic plumbing system. Seismic structures for V_p, V_s and V_p/V_s ratio are used to assist the developments of finite element models of the magmatic reservoirs for Okmok volcano. Surface deformation predicted by a distributed reservoir model and a single reservoir model are analyzed and compared with the geodetic deformation measurements. The single reservoir model with magma chamber

located ~4 km beneath the central caldera of Okmok, outlined by anomalous low V_p, V_s, and moderate V_p/V_s ratio is preferred by the surface deformation compared to the distribute reservoirs represented by high V_p and V_p/V_s ratio and low V_s anomaly. Although further work is needed to develop more robust magma chamber models, this work highlights the complexity of the magma plumbing system and the importance of joint interpretation of geophysical observations over volcanic environments.

The above studies have demonstrated the effectiveness of timeseries InSAR processing in capturing regional volcanic/nonvolcanic deformation over large, tectonic active environments. Source evolutions derived from inverse models of the deformation timeseries provide valuable insights into the complex magmatic processes and critical information for volcanic hazard forecasting and mitigations. The methodologies can be easily applied to other volcanoes or geophysical processes as well.